Reversibility of the Pathology in a Mouse Model of Fragile X-Associated Tremor/Ataxia Syndrome: Exploring Time-Dependence and Intervention Strategies

Thesis

for the degree of

doctor rerum naturalium (Dr. rer. nat.)

approved by the Faculty of Natural Sciences of Otto von Guericke University Magdeburg

by

Ufuk Emre Kul, M.Sc.

born on 15 April 1985 in Fatih / Istanbul

Examiner: Prof. Dr. Oliver Stork
PD Dr. Sabine Hölter-Koch

submitted on: 27 November 2019
defended on : 30 March 2020

DDC: 573.8639

Abstract

Trinucleotide repeat expansion mutations in the 5′ untranslated region of the fragile X mental retardation-1 gene (*fmr1*) are the underlying genetic cause of four distinct disorders. Large expansions result in silencing of the *fmr1* gene and its protein product fragile X mental retardation protein (FMRP) is not expressed. Lack of FMRP causes fragile X syndrome (FXS), the most common inherited cause of intellectual disability. Moderate expansions are referred to as premutations and are associated with fragile X-associated tremor/ataxia syndrome (FXTAS), fragile X-associated neuropsychiatric disorders (FXAND), and fragile X-associated primary ovarian insufficiency (FXPOI). The premutation disorders are distinct from FXS as they are caused by the aberrant RNA transcript of the *fmr1* that generally drives a degenerative process within the tissues that are associated with each disorder. FXTAS is the incurable late onset manifestation of the premutation and is characterized by action tremor, cerebellar gait ataxia, Parkinsonism and cognitive decline with memory deficits. Intranuclear inclusions are considered to be the hallmark of the disorder and are formed by aggregation of a broad range of proteins and mRNA. FXTAS has been previously modelled in an inducible mouse that expresses moderately expanded repeats in the brain. The mice formed inclusions throughout the brain and had poor motor performance. Taking advantage of the inducible nature of the model, phenotypes that have not been previously addressed are investigated using various induction timelines. Early onset anxiety-related phenotypes, as well as late onset Parkinsonian phenotypes are identified. Parkinsonism is found to be paralleled by nigrostriatal degeneration in this model. Given that no cure exists for FXTAS, two treatment strategies are developed and tested in the inducible mice. The first strategy is based on modulation of protein turnover in order to limit aggregation via activation of autophagic degradation pathway. The second strategy is an antisense gene therapy that aims to inactivate the aberrant mRNA that contains the expanded repeat locus. Both strategies resulted in a decrease in the intranuclear inclusion pathology and an improvement in the motor performance of the inducible mice. Although various strategies have been previously applied to limit the pathogenesis of FXTAS, the approach presented here is the first evaluation of potentially translational strategies in a mammalian model of FXTAS. Thus, these strategies are novel and serve to fill an important gap in the research field of FXTAS with relevance to the other *fmr1* premutation disorders.

Zusammenfassung

Eine Expansion der Trinucleotidwiederholungen im 5ʻ untranslatierten Bereich des fragile X mental retardation (fmr1) Gens ist Ursache für verschiedene Krankheiten. Eine moderate Expansion wird als Prämutation bezeichnet und steht im Zusammenhang mit fragile X-assoziiertem tremor/ataxia syndrome (FXTAS). Diese Krankheit wird von aberranten RNA-Transkripten verursacht, ist unheilbar und setzt spät ein. Sie ist charakterisiert durch Aktionstremor, cerebelläre Gangataxie, Parkinsonismus, sowie durch Gedächtnisdefizite und einer Abnahme der kognitiven Leistungsfähigkeit. Auf molekularer Ebene finden sich intranukleäre Einschlüsse, verursacht durch Aggregation von Proteinen und RNAs. In dieser Arbeit wurde ein induzierbares FXTAS-Mausmodel verwendet, für das intranukleäre Einschlüsse im Gehirn und motorische Defizite bereits beschrieben sind. Der induzierbare Charakter dieses Models erlaubte es den Einfluss der Prämutation in vershiedenen Entwicklungsstadien zu untersuchen und so den Angst-Phänotyp mit einer frühen, und den Parkinson-Phänotyp mit einer späten Induktion zu assoziieren. Darüberhinaus war Parkinsonismus von einer nigrostriatalen Degeneration begleitet. Da eine Heilung gegnwärtig nicht möglich ist, habe ich zwei Behandlungsstrategien entwickelt und getestet. Der erste Ansatz basiert auf der Manipulation des Protein-Turnovers um die Aggregation mithilfe einer Aktivierung des Autophagie-Degradierungsweges zu verhindern. Die zweite Strategie ist eine Antisense-Gentherapie mit dem Ziel der Inaktivierung aberranter mRNA. Beide Strategien führten zu einer Reduktion intranukleärer Einschlüsse und einer Verbesserung der motorischen Leistung.

Zusammenfassend konnte ich in diesem Modell bislang unbeschriebene Symptomklassen identifizieren, die von der Prämutation verursacht werden, und zwei Behandlungsmöglichkeiten etablieren. Obwohl bereits einige Interventionsansätze in Invertebraten existieren, sind die hier präsentierten Interventionen die ersten im Säugetier, was translationales Potential birgt.

Table of Contents

List of Figures

List of Tables

Abbreviations

°C	Degree Celsius
aCSF	artificial cerebrospinal fluid
AD	Alzheimers’s disease
ADHD	attention deficit hyperactivity disorder
AEBSF	4-(2-aminoethyl)benzenesulfonyl fluoride hydrochloride
ALS	amyotrophic lateral sclerosis
ANOVA	Analysis of variance
ASD	autism spectrum disorder
ASO	Antisense oligonucleotides
ASR	acoustic startle response
BL6	black6
BLA	basolateral amygdala
CA3	cornu ammonis-3
CCS	splenium of the corpus callosum
$\mathrm{CGG}^{\mathrm{exp}}$	expanded CGG repeats of the PM
$\mathrm{CGG}^{\mathrm{norm}}$	normal CGG repeat size up to 55 triplets
cm	Centimeter
CNS	central nervous system
CS	conditioned stimulus
CSPP	complex cortico-striato-pallidopontine
ctrl	control
DAT	dopamine active transporter
dB	Decibel
DG	dentate gyrus
DNA	Deoxyribonucleic acid
dNTP	Deoxynucleotide Triphosphate
Dox	doxycycline
EC	external capsule
EDTA	Ethylenediaminetetraacetic acid
EGNA	egress of nuclear aggregates

EtBr	Ethidium bromide
FDA	Food and Drug Administration
fEPSP	field excitatory postsynaptic potential
FM	full mutation
fmr1	fragile X mental retardation-1
FMRP	fragile X mental retardation protein
FMRpolyA	FMR polyalanine
FMRpolyG	FMR polyglycine
FMRpolyR	FMR polyarginine
FTD	frontotemporal dementia
FXAND	fragile X-associated neuropsychiatric disorders
FXPOI	fragile X-associated primary ovarian insufficiency
FXS	fragile X syndrome
FXTAS	fragile X-associated tremor/ataxia syndrome
GABA	gamma-aminobutyric acid
GFP	green fluorescent protein
h	Hour
HD	Huntington’s disease
HFS	high frequency stimulation
hnRNP	heterogenous nuclear ribonucloprotein particle
Hz	hertz
I/O	input-output
ICV	intracerebroventricular injection
IHC	immunohistochemistry
iPSC	induced pluripotent cell
ISI	Inter-stimulus interval
ITI	Inter-trial interval
kHz	Kilohertz
KI	knock-in
L	Liter
LA	lateral amygdala
LSD	Least Significant Difference

LTP	long-term potentiation
M.O.M.	mouse-on-mouse
mA	Milliampere
MCP	middle cerebellar peduncle
min	Minute
MPP	Medial perforant pathway
MRI	magnetic resonance imaging
ms	Millisecond
mTOR	mammalian target of rapamycin
NIH	National Institutes of Health
NMDA	N-methyl-D-aspartate
OCD	obsessive-compulsive disorder
PCR	polymerase chain reaction
PD	Parkinson’s Disease
PM	premutation
PPI	Prepulse inhibition
PrP	prion protein
PTSD	post-traumatic stress disorder
PTX	picrotoxin
PVDF	Polyvinylidene difluoride
RAN	repeat-associated non-AUG
RISC	RNA induced silencing complex
RNA	Ribonucleic acid
rtTA	reverse tetracycline-controlled transactivator
s	Second
S.E.M.	Standard error of the mean
SDS-PAGE	Sodium dodecyl sulfate polyacrylamide gel electrophoresis
SNP	single nucleotide polymorphisms
SNpc	substantia nigra pars compacta
SNpr	substantia nigra pars reticulata
STP	short-term potentiation
Tet-On	tetracycline-on

Th	tyrosine hydroxylase
TRE	tetracycline response element
treh	trehalose
UPS	ubiquitin proteasome system
UTR	untranslated region
VTA	ventral tegmental area
WO	wash-out
Wt	wild type
µl	Microliter

1 Introduction

Mutations in the 5′ untranslated region (UTR) of the fragile X mental retardation-1 gene (*fmr1*) have been identified as the genetic cause of two separate classes of disorders. The mechanisms that lead to disease manifestation are distinct from one class to the other however, the underlying genetic condition for all *fmr1*-related disorders is the expansion of the CGG/CCG repeats that are present in the 5′ UTR of the gene. Alleles with large number of repeats are unstable. They can undergo contraction as well as expansion giving rise to more than 30 genetic disorders, including but not limited to Huntington's disease (CAG/CTG), several types of spinocerebellar ataxias including Machado-Joseph disease (CAG/CTG), Haw River Syndrome (CAG/CTG), Kennedy's disease (CAG/CTG), myotonic dystrophy type I (CTG/CAG) and Friedrich ataxia (GAA/TTC). Genetic disorders caused by unstable repeats are not limited to triplets, a hexanucleotide repeat (GGGGCC/GGCCCC) in the *c9orf72* gene is linked to amyotrophic lateral sclerosis and frontotemporal dementia (van Blitterswijk, DeJesus-Hernandez, and Rademakers 2012).

1.1 Expansion of CGG/CCG-triplets in the *fmr1*

CGG/CCG repeat expansions in the fragile X mental retardation-1 gene adds four additional disorders to the list, all of which are related to trinucleotide repeat expansions at a locus that encodes the 5′ UTR of the gene's mRNA transcript. These are fragile X syndrome (FXS), fragile X-associated tremor/ataxia syndrome (FXTAS), fragile X-associated neuropsychiatric disorders (FXAND) and fragile X-associated primary ovarian insufficiency (FXPOI). *Fmr1* is located on X chromosome at Xq27.3 and encodes the fragile X mental retardation protein (FMRP). FMRP is expressed in a broad range of human tissues with high levels found in lungs, gastrointestinal tract, kidneys, reproductive tissues and brain (Uhlen et al. 2015). FMRP is an RNA binding protein that can translocate between nucleus and cytoplasm with roles in the mRNA stability and shuttling and repression of mRNA translation. In the brain, FMRP is associated with polysomes at postsynaptic sites with modulatory function in protein synthesis at dendrites (Bardoni, Schenck, and Mandel 2001), (Zalfa et al. 2007).

CGG repeats harbored in the 5′UTR of the *fmr1* may become unstable during maternal transmission and the length may vary in the next generation that gives rise to a polymorphism in the normal population with repeat lengths ranging from 6 to 55 (Willemsen, Levenga, and Oostra 2011). However, the changes in the size of the repeats occur with a 1:10 bias favoring expansion. These expansions mainly occur prezygotically, but somatic expansions have also been observed (Zhao and Usdin 2016). As the repeat size passes the 55-repeat threshold, the risks of developing FXTAS, FXAND and FXPOI significantly increases. These disorders are associated with expanded repeat length of 55-200 repeats that is also known as *fmr1* premutation. The premutation in return, predisposes the allele for further expansions and new expansions drives the allele to a full mutation (FM; >200 repeats), which is the underlying genetic cause of FXS (R. J. Hagerman et al. 2018).

Although the CGG repeats that the *fmr1* gene contains are associated with different disorders depending on the size of the repeat stretch, the repeat number is not the only factor that determines an allele’s predisposition for future expansion events. Within the CGG repeat locus of the *fmr1* there are one or more AGG interruptions that have a periodicity of 9-11 repeats. These interruptions in the CGG repeat stretch decrease the risk of allele instability during maternal transmission. The risk of further expansions is directly related to the total number of AGG interruptions including the risk of expansion to a full mutation from an already expanded premutation allele. Apart from the size of the repeat stretch and the number of AGG interruptions it contains, factors like family history and maternal age contribute to the risk of expansions at the CGG repeat locus, though to a lesser extent (C. M. Yrigollen et al. 2014). Animal studies also revealed additional factors that might increase the risk of expansions including exposure to oxidizing agents that damage DNA, single nucleotide polymorphisms (SNPs) related to DNA repair machinery and gender. Somatic expansions occur less frequently in female mice, an observation that is mostly attributed to the X chromosome inactivation (Zhao and Usdin 2016).

In spite of the identification of some of the factors that influence the expansion of the CGG repeats from one generation to the next, the mechanisms, by which these expansions occur is less understood. One of the proposed mechanisms is based on strand slippage during DNA replication caused by unusual single stranded secondary structures, such as hairpin, quadruplex and R-loop RNA:DNA hybrid that the repeat containing DNA stands may form. These structures are proposed to render the DNA prone to slippage and a 5’ slippage of the

DNA strand that is being newly synthesized with repriming at the slipped position could, in this case, result in the incorporation of additional bases into this strand. Retractions are also possible under this mechanism when the slippage takes place in the template strand. The AGG interruptions would then be a destabilizing factor on these secondary structures that the repeat-DNA may form, thereby protecting the DNA from repeat length changes during replication (Zhao and Usdin 2016).

1.2 FXS: The disorder of the full mutation

Fragile X syndrome is the most common monogenic cause of intellectual disability that affects females (1 in 7000 to 10000) and males (1 in 4000 to 6000) alike. However, symptoms manifest more severely in males. The manifestation of the disorder starts early in childhood with delays in speech development, autistic-like behavior, anxiety, hyperactivity and moderate-to-severe mental retardation. Most affected individuals have characteristic physical features like mild facial dysmorphia with long and narrow face, prominent ears and jaw and macroorchidism in males (Mandel and Biancalana 2004). FXS manifests as an impairment in dendritic spine maturation and pruning in the brain resulting in changes in synaptic plasticity. This phenotype is considered to be linked to the role of FMRP in the postsynapse (Irwin 2000).

The expansion of the CGG triplets beyond 200 repeats is the genetic cause of the FXS that results in the hypermethylation of the promotor region of *fmr1*. As a result, the gene is silenced and FMRP is not produced. The maternally transmitted FM is highly unstable during the early embryogenesis and can give rise to mosaicisms. The mosaic pattern is caused by the presence of both FM and PM alleles with in the same individual. This type of size mosaicism is caused by the somatic retraction of the expanded repeats in some but not all cells during embryogenesis. Methylation can be another factor that leads to a mosaic pattern as it can be partial when the repeat length is between 200-250. These mosaicisms allow for expression of FMRP at low levels and in some cases result in a milder cognitive phenotype (Pretto et al. 2014).

The inheritance of FXS happens only through maternal transmission therefore seen only with children of PM carrier mothers. The PM does not expand in male carriers as it is passed onto the next generation. However, PM carrier men pass the allele onto their daughters, who in return, have a high risk of passing on the PM allele as a FM allele to their children and developing FXPOI, FXAND or FXTAS (Mandel and Biancalana 2004), (R. J. Hagerman et al. 2018).

1.3 Disorders of the premutation

Moderate CGG repeat expansions ranging from 55 to 200 at the 5'UTR of the *fmr1* gene are common in the general population (females; 1 in 200, males; 1 in 400) and classified as premutations and are associated with three distinct disorders with incomplete penetrance. The pathological mechanisms of the PM are also very distinct from the FM. In the PM, *fmr1* is not silenced, on the contrary PM alleles give rise to an increase in the expression of their mRNA transcripts. These mRNA form extended hairpin structures that is considered as one of the main pathogenic mechanisms of the PM disorders. Extended hairpin structures on these transcripts have been proposed to result in a toxic RNA gain-of-function mechanism that alters the normal function of specific proteins and interfere with cellular homeostasis. On the other hand, less FMRP is translated from these manuscripts together with a polyglycine-containing homopolypeptide (FMRpolyG) via the repeat-associated non-AUG (RAN) translation mechanism. Interference of FMRpolyG with various cellular functions is considered to be a toxic protein gain-of-function mechanism, the other main pathogenic mechanism of the PM (Glineburg et al. 2018). Both mechanisms seem to contribute to the formation of intranuclear aggregates that sequester various proteins and RNA, including the *fmr1* mRNA and the FMRpolyG (Tassone, Iwahashi, and Hagerman 2004), (Todd et al. 2013).

1.3.1 FXPOI

Primary ovarian insufficiency is a subfertility disorder that affects around 1% of the normal population. The disorder is characterized by cessation of menstruation before the age of 40. However, it differs from menopause because ovarian function may not be completely lost with conception rates up to 10% in the diagnosed women. Women premutation carriers are at a higher risk of developing primary ovarian deficiency with a prevalence of around 20%.

FXPOI is believed to be caused by abnormal follicle function rather than depletion of the primordial follicles that contains oocytes and granulosa cells (Fink et al. 2018). Although, FMRP has been implicated to play a role in oocyte development in embryonic stages (Rosario et al. 2016), RNA gain-of-function as well as RAN translation are considered to be main pathogenic mechanisms that result in this substantial increase in prevalence among the PM carriers. Decreased levels of FMRP is not considered to be the culprit, as full mutation carriers do not suffer from primary ovarian deficiency (Sherman et al. 2014). On the other hand, intranuclear inclusions with FMRpolyG foci have been identified in the ovaries of a FXPOI patient as well as of the PM mice (Buijsen et al. 2016).

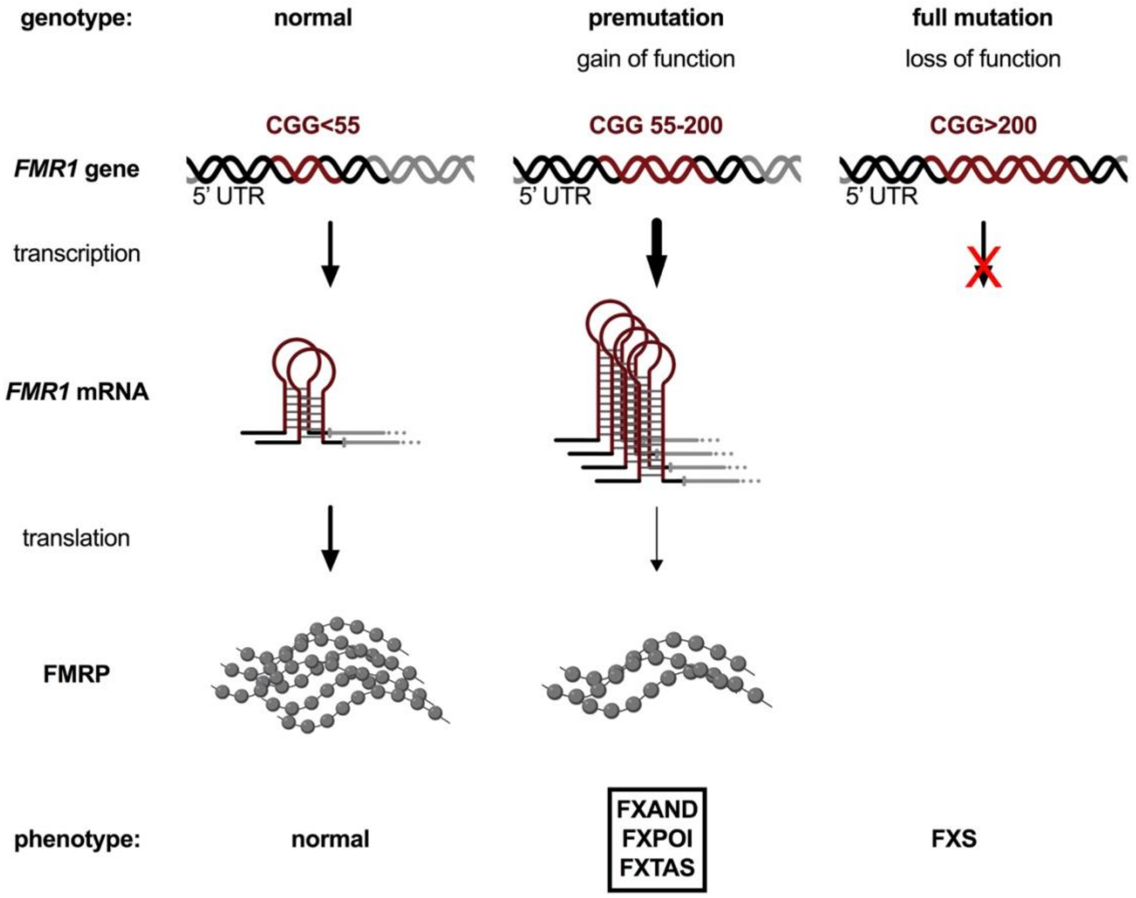

Figure 1.1: Genotype to phenotype comparison between distinct ranges of the 5' UTR repeat lengths of fmr1

Normal population has 6 to 54 CGG triplets in the 5' UTR of the fmr1 gene. An elevation of fmr1 mRNA transcript levels together with a decrease in FMRP production is seen when the repeats moderately expand to the 55-200 PM range. This expansion is associated with FXAND, FXPOI and FXTAS. Expansions beyond 200 CGG triplets result in DNA hypermethylation and silencing of fmr1. The absence of FMRP is associated with FXS. (Adapted from R. J. Hagerman and Hagerman 2002)

1.3.2 FXAND

Fragile X-associated neuropsychiatric disorders (FXAND) are a class of disorders with the highest (up to 50%) prevalence among the PM carriers. These can manifest as early as childhood with broad range of symptoms related to autism, ADHD, social deficits and anxiety. In adults, anxiety and depression are the dominating manifestations but obsessive-compulsive disorder and ADHD that is also linked to substance abuse are also reported.

FXAND is the newest addition to the list of premutation disorders and named with the purpose of increasing awareness and promote timely recognition of the PM as these neuropsychiatric manifestations typically occur at an early age (R. J. Hagerman et al. 2018).

Low FMRP levels are believed to play a role in some of the phenotypes associated with FXAND in the childhood. However, it is not known whether or not the intranuclear inclusion pathology occurs in the brains of FXAND patients despite their earlier age due to the unavailability of post-mortem tissue. However, the two main pathogenic mechanisms of the PM, namely RNA gain-of-function and RAN translation occur regardless of the age and are believed to be responsible for the manifestation of FXAND (R. J. Hagerman et al. 2018). Moreover, an older study that was published before the recognition of FXAND, reports intranuclear inclusion pathology in the brain of an asymptomatic female PM carrier, who died of cancer at the age of 76 (Tassone et al. 2012).

1.3.3 FXTAS

Fragile X-associated tremor/ataxia syndrome (FXTAS) is the late onset manifestation of the PM affecting the older carriers, typically above 60 years of age. FXTAS predominantly affects male carriers with a prevalence of approximately 40%, whereas females are believed to be relatively protected by X chromosome inactivation with a prevalence of 16% among the PM population. FXTAS is a progressive neurodegenerative disorder characterized by the onset of intention tremor followed by cerebellar gait ataxia. Other features of the disorder include neuropathy, autonomic dysfunction, Parkinsonism and cognitive decline with memory and executive function deficits. (R. J. Hagerman et al. 2018), (Ma et al. 2019). The risk of developing FXTAS increases dramatically with age and the CGG repeat length is considered to be a predictor of the age of onset for both tremor and ataxia (Tassone et al. 2007).

The intranuclear inclusions are considered to be the hallmark of the disorder, they occur throughout the body and in the brain, both in neurons and astrocytes. Both RNA gain-of-function and RAN translation have been described for FXTAS as main mechanisms of neurotoxic action (R. J. Hagerman et al. 2018). The features and the pathologic mechanisms of the premutation are described in more detail within the context of FXTAS in the following sections.

1.4 Clinical features of FXTAS and diagnostics

Action tremor and cerebellar gait ataxia are considered the major clinical features of FXTAS. However, FXTAS can present with a variety of features and other symptoms. Parkinsonism, short-term memory deficiency, executive function deficits and neuropathy make up the minor diagnostic criteria (Hall et al. 2014). Parkinsonism is common in the FXTAS patient group with a prevalence of 29%. The common features of Parkinsonism like body bradykinesia and resting tremor has been individually identified in 52% and 26% of the FXTAS patients respectively (Niu et al. 2014). In some studies, these numbers are even higher (Apartis et al. 2012). However, the pathologic mechanisms underlying the Parkinsonism seen in FXTAS are not clear. Dopamine transporter scans that are used as an alternative diagnostic criterion for Parkinson's Disease (PD) (Kagi, Bhatia, and Tolosa 2010) showed evidence on dopaminergic nigrostriatal dysfunction only in approximately half of the FXTAS cases with Parkinsonism. On the other hand, FXTAS cases with concomitant PD pathologies including loss of neurons in the substantia nigra and α-synuclein positive Lewy bodies have been reported (De Pablo-Fernandez et al. 2015). Parkinsonism in FXTAS also interacts with the other minor diagnostic criteria. One study found that FXTAS patients with Parkinsonism have significantly more severe deficits related to executive function and memory compared to patients without Parkinsonism. (X.-H. Wang et al. 2018). This finding also parallels the literature on PD (Muslimovic et al. 2005).

Medical comorbidities involving a variety of organs also exist in FXTAS, including seizures, migraine, sensorimotor impairments, cardiac arrhythmias, hypertension, thyroid disease, fibromyalgia, autoimmune disease, irritable bowel syndrome, urinary incontinence and impotence (R. J. Hagerman et al. 2018), (Schneider et al. 2012), (Coffey et al. 2008), (Leehey 2009).

Apart from clinical features, radiological findings that are specifically associated with FXTAS also exist. These radiological features are critical in establishing FXTAS diagnosis. The two major radiological signs as detected from magnetic resonance imaging (MRI) scans are the white matter lesions in middle cerebellar peduncle (MCP) and in the splenium of the corpus callosum (CCS). Minor radiological features include, lesions involving cerebral white matter and generalized atrophy. The major pathological feature used for diagnosis from the *post-mortem* tissue is the intranuclear inclusions in the central nervous system (CNS). For the definite diagnosis of FXTAS one clinical major and one radiological major feature or the intranuclear inclusions must be present (Hall et al. 2014).

1.5 Neuropathology of FXTAS

Classically, the hallmark of the neuropathology in FXTAS is ubiquitin-positive intranuclear inclusions found mostly as solitary particles distinct from nucleoli, in neurons and glia alike throughout the CNS. They are most numerous in the hippocampus. In cerebellum, these inclusions were identified in the dentate nucleus neurons, in the Purkinje and granule cells and more diffusely in glia (Greco et al. 2002), (Ariza et al. 2016), (Ma et al. 2019). The ubiquitin-rich nature of inclusions was later on, linked to an impairment in the ubiquitin proteasome system (UPS) (Oh et al. 2015), (Ma et al. 2019). Moreover, the FXTAS inclusions have been shown to contain hundreds of different proteins, many of which have complex functions that could contribute to the pathogenesis of FXTAS (Iwahashi et al. 2006), (Ma et al. 2019). Two examples are given below.

Alterations to the nuclear lamina have been observed in autopsied samples of FXTAS and believed to be a component of the FXTAS pathogenesis. The nuclear lamina has been found to be disorganized also in neurons differentiated from FXTAS induced pluripotent cells (iPSCs). This observation was attributed to a nuclear lamina protein LAP2β, whose normal localization has been lost and has been found to be sequestered into the inclusions (Sellier et al. 2017), (Arocena et al. 2005). LAP2β is a nuclear protein that has roles in the assembly of the nuclear lamina and is essential for the maintenance of the nucleus integrity. Its loss has been associated with disruption of the nuclear envelope and cell death (Dubińska-Magiera et al. 2016).

P62/sequestrosome-1 is another protein that is highly enriched in the FXTAS inclusions with roles that may have important implications for the pathogenesis. P62 is part of the autophagy lysosome pathway, the main endogenous cellular degradation pathway targeting aggregates. Normal functioning of p62 involves binding aggregates and mediating their transport to lysosome for degradation. The presence of P62 in the inclusions is interpreted as a cellular effort to target these aggregates for autophagy that ultimately fails as the inclusions get too big to be able to exit the nucleus. This potential problem is believed to be intensified with the added contribution of the failing UPS degradation (Ma et al. 2019).

Apart from the intranuclear inclusions, there are many other pathological features observed from the FXTAS brains. Cerebellum is predominantly affected but not singled out from occurrence of these features. Some of these neuropathological characteristics include white matter disease both in cerebrum and cerebellum with dramatically enlarged astrocytes, cerebellar white matter spongiosis with axonal and myelin loss and substantial loss of Purkinje cells in the cerebellum accompanied by Bergmann gliosis. (Greco et al. 2006). Moreover, iron accumulation in the cerebellar dentate nucleus (Rogers et al. 2016) and in the putamen reflecting an impaired iron metabolism (Ariza et al. 2017), increased oxidative stress following mitochondrial dysfunction (Ross-Inta et al. 2010), high intracellular calcium levels related to abnormal Ca^{2+} dynamics (Robin et al. 2017) have also been described for FXTAS.

1.6 Mechanisms of neuropathology in FXTAS

Although the pathological features of FXTAS have been intensively studied, the mechanism(s) involved in the formation of inclusions and the subsequent neurodegeneration are still not completely known. Two main mechanisms have been proposed with evidence supporting that each may take place in the FXTAS brain separately or in combination (Sellier et al. 2017). The first model is based on sequestration of one or more RNA-binding proteins via interactions with PM mRNA containing expanded repeats that results in functional depletion of the protein pool. The second model proposes that CGG repeats can be translated to give rise to a homopolypeptide, FMRpolyG, in spite of the repeat locus being in the 5′ UTR of the *fmr1* mRNA. FMRpolyG is believed to be toxic and prone to aggregation. (Todd et al. 2013), (Sellier et al. 2017), (Hoem et al. 2019).

1.6.1 RNA toxic gain-of-function

The most important evidence that supports a toxic RNA gain-of-function mechanisms for FXTAS pathogenesis is the presence of *fmr1* mRNA within the intranuclear inclusions (Raske and Hagerman 2009), (Tassone, Iwahashi, and Hagerman 2004). Sequestration of RNA-binding proteins into the inclusions via their interaction with the expanded repeat containing *fmr1* RNA and the subsequent loss of their function have been demonstrated for a number of proteins (Sellier et al. 2010). In fact, more than half of the proteins identified in the inclusions are RNA binding or are involved in protein turnover (Ma et al. 2019).

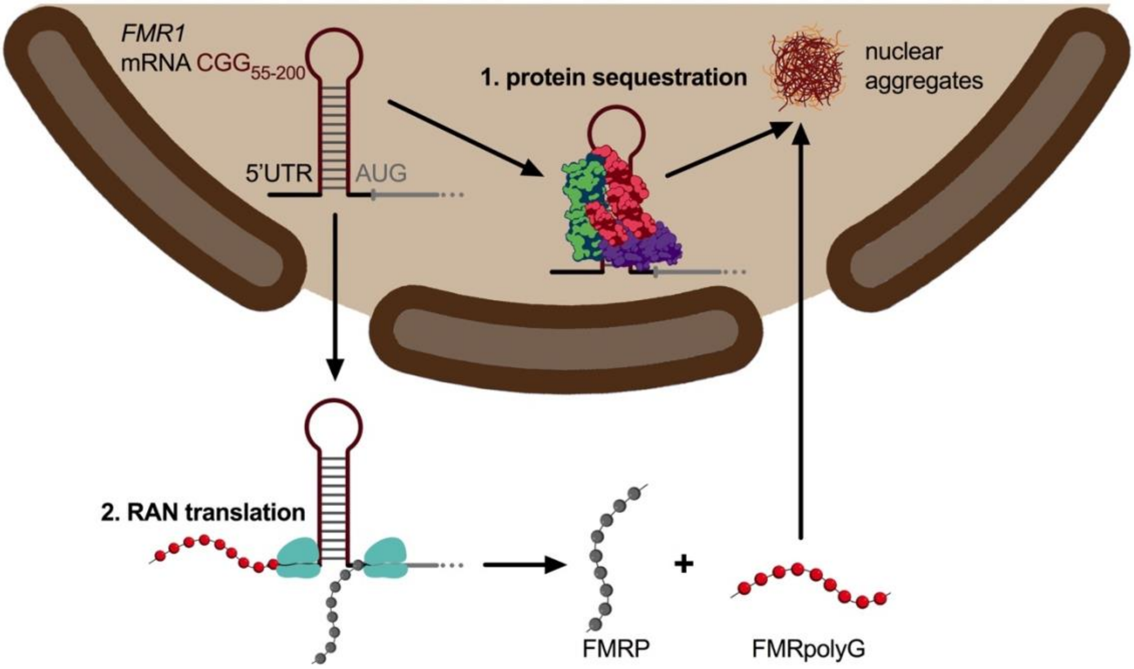

Figure 1.2: The two main mechanisms of pathogenesis in FXTAS
1. RNA gain-of-function, which results in the sequestration of RNA binding proteins and drives aggregation. 2. RAN translation that produces the toxic FMRpolyG homopolymeric peptide that is prone to aggregation.

One important example is DGCR8, an RNA binding protein that binds double-stranded RNA, which then recruits DROSHA, an RNase that functions in the miRNA processing. DGCR8 has been found to preferentially bind the double stranded hairpin on the expanded CGG repeats of the PM mRNA (CGG^{exp}-mRNA) and gets partially immobilized together with its partner DROSHA. This sequestration reduces the abundance of these proteins and their functional activity. As a result, a decrease in the levels of mature miRNAs is observed that is associated with a decrease in cell viability. The secondary sequestration of DROSHA via its interaction with the RNA-binding DGCR8 points out that accumulation of proteins around the CGG^{exp}-mRNA is also possible by further protein-protein interactions (Sellier et al. 2013).

A different type of mRNA gain-of-function occurs in FXTAS as the CGG^{exp}-mRNA becomes a substrate for the enzyme DICER, another RNase. Like DROSHA, it functions in the miRNA processing. DICER has been found to interact with the hairpin structure of the CGG^{exp}-mRNA by digesting the hairpin into potentially toxic miRNA-like CGG-repeat stretches (Sellier et al. 2013), (Handa 2003).

1.6.2 RAN translation

The second mechanism of toxicity arises from the translation of the CGG repeats in the *fmr1* mRNA in the absence of an AUG codon. Originally described in relation to CAG repeat expansions within the context of spinocerebellar ataxia type-8, this repeat-associated non-AUG (RAN) translation mechanism has been found to initiate from a near-cognate codon with a possibility of initiating translation in three different reading frames via frameshift. In most cases near-cognate codons differ from AUG by one nucleotide (GUG, CUG, UUG, ACG, etc.) with different efficiencies of driving translation (Kearse and Wilusz 2017). RAN translation in FXTAS occurs predominantly in the glycine frame (GGC: +1) and initiates independently of the downstream CGG repeat sequence at an ACG codon embedded in a poor Kozac consensus sequence (Sellier et al. 2017). Translation of polyalanine (FMRpolyA, GCG: +2) and polyarginine (FMRpolyR, CGG: +0) are also observed but with much less efficiency (Glineburg et al. 2018).

RAN translation is believed to occur regardless of the repeat length but a minimum size of 60 CGG repeats are required for the detection of the translated FMRpolyG. Shorter polypeptides are believed to be too unstable to persist in the cell. This is proposed as the main reason for the inability to observe FMRpolyG in the brain tissue of control individuals. On the other hand, as the size of FMRpolyG increases, it becomes more prone to aggregation forming small cytoplasmic aggregates (Gohel et al. 2019), (Glineburg et al. 2018). Because the minimum repeat threshold for its stability is already at the premutation repeat lengths, FMRpolyG is present in the intranuclear inclusions of FXTAS patients (Glineburg et al. 2018). Moreover, a protein gain-of-function mechanism has been demonstrated for FMRpolyG. The sequestration of the nuclear lamina protein Lap2β into intranuclear inclusions and the subsequent damage to nuclear architecture has been shown to result from a direct interaction with FMRpolyG (Sellier et al. 2017).

1.7 Mouse models of FXTAS

Over the years, several distinct types of mouse models have been generated in order to capture and study the phenotypes and pathologies associated with FXTAS patients. None of these models have succeeded in fully capturing all of the aspects of FXTAS. These mouse models include but not limited to, CGG^{exp} knock-in (KI) models, transgenic mice overexpressing *fmr1* with a normal sized repeat length (CGG^{norm}), tissue and cell type specific conditional mouse models and the tetracycline inducible models (Berman et al. 2014), (Hukema et al. 2015), (Castro et al. 2017), (Sellier et al. 2017). Some important examples are described below.

1.7.1 *fmr1* overexpressing model

FXTAS presents with an overexpression of the *fmr1* mRNA transcript and initially it was not clear whether this overexpression alone, independent of the repeat length could be responsible for the pathogenesis or the expanded repeat mRNA is the primary source of FXTAS. The *fmr1* overexpressing mice have been generated to test this possibility, in that an increase of 20- to 100-fold of the *fmr1* mRNA with a repeat length of 29xCGG has been found in all tissues tested. These mice, however, did not show any behavioral phenotypes differing significantly from their wild type (wt) controls. The work with this model suggested that the overabundance of *fmr1* mRNA is not the primary mechanism for toxicity in FXTAS, but rather the expression of the expanded repeats is the culprit (Berman et al. 2014).

1.7.2 Knock-in models

The first knock-in (KI) mouse model, the so-called “Dutch-mouse” was generated at the Erasmus University Medical Center in the Netherlands via the replacement of endogenous repeats in the murine *fmr1* with expanded CGG repeats of 98xCGG of human origin. When targeting the construct, the region flanking the repeats in the human *fmr1* was also included in the murine genome. The second KI model is the so-called “NIH-mouse” developed at the National Institutes of Health (NIH) via insertion of a 118xCGG tract into the 5’ UTR locus of the mouse *fmr-1* gene. NIH-mouse retains much more of the endogenous murine sequences flanking the repeats including an upstream TAA stop codon that is not present in the Dutch-mouse or humans (Berman et al. 2014), (Todd et al. 2013).

These KI models were successful in capturing some of the features of FXTAS seen in humans. Both models showed modest intergenerational instability of the repeats, increased *fmr1* mRNA expression and reduced FMRP levels in the brain. Ubiquitin-positive intranuclear inclusions were more prominent in the Dutch-mouse but readily detectable in both models. In the Dutch-mouse inclusions were present the hippocampus, cortex, cerebellum, olfactory bulb and hypothalamus but Purkinje cell loss was detected only in the NIH-mouse. At the behavior level, both models showed some level of memory deficits. Higher anxiety levels were observed in the Dutch-mouse but not in NIH-mouse. Similarly, motor decline with advancing age was only present in the Dutch-mouse but not in the NIH-mouse (Berman et al. 2014), (Qin et al. 2011), (Van Dam et al. 2005).

The differences observed between the Dutch-mouse and the NIH-mouse was mainly attributed to the differences in the flanking sequences of the CGG repeats that are inserted in the murine *fmr1*. This difference in the flanking regions was found to be responsible in the initiation of RAN translation. The flanking sequences of human origin found in the Dutch-mouse allows for generation of FMRpolyG, whereas the murine stop codon upstream of the repeats that is present in the NIH-mouse prevents it to produce FMRpolyG. Consequently, FMRpolyG was not detected in the inclusions formed by the NIH-mouse but only in the inclusions of the Dutch-mouse (Todd et al. 2013), (Berman et al. 2014).

1.7.3 The transgenic astroglia-specific model

The presence of intranuclear inclusions pathology in astrocytes raises the question how much of the features attributed to FXTAS originate from neurons and whether or not glia have substantial involvement in the generation of pathology. In order to address this question, the gfa2-CGG99-eGFP mouse model has been generated. The 99xCCG tract was found to be expressed in astroglia throughout the brain of these mice. This includes the cerebellar Bergmann glia, for which gliosis was reported in FXTAS patients (Wenzel et al. 2019), (Greco et al. 2006). Ubiquitin- and FMRpolyG-positive intranuclear inclusions as well as cytoplasmic inclusions were observed in the cells expressing the transgene. An interesting finding was that neurons in the brain of these mice also formed FMRpolyG-positive inclusions without any evidence of leakage (Wenzel et al. 2019). This is therefore, considered the first evidence of cell-to-cell transmission of repeat proteins in FXTAS; a phenomenon that has been reported for the hexanucleotide repeat expansions of the *c9orf72* gene that is linked to ALS and FTD. This transmission is believed to occur via one of the four proposed means; exosome-dependent, exosome-independent, anterograde and retrograde (Westergard et al. 2016). Behaviorally, these mice showed a paradoxical motor phenotype; impaired performance on the ladder-rung test and better performance on the Rotarod (Wenzel et al. 2019). These tests have been previously used to quantify the motor performance of KI-models (Qin et al. 2011), (Van Dam et al. 2005).

1.7.4 Inducible models

Inducible models have been generated for the purpose of investigating whether or not the progression of FXTAS can be halted if the expression of expanded CGG repeats is stopped at specific time points. Potential reversibility of the FXTAS phenotypes can be tested with these models to investigate the feasibility of therapeutic intervention strategies targeting the expression of the expanded repeats (Hukema et al. 2014), (Hukema et al. 2015). Two lines containing transgenes with different CGG repeat lengths in frame with an upstream tetracycline response element (TRE) were generated using the Tet-On system; a mouse line containing a normal repeat length of 11xCGG and another line with an expanded tract of 90xCGG. Both of these lines were generated with untargeted approach thus, the transgene loci are outside of the context of the endogenous *fmr1* (Hukema et al. 2015). When these mice are crossed with a driver line containing a reverse tetracycline-controlled transactivator (rtTA), the repeat tract can be expressed upon doxycycline (dox) administration in food or water in their bigenic offspring. The CGG tract expression is specific to the dox administered bigenic mice. Reporter expression has not been found either in the dox administrated monogenic mice or in the uninduced bigenic mice (Hukema et al. 2014).

The monogenic TRE-nCGG mice were first bred with hnRNP-rtTA driver mice to obtain a bigenic offspring with a ubiquitous CGG tract expression throughout the body. The bigenic hnRNP-rtTA/TRE-nCGG-eGFP mice expressing the 90xCGG tract unfortunately died prematurely before most of the FXTAS related phenotypes can be investigated. The premature death was linked to mitochondrial dysfunction that caused liver damage only upon expression of the expanded CGG repeats. The 11xCGG expressing bigenic mice remained unaffected. Mitochondrial dysfunction has indeed been reported with FXTAS but this kind of deleterious effect of the expanded CGG expression on liver function does not occur in human patients (Hukema et al. 2014).

A second dox-inducible bigenic line was generated by crossing the TRE-nCGG monogenic mice with a brain-driven prion protein (PrP) driver line. The use of PrP driver confines the expression of the CGG tract to the central nervous system with reporter expression both in neurons and glia. Strongest expression was seen in cerebellum, hippocampus and striatum. Dox quickly crosses the blood-brain-barrier and the reporter expression can be detected, as little as two days after starting dox-induction. Upon dox-induction both the 90xCGG and

11xCGG transcript levels were more than double of the endogenous *fmr1* mRNA. The bigenic offsprings that express the expanded repeats capture many of the FXTAS-related pathology and phenotype (Hukema et al. 2015), (Castro et al. 2017).

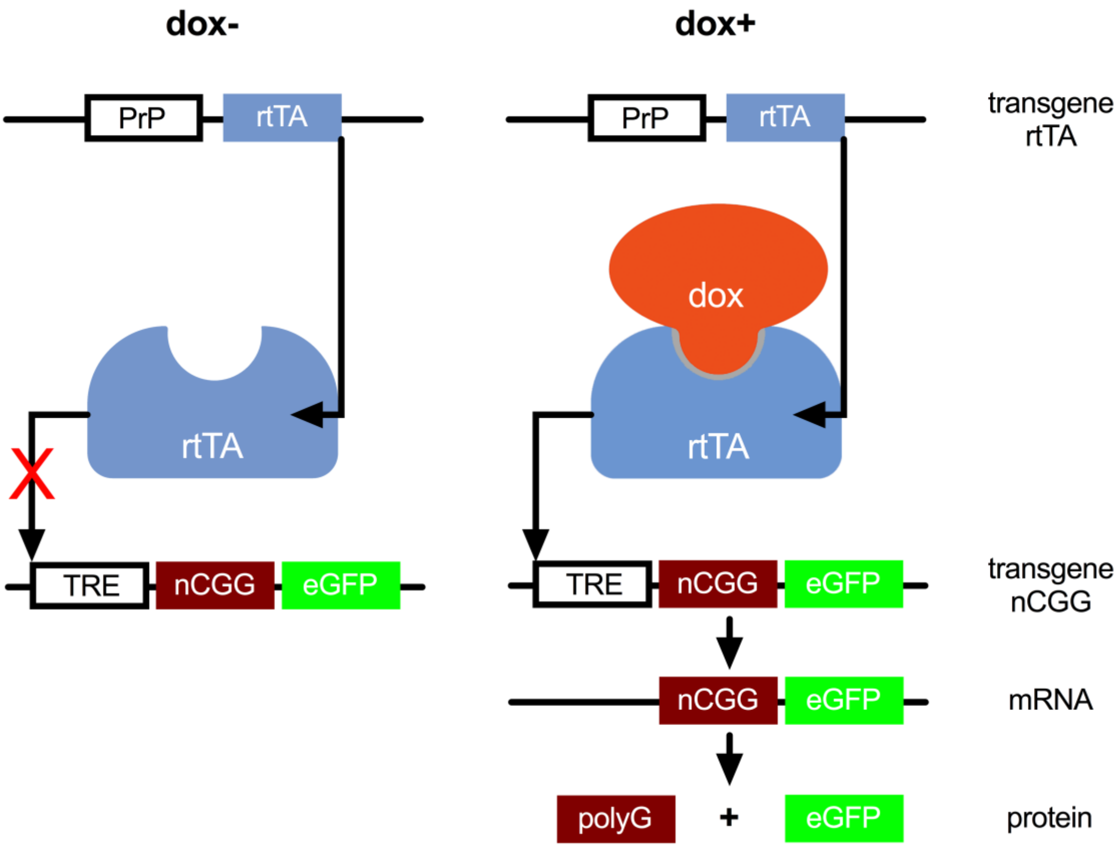

Figure 1.3: The Tet-On system under the PrP driver that controls CGG expression in the bigenic PrP.90xCGG and PrP.11xCGG mice

The PrP promotor drives the expression of rtTA in the brain. However, rtTA protein binds and activates the TRE operator only if bound by dox. The activation of the TRE operator allows for expression of the CGG repeats. Consequently, CGG repeats can translated via RAN translation and the eGFP-reporter is synthesized from its own canonical AUG codon (Adapted from Hukema et al. 2015).

1.7.4.1 Features of the inducible PrP.90xCGG model

The PrP-rtTA/TRE-nCGG-eGFP (PrP.nCGG for short) has been investigated for FXTAS pathology and related phenotypes. FXTAS is modeled in the dox-induced PrP.90xCGG mice and either the PrP.11xCGG or the uninduced PrP.90xCGG animals are routinely used as controls. The dox-induced PrP.90xCGG mice form ubiquitin-positive intranuclear inclusions throughout the brain, especially in the regions with high reporter expression and these inclusions are also positive for the RAN translation product FMRpolyG. The highest inclusion load was seen in the cerebellum lobule X with increasing numbers and size as the dox-induction duration was extended. The dox-induced PrP.11xCGG and the uninduced PrP.90xCGG mice do not form inclusions (Hukema et al. 2015).

Behaviorally, PrP.90xCGG mice showed deficits in motor performance after 12 weeks of dox-induction but not after 8 weeks. The same was true for gait and anxiety measures. An abnormal gait and higher anxiety levels have been described after 12 weeks of exposure to dox. However, after the shorter 8 weeks of dox-induction these behavioral changes were not observed in the PrP.90xCGG mice. None of these parameters have been reported to be affected in the PrP.11xCGG mice upon 12 weeks of dox-induction (Castro et al. 2017). Additionally, impairments in visuomotor tasks (optokinetic reflex and vestibulo-ocular reflex) were identified in the PrP.90xCGG mice, not upon 8 weeks but after 20 weeks of dox exposure. This specific reflex is strongly connected to the function of the cerebellar flocculus and this deficit is believed to reflect the high reporter expression and inclusion load in that region (Hukema et al. 2015).

1.7.4.2 Reversibility of the features of PrP.90xCGG model

The inducible nature of the PrP.90xCGG model allows for investigation of potential recovery both in pathology and behavior upon transgene shut down. For this purpose, all studies involving the model used a so-called “wash-out” period, a 12-week dox-free period following a dox-induced period. When mice are subjected to this wash-out period reporter expression becomes undetectable, whereas inclusions mostly. However, a region-dependent decrease in the number of inclusions has also been reported after the wash-out following a 12-week dox-induction period for the dentate gyrus (DG) and of the hippocampus and basolateral amygdala (BLA). On the other hand, the number of inclusions in the cerebellum lobule X remained unchanged despite the wash out. However, there is a disagreement between the published studies on whether or not the inclusion load in the cerebellum lobule X decreases after the wash-out following the shorter 8-week of dox exposure (Hukema et al. 2015), (Castro et al. 2017).

Behavioral phenotyping within this wash-out scheme complemented the findings on the pathology with some interesting implications for the progression of FXTAS. The wash-out introduced after 12 weeks of dox exposure did not rescue the motor deficits, including the gait abnormalities but corrected the heightened anxiety (Castro et al. 2017). The wash-out period also attenuated the visuomotor deficits when introduced after the initial 8-week dox-induction (Hukema et al. 2015). However, motor deficits have been reported after the wash-out that were not present when the mice were tested right after the 8-week dox-induction. This result was interpreted to be suggestive of a further modulation of deterioration upon the initial genetic insult by additional factors other than inclusion formation (Castro et al. 2017).

1.8 Behavioral domains relevant to PrP.90xCGG model

Use of model organisms to investigate pathology and functional alterations is a critical step towards identification of disease genes, for a better understanding of the underlying mechanisms and complex genetic interactions that result in disease phenotypes (Aitman et al. 2011). Comprehensive behavioral phenotyping can target different behavioral domains by the use of various paradigms, to dissect functions that are associated with different brain structures.

For FXTAS one of the most studied domains is the motor domain. Functional alterations related to this domain can be addressed by using different tests; each with differential sensitivity to abnormal changes in the specific brain regions involved. Rotarod is the most widely used test in behavioral phenotyping of FXTAS models (Qin et al. 2011), (Van Dam et al. 2005), (Wenzel et al. 2019), (Castro et al. 2017). For the Rotarod test, the mouse is placed on a rotating horizontal rod, where it has to walk forwards to remain on the rod and not fall off. The rotarod tests are sensitive to alterations in muscle tone, balance, motor coordination, grip strength and endurance. There are two variants of the rotarod test; constant speed test and acceleration test. Fatigue is believed to influence the results of the acceleration test that is, it requires more endurance, whereas constant speed test is considered to be more sensitive to subtle biological changes governing balance and coordination. Deficits in Rotarod tests are associated with alterations in cerebellar and spinal cord function. Rotarod tests can, with a substantially lower sensitivity, detect abnormalities also in the basal ganglia functioning (Mann and Chesselet 2015).

Gait analysis based on pawprint patterns is another test that is sensitive to changes in motor coordination and synchrony in walking (Mann and Chesselet 2015) and has been used with the PrP.90xCGG model to investigate the presence of ataxic gait (Castro et al. 2017). One of the typical parameters assessed from the pawprint patterns is the stride length. This parameter is widely used for phenotyping in the PD research and reductions in stride length have been correlated with reduced nigrostriatal dysfunction (Fernagut et al. 2002), (Mann and Chesselet 2015). Another type of behaviorally relevant area to the PD research in relation to nigrostriatal dysfunction is sensorimotor gating. Sensorimotor gating is typically measured in hearing rodents with an acoustic paradigm called prepulse inhibition of the acoustic startle reflex. Prepulse inhibition (PPI) is defined as the attenuation of the amplitude of a startle reflex that is induced by a sudden intense stimulus, if preceded by a weaker sensory stimulus. The amount of inhibition created by the weaker stimulus is used as a measure of sensorimotor gating. PPI is believed to be mediated by a complex cortico-striato-pallidopontine (CSPP) circuitry. Deficits in PPI have been described for neuropsychiatric disorders as well as for diseases of the basal ganglia and have been linked to reduced density of dopamine transporters and reduced dopamine levels in the striatum (Swerdlow, Braff, and Geyer 2016), (Zoetmulder et al. 2014).

Another domain relevant to FXTAS models is anxiety. Anxiety-like phenotypes have been investigated in many of the FXTAS models, including the PrP.90xCGG model. Anxiogenic behavior observed in mice, has been linked to the presence of inclusions in the amygdala, a key structure related to emotional processing (Castro et al. 2017). Anxiogenic behavior can be quantified by various paradigms in rodents. These include light-dark transition test, open field and marble burying. In the light-dark transition test, mice are subjected to two-compartment setup, a dark compartment versus an illuminated chamber. Mice can transition between compartments via a small opening and freely explore the setup. The time spent in the illuminated chamber and the number of entries to that chamber are considered as indices of bright-space anxiety in mice, i.e. less time spent reflects higher anxiety-levels (Takao and Miyakawa 2006). The open field test is typically used to test spontaneous locomotor activity in rodents by letting them freely explore a bare, wall-enclosed arena and recording the total ambulatory distance during a specific time interval. However, by compartmentalizing the arena, thigmotaxis or the tendency to remain close to vertical surfaces, can be quantified. Increased thigmotaxis in mice is considered as a measure of increased anxiety (Seibenhener and Wooten 2015).

Compulsive-like behaviors related to obsessive-compulsive disorder (OCD) or autism spectrum disorder (ASD) can be quantified using a marble burying test in mice. In this test, marbles are placed in a cage containing fresh bedding and mice are allowed to freely explore the cage for a specific time interval. The number of marbles a mouse buries are considered to be reflective of compulsive-like repetitive behaviors and anxiogenic behavior alike. This is due to the fact that, the test is sensitive to anxiolytic drugs as well as different types of antidepressants used in the treatment of both anxiety and OCD. Therefore, marble burying is not a recommended stand-alone test for anxiety (Angoa-Pérez et al. 2013), (Hayashi et al. 2010).

Another important domain concerning research on FXTAS models is learning and memory, as many FXTAS patients present with memory deficits along with cognitive decline. Also, the hippocampus, a brain region that is particularly important for memory processes is markedly impacted by the presence of inclusions in human patients as wells as in the PrP.90xCGG mice (Greco et al. 2002), (Hukema et al. 2015), (Castro et al. 2017). One important paradigm of the behavioral research on learning and memory is the cued and contextual fear conditioning. This test assesses the ability of mice to learn and remember an association between environmental cues, usually an acoustic tone and aversive experiences like a mild foot-shock.

The environmental context, in which the aversive experience happens constitutes a contextual association, whereas the presence of an acoustic cue coupled with the aversive experience constitutes an association in relation to the cue. Mice that are successfully trained to this paradigm typically respond with a freezing behavior upon presentation of the reminders of the aversive experience and the level of freezing is considered as an index of fear memory. This type of memory is believed to recruit both amygdala and hippocampus (Shoji et al. 2014), (Raybuck and Lattal 2011). A variation of the paradigm is trace fear conditioning, in which the acoustic cue is not coupled with the foot-shock but rather separated by a time interval that is called the trace period. This variation paradigm is believed to be more strongly dependent on hippocampus than amygdala (Lugo, Smith, and Holley 2014), (McEchron et al. 1999), (Raybuck and Lattal 2011).

1.9 Treatment strategies for FXTAS

Currently, the only available option for patients with a FXTAS diagnosis is supportive treatment, directed at component symptoms of the disorder that cause the most serious problems for each individual. This approach aims to increase the quality of life of the patients and limit their suffering via applying treatment strategies developed for various other disorders that have phenotypic overlap with FXTAS. One important example of this is dopaminergic medications also used for primary Parkinson's disease. Some but not all FXTAS patients have found to be dopamine responsive (Hall et al. 2016). Three controlled drug trials designed specifically for FXTAS have also been performed. Memantine (ID: NCT00584948), an US Food and Drug Administration (FDA) approved drug for Alzheimers's disease (AD), was the first drug to be tested on patients for its potential to improve neurologic and cognitive symptoms of FXTAS patients. The study found that memantine had no benefits for FXTAS patients (Seritan et al. 2014). Citocoline (ID: NCT02197104), an oral nutritional supplement that has been initially investigated for treatment of stroke, has also been tested on FXTAS individuals for its potential neuroprotective properties. The preliminary data suggested that citocoline may be effective in stabilizing the progression of the disease (unpublished conference proceedings by D. Hall; Department of Neurological Sciences, Rush University, Chicago, USA – International Congress of International Parkinson and Movement Disorder Society, 2018, Hong Kong), (Gareri et al. 2015). The third drug trial was involved allopregnanolone (ID: NCT02603926), a neurosteroid tested for its potential regeneration and repair promoting properties. The study has found some improvement in the cognitive functioning of the patients and that allopregnanolone partially alleviated neurodegeneration (J. Y. Wang et al. 2017).

Although current treatment strategies available for FXTAS patients are very limited, there is a substantial effort in the field towards development of novel strategies. Most strategies involve targeting either one or both of the two main mechanisms of the FXTAS pathogenesis; the CGG^{exp} mRNA and RAN translation. Efforts concentrated on screening of small molecule libraries and testing bioactive compounds with potential abilities to inhibit toxicity in FXTAS cell and animal models (Qurashi et al. 2012), (Green et al. 2019). Small molecules including designer compounds (W.-Y. Yang et al. 2015) that bind and assemble on the CGG^{exp} repeat hairpin structure have been found to improve FXTAS associated defects not only by inhibiting protein sequestration but also by impeding the translation of the repeat sequences by the RAN translation machinery (Disney et al. 2012), (Tran et al. 2014), (Bernat and Disney 2015). Another class of compounds that target RAN translation initiation directly, were also successful in limiting the generation of FMRpolyG (Green et al. 2019). Oligonucleotides with antisense sequences to the CGG-repeats are also another possibility to target the hairpin structure, thereby interfering with both protein sequestration and RAN translation (Tran et al. 2014), (W.-Y. Yang et al. 2015). Some of the abovementioned compounds are, however, toxic by nature and the mechanisms they successfully interfere with can also result in unwanted reduction of the canonical translation that produces FMRP (Green et al. 2019), (Tran et al. 2014), (Bernat and Disney 2015). Endogenous modifiers that act on the CGG^{exp} mRNA have also been screened as potential targets and the disruption of a particular RNA helicase has been shown to selectively reduce toxicity related to RAN translation in cell and animal models (Linsalata et al. 2019).

1.10 Autophagy in disease states

Autophagy is a lysosomal degradation pathway conserved in various eukaryotes that is utilized to recycle intracellular components with essential roles in development, differentiation, homeostasis and survival. Autophagy is typically triggered by the lack of nutrients under the inhibitory control of mammalian target of rapamycin (mTOR) pathway and provides the nutrients that are vital to the cell’s survival via its recycling action. However, the same mechanism can also rid the cell of damaged organelles, invading organisms, misfolded proteins and aggregations in a house-keeping action. Dysfunctional autophagy has been associated with a number of diseases ranging from cancers to metabolic disorders, from neurodegenerative diseases to infections. Autophagy initiates with recruitment of proteins of the ATG family to a double-membraned phagophore tightly associated with LC3 and expands with additionally recruited essential proteins. The structure finally closes to form the autophagosome. The autophagosome can then collect cytoplasmic cargo, an action mediated by p62 and finally merge with the lysosome. In the autolysosome, the cargo and p62 is degraded by lysosomal proteases with the help of the hydrolytic environment and released back into the cytoplasm (Luo et al. 2016), (Liu et al. 2016). Unlike UPS, autophagy can degrade bulk cargo, such as aggregated mutant proteins. Aggregated proteins are poor substrates for the UPS because of the narrow pore of the proteasomal barrel. On the other hand, autophagic degradation occurs strictly in the cytoplasm (Levine and Kroemer 2008). For nuclear aggregates to be degraded by autophagy they must be exported via the nuclear pore complex that does not allow for the passage of structures greater than 39 nm in diameter. This holds especially true for non-dividing cells, in which the nuclear envelope remains intact for extended periods of time. In many triplet expansion diseases, the size of nuclear intranuclear inclusions exceed this limit. On the other hand, a hypothetical egress of nuclear aggregates (EGNA) pathway that allows export of nuclear aggregates via a budding mechanism has also been postulated (Rose and Schlieker 2012).

Pharmacological activation of autophagy has been shown to reduce the levels of aggregated as well as soluble forms of mutant proteins associated with neurodegenerative disorders, including Huntington's disease (HD) and several types of spinocerebellar ataxias (Levine and Kroemer 2008). Neuron specific inactivation of essential ATG genes, however, results in accumulation of aggregated proteins that form ubiquitinated inclusion bodies (Thorburn 2018). Rapamycin and trehalose are two examples of inducers of autophagy frequently used in research related to neurodegenerative diseases with aggregation pathology. Rapamycin is an mTOR-dependent autophagy inducer that has been shown to successfully attenuate aggregate formation in many experimental models of HD, Parkinson's disease (PD) and Alzheimer's disease (AD) (Bové, Martínez-Vicente, and Vila 2011) and is currently under evaluation for the treatment of amyotrophic lateral sclerosis (ALS) in a controlled clinical trial (NCT03359538). On the other hand, trehalose is believed to a activate autophagy by blocking glucose import to the cells thereby generates a starvation-like state (Mardones, Rubinsztein, and Hetz 2016). Trehalose has also been successfully applied in various disease models and was found to decrease polyglutamine inclusions and associated pathology in a mouse model of HD (Tanaka et al. 2004). Another example of successful application of trehalose is in a mouse model of ALS. In this study, trehalose was found to increase autophagy levels via oral application and alleviate motor deficits in the early stages of the disease but not as the disease progressed further (Y. Li et al. 2015).

1.11 Antisense oligonucleotides in neurodegeneration

Antisense oligonucleotides (ASOs) are short chemically modified compounds with a Watson-Crick base-pairing mode of recognition for their RNA target. Therapeutic ASOs can recruit several types of biological mechanisms to inactive their target. Upon ASO recognition and binding the target mRNA can either be degraded or be functionally hindered by simple occupancy. ASOs with RNA backbones activate endogenous RISC pathway for cleavage, whereas single-stranded DNA ASOs depend on the RNase H1 mechanism that cleaves DNA:RNA hybrids. Depending on the antisense sequence and chemical modification, ASOs can be targeted to specific sites on the target mRNA, such as loci proximal to exon-intron junctions and act as steric blockers regulating splicing events without causing the degradation of the mRNA (Wan and Seth 2016).

Pharmacokinetic properties and biodistribution of ASOs are largely driven by the chemistry of their backbone; unmodified nucleic acids are rapidly degraded by nucleases. Moreover, ASOs do not cross the blood-brain-barrier. However, biodistribution, efficient uptake and stability are not the only challenges faced by an *in vivo* antisense therapy. The transcription level of the target gene plays a critical role towards the determination of appropriate dosage of the ASOs to be delivered (Geary et al. 2015). Despite these challenges, ASOs have been successfully used as potential treatment strategies on experimental models of neurodegenerative diseases with one antisense drug, nusinersen, already been approved for the treatment of spinal muscular atrophy by FDA in 2016 (Bennett, Krainer, and Cleveland 2019). Within the context of triplet expansion diseases, a most relevant *in vivo* application example is the targeting of the CAG-repeats in two independent mouse models of HD. In this study, the ASO was delivered via intracerebroventricular infusion resulting in a broad range distribution throughout the brain. Depending on the brain region, this ASO has reduced the soluble mutant huntingtin levels up to 30% and the aggregation fraction up to 58%. This molecular correction was also accompanied by improved motor performance on the Rotarod. Moreover, the mutant huntingtin levels were found be suppressed for up to 18 weeks post-infusion (Datson et al. 2017).

1.12 Aims and motivation

The initial phenotyping studies on the PrP.90xCGG model has investigated different dox-induction timelines ranging from 8 to 28 weeks together with a recovery interval of 12 weeks also known as the wash-out period (Hukema et al. 2015). This initial effort, however, has been mainly based on histological investigation of intranuclear inclusion profiles at various timepoints with little emphasis on the behavior. The more extensive behavioral phenotyping study came later on and identified an anxiety-like behavior that can be rescued after a wash-out period and motor deficits that are not amenable to rescue despite the wash-out (Castro et al. 2017). However, this study has concentrated on the 8 and 12-week induction schedules starting at weaning with a 12-week wash-out period and failed to capture the full range of phenotypes associated with the premutation that the PrP.90xCGG model may manifest. On the other hand, the exploration of two different induction intervals together with a wash-out period resulted not only in the identification of key behavioral phenotypes associated with the premutation but also revealed that these phenotypes may require an incubation period to become apparent. More specifically, although after the shorter 8-week induction interval the mice remained free of any deficits, they started to show motor deficits after the wash-out period that was originally intended as a recovery period. From the inclusion pathology point of view, the wash-out period did not lead to a lower number of inclusions in the most parts of the brain including the cerebellum. It seems therefore that phenotypes -particularly in this case motor phenotype- arise from an interaction between the duration of dox-induction and the age of the mice in the inducible PrP.90xCGG mouse model despite being an overexpressing model.

Based on these observations, I hypothesized that further phenotypes related to the premutation can be identified in the brain specific PrP.90xCGG model by employing additional induction schedules that allow the mice to be tested after various induction duration and age combinations. To test this hypothesis and to extend the phenotyping efforts that has already been done with this model, I have used two additional induction schedules. First, a longer induction schedule with a duration of 24 weeks starting from the weaning that should allow for investigation of later phenotypes that may arise with increasing age and induction duration. Therefore, this schedule corresponds to an extension to the investigation of FXTAS-related phenotypes in PrP.90xCGG model. Second, I have used an early induction schedule that allows the mice to be tested after the common 12-week induction period but at a younger age. This schedule aims to capture a pre-motor era of the premutation with the use of younger animals without sacrificing from the power of the longer 12-week induction. Therefore, this early induction timeline may serve as a model for FXAND. There are no studies reported addressing the premutation features within the context of FXAND in any of the available mouse models at the time of writing of this thesis.

Several symptomatic treatment strategies exist for *Fmr1*-premutation disorders with limited success. However, there is no cure. A limited number of human studies involving testing of FDA approved drugs such as memantine (Seritan et al. 2014) have also been conducted within the context of FXTAS but failed to elicit a substantial recovery. The weakness of this approach is perhaps, selection of drugs based on their potential effects on certain kinds of symptoms but not as a strategy targeting pathological processes underlying FXTAS. Several targeted drug treatment strategies including small molecule inhibitors of RAN translation have also been tried in FXTAS *in vitro* models for their potential to decrease the formation of intranuclear inclusions. Despite the success in reducing the aggregation, these studies suffered from highly toxic nature of the compounds that have been tested (Green et al. 2019). Studies investigating viable treatments for FXTAS at the preclinical level are rare with limited translational potential due to the use of technologies such as gene editing (C. Yrigollen and Davidson 2019). Strategies that target pathological processes identified for FXTAS involving compounds with low *in vivo* toxicity represent an area that is not well explored. Preclinical studies based on this approach are urgently needed and they may represent the highest translational value among all strategies. For the development of novel therapeutics for FXTAS, I hypothesized that compounds with low toxicity that are able to target pathological processes specific to FXTAS with success, -particularly in this case the formation of intranuclear inclusions- will also affect the behavioral outcomes of the dox-induced PrP.90xCGG mice positively.

In order to test my hypothesis, I have designed two distinct treatment strategies based on the approach described above. The first strategy targets alternative protein degradation pathways to complement ubiquitin proteasome system that is known to be dysfunctional in FXTAS (Oh et al. 2015). This strategy involves targeting of FMRpolyG-related toxicity via oral supplementation of trehalose, a disaccharide that considered to be safe for human consumption and is recognized as an autophagy inducer (Mardones, Rubinsztein, and Hetz 2016). Because autophagy targets cytoplasmic cargo (Levine and Kroemer 2008), my secondary hypothesis is that meaningful intervention is only possible when it starts at the early stages of the pathogenesis. FMRpolyG will only be degraded via autophagy as it forms small cytoplasmic aggregates and it will be inaccessible once it becomes part of the stable inclusions in the nucleus. The second strategy targets the CGG-repeats in the mRNA and inactivates it via the use of highly stable antisense oligonucleotides (ASOs) that have low toxicity. This strategy potentially targets not only the RAN translation but also the RNA toxic gain-of-function mechanism. The application is based on intracerebroventricular infusion because of the blood-brain barrier impermeability to ASOs. However, this limitation does not substantially decrease the translational value of the antisense therapy with the possibility of intrathecal delivery (Bennett, Krainer, and Cleveland 2019) and with the advancement of technologies making the systemic delivery of ASOs more feasible (Zeniya et al. 2018). Both of the proposed strategies have the potential to decrease the formation of aggregates in the brain and thereby to improve the behavioral outcome.

2 Materials and Methods

2.1 Materials

2.1.1 Chemicals

Acrylamid 30%	Carl Roth, Karlsruhe, DE
Agarose	Peqlab, Erlangen, DE
Bovine serum albumin (BSA)	Carl Roth, Karlsruhe, DE
β-mercaptoethanol	Serva, Heidelberg, DE
$CaCl_2$	Carl Roth, Karlsruhe, DE
DAPI (1 µg/ml)	Sigma-Aldrich, St. Louis, MO, USA
dNTPs	Thermo Fisher Scientific, Waltham, MA, USA
DMSO	Carl Roth, Karlsruhe, DE
Donkey serum	Vector laboratories, Burlingame, CA, USA
Doxycycline hyclate (HPLC grade)	Sigma-Aldrich, St. Louis, MO, USA
EDTA	Carl Roth, Karlsruhe, DE
Ethidium Bromide	Carl Roth, Karlsruhe, DE
Ethanol	Carl Roth, Karlsruhe, DE
Glucose	Carl Roth, Karlsruhe, DE
Glycine	Sigma-Aldrich, St. Louis, MO, USA
Goat serum	Vector laboratories, Burlingame, CA, USA
Shandon Immu-mount	Thermo Fisher Scientific, Waltham, MA, USA
Isoflurane	Nicholas Piramal, Mumbai, IN
Isopentane	Carl Roth, Karlsruhe, DE
Isopropanol	Carl Roth, Karlsruhe, DE
KCl	Carl Roth, Karlsruhe, DE
Ketamine/Xylazine	Sigma-Aldrich, St. Louis, MO, USA
$MgSO_4$	Carl Roth, Karlsruhe, DE
NaCl	Carl Roth, Karlsruhe, DE
$NaHCO_3$	Carl Roth, Karlsruhe, DE
Na_2HPO_4	Carl Roth, Karlsruhe, DE
PCR Direct Lysis Buffer	Peqlab, Erlangen, DE
PFA	Carl Roth, Karlsruhe, DE

PLL (Poly-L-Lysine)	Sigma-Aldrich, St. Louis, MO, USA
Proteinase K	Carl Roth, Karlsruhe, DE
Protifar protein powder	Nutricia, Zoetermeer, NL
Rabbit serum	Vector laboratories, Burlingame, CA, USA
Sucrose	Sigma-Aldrich, St. Louis, MO, USA
Tablet Pierce protease inhibitor	Thermo Fisher Scientific, Waltham, MA, USA
Tissue-Tek® O.C.T.™ compound	Sakura Finetek, Alphen aan den Rijn, NL
Trehalose	FormMed HealthCare, Frankfurt Am Main, DE
Tris-HCl	Carl Roth, Karlsruhe, DE
Tri-sodium citrate.$2H_2O$	Carl Roth, Karlsruhe, DE
Triton-X	Serva Electrophoresis, Heidelberg, DE
Tween-20	Carl Roth, Karlsruhe, DE

2.1.2 Enzymes and kits

Avidin/biotin blocking kit	Vector laboratories, Burlingame, USA
Bradford Assay	Bio-Rad Laboratories Inc., Hercules, CA, USA
Brightvision poly-HRP-linker	Immunologic, Duiven, NL
DAB substrate	Dako-Agilent, Santa Clara, CA, USA
DreamTaq-polymerase	Thermo Fisher Scientific, Waltham, MA, USA
Enhance High Fidelity-polymerase	Roche, Basel, CH
M.O.M. Immunodetection Kit	Vector laboratories, Burlingame, CA, USA

2.1.3 DNA and protein standards

Gene Ruler 100 bp Plus DNA Ladder	Thermo Fisher Scientific, Waltham, MA, USA
Gene Ruler 1 kb DNA Ladder	Thermo Fisher Scientific, Waltham, MA, USA
Paige Ruler Plus Protein Ladder	Thermo Fisher Scientific, Waltham, MA, USA

2.1.4 Antisense oligonucleotides

11 nucleotide-long ASO-CCG was composed of 10 LNA units and 2'OMe unit at 3' end. All LNA positions were phosphorothiorated. The ASO-CCG has the sequence 5'-CCGCCGCCGCC-3'. ASOs were synthetized and purified by Kaneka Eurogentec S.A., Seraing, Belgium. ASO-CCG was obtained through a collaboration with M. Derbis; K. Sobczak's group, AMU, Poznań, Poland.

2.1.5 Primary antibodies

mouse-anti-tyrosine hydroxylase (Th) (1:100, sc-25269, Santa Cruz Biotech., Dallas, TX, USA)

goat-anti-green fluorescent protein (GFP) (1:100, ab6673, Abcam, Cambridge, UK)

mouse-anti-p62/sqstm1 (1:100, ab56416, Abcam, Cambridge, UK)

rabbit-anti-ubiquitin (1:250, Z0458, Dako-Agilent, Santa Clara, CA, USA)

rabbit-anti-dopamine transporter (DAT) (1:250, ab184451, Abcam, Cambridge, UK)

rabbit-anti-LC3 A/B (1:1500, 12741S, Cell Signaling Technology, Danvers, MA, USA)

mouse-anti-alpha tubulin (1:10000, T6199, Sigma-Aldrich, St. Louis, MO, USA)

mouse-anti-FMRpolyG (8FM) (1:200, kind gift from N. Charlet-Berguerand; IGBMC, University of Strasbourg, France. 8FM described previously in Buijsen et al. 2014)

2.1.6 Secondary antibodies

Biotinylated goat-anti-rabbit (1:250, Vector Laboratories, Burlingame, CA, USA)

Biotinylated donkey-anti-goat (1:250, Vector Laboratories, Burlingame, CA, USA)

Cy3-Streptavidin (1:1000, Jackson ImmunoResearch Europe Ltd., Cambridgeshire, UK)

Cy5-Streptavidin (1:1000, Jackson ImmunoResearch Europe Ltd., Cambridgeshire, UK)

IRDye 680RD goat-anti-mouse (1:15000, LI-COR Inc., Lincoln, NE, USA)

IRDye 800CW goat-anti-rabbit (1:15000, LI-COR Inc., Lincoln, NE, USA)

2.1.7 Animal care

R/M-H V-1534	Ssniff Spezialdiäten, Soest, DE
R/M-H-A153-D04004	Ssniff Spezialdiäten, Soest, DE
Macrolon standard cages (type II long)	Techniplast, Hohenpeissenberg, DE
Bepanthen eye ointment	Bayer, Leverkusen, DE
Bepanthen wound ointment	Bayer, Leverkusen, DE
Paladur dental cement	Heraeus Kultzer, Wehrheim, DE
Perma-Hand suture	J&J Medical Devices, Norderstedt, DE

2.1.8 Equipment

Genotyping

Veriti thermal cycler	Applied Biosystems, Darmstadt, DE

Stereotactic surgery

Stereotactic frame	World precision instruments, Sarasota, FL, USA

Surgical instruments	Carl Roth, Karlsruhe, DE
Micro drill	World precision instruments, Sarasota, FL, USA
Isoflurane anesthesia system	Rothacher Medical, Heitenried, CH
28G infusion cannula	Plastics1, Roanoke, VA, USA
Alzet osmotic pump model: 1004	Durect, Cupertino, CA, USA
Behavior	
Rotarod	Ugo Basile, Varese, IT
Open field	Stoelting Co., Wood Dale, IL, USA
Acoustic startle reflex system	Med Associates Inc., St. Albans, VT, USA
Fear conditioning system	TSE, Bad Homburg, DE
Tissue processing	
Cryostat, CM 1950	Leica, Nussloch, DE
Dounce homogenizer	Wheaton, Millville, NJ, USA
Histology	
DMI 6000 epifluorescence microscope	Leica, Nussloch, DE
Microscope slides	Carl Roth, Karlsruhe, DE
Slide holder	NeoLab, Heidelberg, DE
Cuvettes	NeoLab, Heidelberg, DE
Western blotting	
Odyssey Scanner	LI-COR Inc., Lincoln, NE, USA
PVDF membrane (Immobilon-FL)	Merck Millipore, Burlington, MA, USA
Wet blotting system	Bio-Rad Laboratories Inc., Hercules, CA, USA
Membrane holders	LI-COR Inc., Lincoln, NE, USA
Other	
Glassware	Carl Roth, Karlsruhe, DE
Plasticware	Brand, Wertheim, DE
Micro-Amp Fast Reaction Tubes	Life Technologies, Darmstadt, DE
Sanyo Ultra Low (-86°C)	Ewald Innovationstechnik, Bad Nenndorf, DE
Fridge/Freezer (KU 2407/GU4506)	Liebherr Hausgeräte, Ochsenhausen, DE
Centrifuge Haraeus Pico 17	Thermo Fisher Scientific, Waltham, MA, USA
Vortexer – Lab dancer	VWR, Darmstadt, DE
Water bath	Lauda, Lauda-Königshof, DE

Scale	Sartorius, Göttingen, DE
Hot plate	Medite, Burgdorf, DE

2.1.9 Software

Adobe Photoshop	Adobe Systems, San Jose, CA, USA
AnyMaze Behavior Tracking Software	Stoelting Co., Wood Dale, IL, USA
BioRender online basic	BioRender, Toronto, ON, CA
Fiji (ImageJ)	Open source
LAS AF software	Leica Microsystems, Nussloch, DE
Odyssey ImageStudio	LI-COR Inc., Lincoln, NE, USA
Matlab	MathWorks, Natick, MA, USA
Mendeley	Mendeley Ltd., London, UK
Microsoft Office	Microsoft, Redmond, WA, USA
Prism, ver. 8	GraphPad, San Diego, CA, USA
SOF-825 startle software	Med Associates Inc., St. Albans, VT, USA
TSE Fear Conditioning Software V08.03	TSE, Bad Homburg, DE

2.2 Methods

2.2.1 Mice

All transgenic mice were generated in the Erasmus Medical Center, Rotterdam, the Netherlands as previously described (see Hukema et al. 2014 and Hukema et al. 2015). The wild type C57BL/6JBomTac (for short BL6) mice were purchased from M&B Taconic, Germany. All mice were bred and maintained in the animal facility of the Institute of Biology, Otto von Guericke University Magdeburg, Germany under standard laboratory conditions. The facility was kept on an inverted 12-hour dark/light cycle (lights off at 7 am with 30 minutes of dim phase), with regulated room temperature (21°C) and humidity (50-60%). Mice were weaned four weeks after birth and were group-housed 2-3 mice per cage with *ad libitum* food (R/M-H V- 1534 or R/M-H-A153-D04004 +4600 mg/kg doxycycline hyclate, ssniff) and water (plain or containing 5% sucrose or containing 5% sucrose and 4 mg/ml doxycycline hyclate). After weaning tail biopsies (<0.3 cm) were collected for genotyping and earmarks were made for mouse identification in group-housed mice. All animal experimental procedures were approved under local ethics committee (CEEA #42502-2-1219UniMD) and met the guidelines of the local and European regulations (European Union directive no. 2010/63/EU). All animal experiments were performed during the active phase (lights off) of the mice.

2.2.1.1 Mouse lines and breeding scheme

Three separate transgenic lines were kept as separate mouse colonies: PrP-rtTA monogenic driver line, TRE-11CGG-eGFP monogenic target line and TRE-90CGG-eGFP monogenic target line. These lines have been generated via an untargeted gene insertion approach to create a Tet-On system (see Fig.1.3. and Hukema et al. 2015). PrP-rtTA driver line contains the tetracycline-controlled transactivator (rtTA) that operates under a prion protein promotor (PrP), whereas TRE-11CGG-eGFP and TRE-90CGG-eGFP lines contain a tetracycline response element (TRE) in frame with a CGG-repeat stretch and eGFP. In order to generate the mice that were used in the experiments, males from the PrP-rtTA driver line were bred with females of either TRE-11CGG-eGFP or TRE-90CGG-eGFP target lines. This generates the bigenic line called PrP-rtTA/TRE-11CGG-eGFP (for short PrP.11xCGG) and PrP-rtTA/TRE-90CGG-eGFP (for short PrP.90xCGG) respectively.

2.2.1.2 Doxycycline, trehalose and ASO treatment schedules

For phenotyping experiments, three different doxycycline (dox) induction schedules were used: A 24-week continuous dox-induction that starts with the weaning of the mice (see Fig.3.1.A.), a 12-week continuous induction schedule that starts at conception (via dox supplementation to the pregnant mice; see Fig.3.9.A.) and a 12-week induction schedule that starts at conception followed by a 12-week wash-out period defined by introduction of plain water (see Fig.3.9.B.). Under these schedules, bigenic PrP.11xCGG and PrP.90xCGG mice were supplemented with either 5% sucrose solution (dox-controls) or with a solution containing 5% sucrose and 4 mg/ml doxycycline hyclate.

For experiments involving trehalose treatment two different dox-induction schedules were used together with two trehalose supplementation timelines: A 12-week continuous dox and trehalose co-supplementation that starts at weaning (see Fig.3.14.A.) and a 12-week dox-induction that starts at weaning followed by a wash-out period defined by supplementation of trehalose (see Fig.3.21.A.). Under these schedules, bigenic PrP.90xCGG and BL6 mice (see

Fig.3.26.A.) were supplemented with normal food pellets (dox-controls), food pellets containing dox (ssniff), plain water (trehalose-controls) or a 2% trehalose solution.

The mice that were subjected to the antisense oligonucleotide (ASO) infusion experiments were supplemented with dox under a single 12-week induction schedule starting at weaning (see Fig.3.29.A). The ASO infusion was started after 4 weeks of dox-induction. In the following 4 weeks, mice received both dox and ASO-CCG followed by 4 additional weeks of only dox. Under this schedule, bigenic PrP.90xCGG were supplemented with food pellets containing dox (ssniff) and infused with either a 0.9% saline solution (ASO-controls) or a 0.9% saline solution containing 5,88 μg/μl ASO-CCG.

During the behavior testing of the mice subjected to trehalose and ASO treatments, mice did not receive doxycycline, trehalose or ASO-CCG in order to exclude any acute effects of these substances on behavior. On the other hand, during the phenotyping experiments mice continued to receive doxycycline to ensure compliance with the previously published phenotyping studies (Castro et al. 2017).

2.2.1.3 Stereotactic surgery and antisense oligonucleotide infusion

At weaning PrP.90xCGG mice were randomly allocated to one of the two treatment groups (saline versus ASO-CCG) with animals from the same litter being represented in both treatment groups and started to receive dox under the 12-week dox-induction schedule. 8-week old mice were anesthetized in an isoflurane anesthesia system (Rothacher) with 5% isoflurane in O_2/N_2O mixture and placed on a stereotactic frame (World Precision Instruments). Anesthesia was maintained throughout the surgery at 1.5%-2.0%. A 28G, brain infusion cannula (Plastics1) with 2.5 mm cut length that is attached via a catheter to a primed osmotic pump (Alzet model: 1004; Durect) filled with 100 µl of ASO-CCG solution (5.88 µg/µl in 0,9% NaCl) was inserted at coordinates M/L: -0.11 (directed laterally to the right), A/P: -0.05 relative to bregma resulting in an intracerebroventricular infusion at the right lateral ventricle. The cannula was secured to its location with Paladur® dental cement (Kulzer). Pumps were subcutaneously implanted on the back of the mice posterior to the scapulae. Osmotic pumps were removed under anesthesia at the end of the 4-week infusion schedule. Control animals were infused with 0.9% saline solution. Cannula placement was visually validated for each animal during cryosectioning (see Fig.3.29.B.).

2.2.2 Genotyping

Genotyping of the transgenic mice were performed from tail biopsies via PCR. Each biopsy tissue was digested by overnight incubation at 55°C in 125 µl PCR Direct Lysis Buffer and 3.75 µl Proteinase K from a stock solution of 10 mg/ml. After successful digestion, Proteinase K was heat inactivated at 85°C for 45 minutes. Digested samples containing DNA were kept in -20°C until further processing. Genotyping via PCR method was done with two set of primers designed to target rtTA transgene and TRE transgene. A separate set of primers that target the CGG-repeat stretches were used in order to track potential repeat expansions concerning the CGG-tract (see Table 2.1 through 2.3). The PCR products were visualized under ultraviolet light after being run in agarose gels made with 1xTAE buffer and the DNA marker EtBr.

Table 1: PCR protocol for the rtTA transgene

rtTA	PCR Master Mix	6,025 µl ddH_2O 1 µl 10x DreamTaq buffer (Thermo-Fischer) 0,8 µl dNTPs (2.5 mM) 0,125 µl spermidine (40mM) 0,5 µl Primer rtTA62f: 5’CAGCAGGCAGCATATCAAGGT3’ 0,5 µl Primer rtTA62r: 5’GCCGTGGGCCACTTTACAC3’ 0,05 µl DreamTaq-polymerase (Thermo-Fischer) <u>For each reaction tube:</u> 9 µl Master mix 1 µl DNA sample
	PCR	95°C 5 min **95°C 10 s** **62°C 20 s** **30 cycles** **72°C 45 s** 72°C 5 min 4°C storage
	Agarose gel	2%, 7 µl/100 ml EtBr
	PCR product	301 bp

Table 2: PCR protocol for the TRE transgene

TRE	PCR Master Mix	6,15 µl ddH$_2$O 1 µl 10x DreamTaq buffer (Thermo-Fischer) 0,8 µl dNTPs (2.5 mM) 0,5 µl Primer Tet-O-F4: 5’GCTTAGATCTCTCGAGTTTAC3’ 0,5 µl Primer Tet-O-R2: 5’ATGGAGGTCAAAACAGCGTG3’ 0,05 µl DreamTaq-polymerase (Thermo-Fischer) <u>For each reaction tube:</u> 9.0 µl Master mix 1.0 µl DNA sample
	PCR	95°C 5 min **95°C 30 s** **55°C 30 s 35 cycles** **72°C 90 s** 72°C 5 min 4°C storage
	Agarose gel	1,5%, 7 µl/100 ml EtBr
	PCR product	422 bp

Table 3: PCR protocol for the CGG repeat size

CGG - size	PCR Master Mix	6,75 µl ddH$_2$O 2,5 µl 10x Enhance High Fidelity buffer (Roche) 0,25 µl dNTPs (25 mM) 12,5 µl betaine (5M) 0,5 µl DMSO 0,5 µl Primer 11CGG3f: 5’CGGGTCGAGTAGGCGTGTAC3’ 0,5 µl Primer Tet-O-CGG-R: 5’CCAGTGCCTCACGACCAAC3’ 0,5 µl Enhance High Fidelity-polymerase (Roche) <u>For each reaction tube:</u> 9.0 µl Master mix 1.0 µl DNA sample
	PCR	95°C 10 min **95°C 60 s** **60°C 60 s 35 cycles** **72°C 5 min** 72°C 10 min 4°C storage
	Agarose gel	2%, 7 µl/100 ml EtBr
	PCR products	11CGG: 393 bp 90CGG: 657 bp

2.2.3 Tissue processing

Mice were anesthetized in an isoflurane chamber, sacrificed by decapitation and then brains were immediately removed. Right hemispheres were drop fixed overnight at 4 °C in 4% PFA/PBS. For fluorescent immunohistochemistry involving visualization of intranuclear inclusions (FMRpolyG and P62), fixed brain tissue was cryoprotected in 30% sucrose/PBS containing 0.02% sodium azide. Brain samples were then embedded in Tissue-Tek® O.C.T.™ compound (Sakura) and frozen in liquid nitrogen cooled isopentane. Frozen blocks were cut in 7 µm thick sagittal sections in a freezing microtome (Leica). Sections were mounted on poly-L-lysine coated slides, air-dried at room temperature, and stored at 4°C until further processing. For ubiquitin immunohistochemistry, drop fixed brain tissue was transferred and kept in a 2% PFA/PBS solution until they are embedded in paraffin blocks. Paraffin blocks were cut in 6 µm thick sagittal sections at room temperature. Sections were mounted on Superfrost™ (Menzel-Roth) slides, deparaffinized and kept at -80°C until further processing. For western blotting, cerebellum tissue was dissected out from the left hemispheres in cold (4-8°C) artificial cerebrospinal fluid (aCSF) containing (in mM) 129 NaCl, 21 $NaHCO_3$, 3 KCl, 1.6 $CaCl_2$, 1.8 $MgSO_4$, 1.25 NaH_2PO_4 and 10 glucose and immediately snap frozen in liquid nitrogen. The frozen samples were kept at -80°C until further processing. For slice electrophysiology experiments whole brain tissue for lateral amygdala (LA) and left-brain hemispheres for dentate gyrus (DG) were placed in cold (4-8°C) carbogenated (5% CO_2/95% O_2) aCSF. For DG physiology, hippocampal transverse slices (400 µm) were obtained from the septal pole by cutting parasagittal slices at an angle of about 12° using an angled platform. For LA slice physiology, horizontal brain slices (400 µm) including ventral hippocampus were cut at an angle of about 12° in the fronto-occipital direction. Three to four slices per hemisphere were transferred into an interface chamber perfused with aCSF (at 32.0 ± 1.0°C for LA; at 30.0 ± 1.0°C for DG; flow rate: 2.0 ± 0.2 ml/min, pH 7.4, osmolarity ~300 mosmol/kg). Slices were incubated for at least 1 hour before starting recordings.

For DAT, Th and GFP fluorescent immunohistochemistry, mice were anesthetized with a ketamine (80 mg/ml)/xylazine (6 mg/ml) mixture at ~1 mg/kg body weight and were transcardially perfused with first PBS then with 4% PFA/PBS. Brains were removed, kept in 4% PFA/PBS for 24 hours at 4°C then transferred into 30% sucrose/PBS containing 0.02% sodium azide for cryoprotection. Brain samples were then embedded in Tissue-Tek® O.C.T.™ compound (Sakura) and frozen in liquid nitrogen cooled isopentane. Frozen blocks were cut in 30 µm thick coronal sections in a freezing microtome (Leica). Brain sections were kept free floating at 4°C in PBS containing 0.02% sodium azide until further processing.

2.2.4 Electrophysiology

(Experiments performed by Dr. Gürsel Çalışkan; O. Stork's group, OvGU Magdeburg, Germany)

Field potential recordings: Glass electrodes filled with aCSF (~1 MΩ) were used for extracellular field recordings. For DG electrophysiology, the recording electrode was placed at the mid-molecular layer at a depth of 70-100 µm. Medial perforant pathway (MPP) was stimulated using a bipolar tungsten wire electrode with exposed tips of ~20 µm and tip separations of ~75 µm (electrode resistance in aCSF: ~0.1 MΩ) placed in the middle one third of the molecular layer. The positioning was confirmed by the paired-pulse depression at 50 ms interpulse interval. For LA electrophysiology, the recording electrode was placed in the LA and the stimulation electrode was placed at the external capsule (EC) for stimulation of cortical input to LA. Signals were pre-amplified using a custom-made amplifier and low pass filtered at 3 kHz. Signals were sampled at a frequency of 10 kHz.

Stimulation protocols: At least twenty minutes of baseline responses were recorded (0.033 Hz, pulse duration: 100 µs) to make sure that the responses were stabilized before measurement of baseline transmission. For MPP-DG recordings, an input-output (I/O) curve was obtained using five intensities ranging from 10 µA to 50 µA and for EC-LA recordings an I/O curve was obtained using nine intensities ranging from 10 µA to 200 µA. The stimulus intensity was arranged to elicit ~40-50% of the maximum amplitude and was further used for long-term potentiation (LTP) experiments. For LTP induction in the MPP-DG synapse, slices were perfused with 100 µM picrotoxin (PTX) to block GABAA receptor-mediated transmission. After baseline recordings of 10 minutes (0.033 Hz), LTP at the MPP-DG synapse was induced by delivery of a high frequency stimuli (HFS) train (100 Hz, 0.5 s duration, 50 stimuli). LTP at the EC-LA synapse was induced by two HFS (100 Hz, 20 s interval, 1 s duration, 100 stimuli per HFS) without PTX perfusion. After LTP induction, responses were recorded for a duration of 40 minutes (0.033 Hz). Data analyzed offline using self-written MATLAB-based analysis tools (MathWorks, Natick, MA)

2.2.5 Immunohistochemistry

Fluorescent IHC: Sections were treated with 0.01M sodium citrate (pH=6.0) in a microwave oven (if slide mounted) or in a hot air oven at 95°C (if free floating) for antigen retrieval. An extra antigen retrieval step with proteinase K (5 µg/ml) was included for inclusion stainings. Sections were first blocked for endogenous biotin using avidin/biotin blocking kit (Vector) and then blocked for mouse Ig when using mouse primary antibodies via M.O.M. reagents (Vector). Blocking was carried out with serum when using primary antibodies made in species other than mouse. Sections were incubated overnight at 4°C in primary antibodies. Following biotinylated secondary antibody incubation (Vector), antigen-antibody complexes were visualized by incubation in Cy-tagged streptavidin (Invitrogen). Double-stainings were performed sequentially for each primary antibody. Sections were counterstained with DAPI and coverslipped with Immu-Mount™ (Shandon).

Chromogenic IHC (Experiment performed by Lies-Anne Severijnen; R. Hukema's group, Erasmus MC, Rotterdam, The Netherlands): Sections were treated with 0.01M sodium citrate (pH=6.0) in a microwave oven for antigen retrieval. Endogenous peroxidase was blocked in PBS containing H_2O_2 (0,6%) and sodium azide (0,125%). An extra antigen retrieval step with proteinase K (5 µg/ml) was included. Sections were then blocked using a general protein blocker (PBS containing 0,5% protifar (Nutricia) and 0,15% glycine (Sigma)) and incubated overnight at 4°C in primary antibody. Following peroxidase conjugated secondary antibody incubation (Immunologic), antigen-antibody complexes were visualized by incubation in DAB substrate (Dako). Sections were counterstained with hematoxylin and coverslipped with entellan.

2.2.6 Image Analysis

For intranuclear inclusion quantifications, fluorescent photomicrographs of cerebellum lobule X with a z-step size of 2 µm were registered under an epifluorescence microscope (Leica) at 630x magnification and analyzed with open source image processing software Fiji. 400 DAPI+ nuclei that lie within the granular layer of the lobule X were counted per mice by a researcher who was blind to the treatment groups. For this quantification random images of 30 µm by 30 µm were used that were generated from whole photomicrographs of lobule X by a custom cell counter script developed for Fiji software (script written by Y. E. Demiray; O. Stork's group, OvGU Magdeburg, Germany). For each DAPI+ nucleus that were counted the script recorded through the researcher's input whether or not the nucleus contains a FMRpolyG+ intranuclear inclusion and its longitudinal size. From the data of the identified inclusions a percentage and an average size value were calculated for each mouse. Statistics have been performed from these values. The same custom script was used for total DAPI+ and Th+ cell counts from the fluorescent photomicrographs of substantia nigra taken at 400x magnification. This time, all DAPI+ nuclei and Th+ cells that were contained in the random images were counted. For signal intensity quantifications from 100x photomicrographs of striatum and substantia nigra, Fiji's built in raw intensity and area measurement functions were used. The inclusion quantifications from ubiquitin staining were performed as previously described (see Hukema et al. 2015) by Lies-Anne Severijnen; R. Hukema's group, Erasmus MC, Rotterdam, The Netherlands.

2.2.7 Western blot

Cerebellum tissue was lysed on ice with the help of a dounce homogenizer (Wheaton) in laurylmaltoside lysis buffer (1% lauryl maltoside N-dodycyl-D-maltoside, 1% NP-40, 1 mM Na_3VO_4, 2mM EDTA, 50 mM Tris-HCl, 150 mM NaCl, 0.5% DOC, 1 mM AEBSF, 1 µM pepstain A, 1 mM NaF, 1 tablet Pierce protease inhibitor (Thermo Fisher)). Homogenized samples were agitated on a rotator turning at 40 rpm at 4°C for 30 min. Samples were then centrifuged for 30 min at 4°C at 16000 rcf. Protein concentration of each sample was determined using the Bradford assay (Bio-Rad) according to the manufacturer's instructions. Protein samples were separated by SDS-PAGE (15%) and transferred to PVDF membranes (Immobilon-FL, Millipore). Membranes were incubated with primary antibodies and antigen-antibody complexes were visualized via fluorescent secondary antibody incubation. Florescent blotted membranes were scanned with the Odyssey scanner (LI-COR) and the signal associated with the antigen/antibody complexes were analyzed using Odyssey ImageStudio software (LI-COR).

2.2.8 Behavioral experiments

When multiple experiments were conducted with the same mice, they were performed in a sequence from the least stressful to the most, in order to minimize potential interferences between tests. Anxiety tests were thus, performed at the beginning of a behavior battery and the fear conditioning was set as the last test. When more than one anxiety test was performed with the same group of mice, these tests were distributed throughout the behavior battery. Nevertheless, no anxiety test was performed following the fear conditioning paradigm. At least 24 hours elapsed between individual sessions and tests of a battery.

2.2.8.1 Rotarod

Motor performance of mice was assessed using the Rotarod test. Two versions of this test were performed with varying training sessions. The training session of the test was performed by placing the mice on the rotating rod at 15 rpm constant speed for a maximum of 60 s in four trials. The training session was only one day for the assessment of motor performance related to treatment strategies and it was repeated for 3 days in the phenotyping experiments. The 3-day version was performed by Dr. Mónica Santos; CNC, University of Coimbra, Portugal. Following the training session, mice were tested on the rotating rod for different constant speeds (8, 15, 24, 31, 36, 40 rpm) in two trials each for a maximum of 60 seconds. Last day of the Rotarod test consisted of testing the mice during a 5 min accelerated ramp from 4 to 40 rpm in four trials. In each trial, the latency to fall off the rod was registered (Castro et al. 2017). The apparatus was cleaned with 10% ethanol.

2.2.8.2 Acoustic startle reflex and prepulse inhibition

In order to asses sensorimotor gating, mice were placed in a mouse holder fixed on a motion sensor and housed within a padded soundproof chamber. Startle responses were registered using acoustic startle reflex equipment and analyzed using SOF-825 software (Med Associates). Both ASR and PPI measurements were performed on the same experimental day and the protocol lasted approximately 35 min. Throughout the experiment, randomized inter-trial intervals (10-30 seconds) were used and constant white noise of 62 dB was played.

The experiment consisted of 5 min of acclimation period followed by 50 ASR trials, where white noise pulses of 20 ms (1 ms rise) with five different sound pressure levels (0, 80, 90, 100 and 110 dB) were presented in a pseudo-randomized order. Ten measurements were taken for each pulse level and startle responses were recorded for 500 ms. The PPI trials consisted of 4 ms pre-pulses (white noise, 1 ms rise) of 0, 70, 75, 80 and 85 dB that preceded 20 ms pulses (white noise, 1 ms rise) of 110 dB in a pseudo-randomized order. The inter-stimulus interval was kept constant at 100 ms for all PPI trials. Ten measurements were taken for each pre-pulse level and data acquisition was made for 450 ms after the 110 dB pulse presentation.

Table 4: ASR and PPI experimental layout
The letters represent the sound pressure level presented during each of the individual 50 trials. For the ASR session: A: 0 dB, B: 80 dB, C: 90 dB, D: 100 dB, E: 110 dB. For the PPI session: A: 70 dB, B: 75 dB, C: 80 dB, D: 85 dB, E: 0 dB

1 D	2 D	3 E	4 D	5 B	6 B	7 B	8 D	9 B	10 C
11 A	12 E	13 C	14 C	15 A	16 D	17 B	18 E	19 C	20 A
21 A	22 C	23 C	24 B	25 D	26 A	27 E	28 E	29 D	30 C
31 B	32 A	33 E	34 C	35 B	36 B	37 E	38 A	39 D	40 A
41 E	42 B	43 E	44 E	45 C	46 D	47 D	48 C	49 A	50 A

Startle responses were quantified by the peak amplitudes reported by the SOF-825 software. The results from ASR trials were obtained by calculating mean amplitudes of 10 trials for each pulse level. The mean amplitudes were then normalized to 0dB measurements and reported as the relative startle amplitudes. The results from the PPI trials were reported as the average of the percentage of PPI values of ten trials per pre-pulse level. The percentage of PPI was calculated as follows: [(response to pulse alone – response to pre-pulse plus pulse) / response to pulse alone] x 100. The mouse holder was cleaned with soap water (adapted from Valsamis and Schmid 2011).

2.2.8.3 Pawprint patterns

Gait parameters were analyzed from pawprints collected by letting the mice walk in a straight line on a white sheet of paper placed under a methacrylate tunnel with their fore- and hind paws painted in different colors using non-toxic ink; blue and red respectively. Using the pawprint patterns 6 different gait parameters from 3 subsequent steps were measured and reported. This corresponds to 4 individual measurements averaged to define the uniformity of step alternation (m_1) parameter and 3 individual measurements averaged to be analyzed as forepaw width (m_2), hind paw width (m_3) and stride length (m_4). The overlap symmetry was calculated as the average difference between the fore- hind paws on one side subtracted from the same measure on the other side (m_5). Alternation coefficient was calculated as $0.5-(m_4/m_6)$ (adapted from Castro et al. 2017).

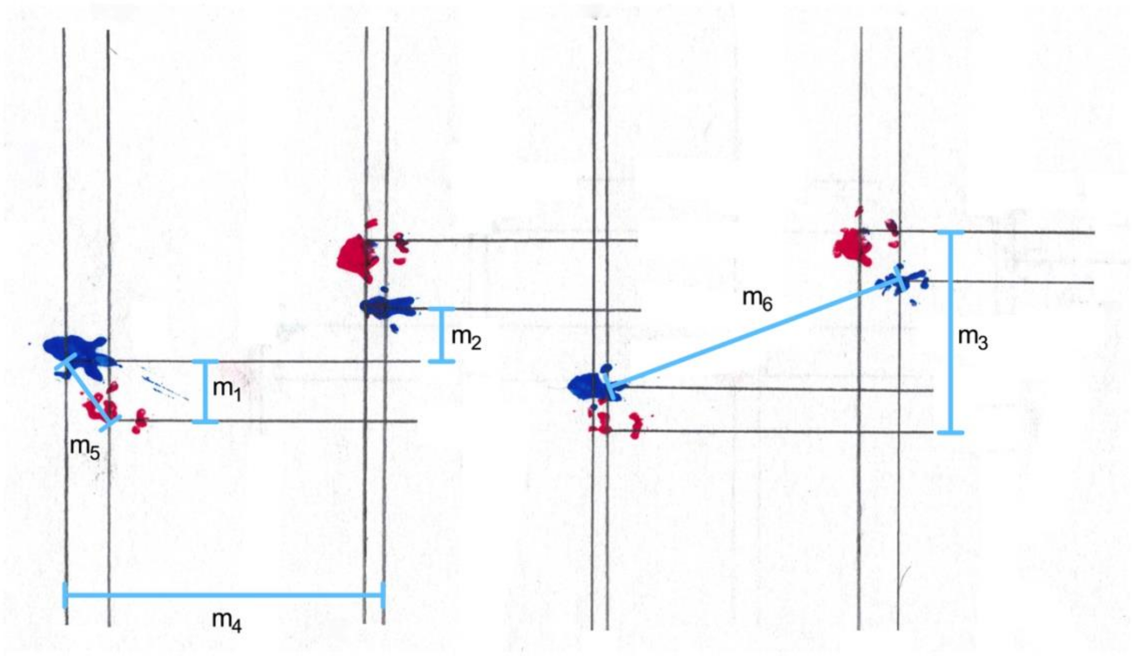

Figure 2.1: Representative pawprint pattern with quantified measures indicated

2.2.8.4 Open field

Locomotor activity and bradykinesia were assessed in a 50 cm by 50 cm open field apparatus under dim light conditions (35 Lux). In the arena, mice were able to freely move, and their movement was tracked and recorded by the AnyMaze software (Stoelting Co.). Total distance covered in the apparatus and time spent in the center (inner area of 25 cm by 25 cm) were the parameters analyzed in 5-minute bins using the software. The apparatus was cleaned with 10% ethanol (adapted from Castro et al. 2017).

2.2.8.5 Light/dark transition test

Mice were tested for anxiety-like behavior in a chamber equipped with a motion-detecting photobeam system and a light source (TSE). The chamber was separated into two compartments of 20 cm by 20 cm each with a methacrylate box. The compartments were connected to each other with a 4 cm by 4 cm opening. One of the compartments was kept dark (0 lux) and the other was illuminated (110 lux). The mice were placed in the illuminated compartment and tracked for 5 minutes. The time they spent in each compartment was recorded. The apparatus was cleaned with 10% ethanol (adapted from Castro et al. 2017).

2.2.8.6 Marble burying

Mice were placed in a mouse cage filled with fresh bedding containing 15 glass marbles. The marbles were placed on the bedding equidistant to each other. Mice were able to move freely in the cage and the number of marbles they have buried after 30 minutes was recorded. The test was performed under dim light conditions (35 Lux) (adapted from Angoa-Pérez et al. 2013).

2.2.8.7 Trace fear conditioning

The trace fear conditioning protocol consisted of four days and was performed in a chamber equipped with steel shock grid to replace the floor, a photobeam tracking system, a speaker, a ventilation fan and a light source. During day 1, mice were placed in a clear methacrylate box (20 cm by 20 cm) to confine them to the shock grid area and were habituated to the apparatus for 5 mins. The training session was performed the next day and consisted of a 2 min pre-training phase without any stimulus, five 10 s of conditioned stimuli (CS+: 2,4 kHz at 80 dB) followed by a presentation of a 2 s foot-shock (0.30 mA) that was separated from the CS+ by a 20 s pause. The inter stimulus interval was 2 minutes. The training ended with a post-training phase of 2 min without any stimulus. On day 3, the context retrieval was performed by placing the mice in the clear box with the grid floor for 5 minutes. The last day of the test was the cue retrieval session and it was performed by placing the mice in a mouse cage filled with fresh bedding that was covering the steel shock grid in the apparatus but not the photobeams. During this session mice were exposed to the same stimuli that were presented on day 2 with the exception of the foot-shock. Throughout the test, the movements of the mice in the apparatus were recorded and their freezing behavior that is complete immobility except breathing was reported. The apparatus was cleaned with 10% ethanol (adapted from Burman et al. 2014).

2.2.9 Statistics

All statistical analyses were performed by the author using the Prism software (GraphPad). For the experimental procedures, the sample sizes were set according to Cohen’s d=0.8. For group comparisons, data were first checked for normality using Shapiro-Wilk normality test. For normally distributed data, Student’s t-test or one-way ANOVA was performed. For data that does not pass the normality test, Mann-Whitney U-test or Kruskal-Wallis test was used. Two-way ANOVA was used when two factors were compared. If repeat measures were available for one of the factors, then the data were analyzed using repeated measures two-way ANOVA. For analyses involving three factors including the cases, where one of the factors is a repeated measures factor, data were reported using three-way ANOVA. For three-way ANOVA analyses, statistically significant factor interactions that result from hypothesis testing were reported in the results section, whereas interactions that were encountered during exploratory analyses were reported in the appendix. Also, interactions involving at least one repeated measures factor were reported in the appendix. When applicable, post-hoc comparisons were performed with Fisher's LSD test. Full range of pair-wise comparison tables has been made available in the appendix. For simplicity, the pair-wise comparison tables related to three-way ANOVA analyses report statistically significant data only. p-values smaller than 0.05 were considered statistically significant for all analyses. All data were presented as mean ± S.E.M.

3 Results

3.1 Exploration of unidentified phenotypes in the PrP.90xCGG model

In order to identify additional phenotypes of the premutation that have been described for human patients but have not yet been reported with the PrP.90xCGG model so far, two new induction schedules have been devised. These schedules aim to capture two very different time windows of the premutation: late and early (or pre-motor).

3.1.1 Extended induction timeline and phenotyping

RATIONALE - One of the behavioral deficits that has been reported with human patients with FXTAS but have not yet been identified with the PrP.90xCGG model is related to sensorimotor gating. Deficits in sensorimotor gating have been found to become more prominent as overall severity of FXTAS increases with patients (Schneider et al. 2012). Therefore, prepulse inhibition, a measure of sensorimotor gating has been investigated as a potential late-phenotype under the extended 24-week dox-induction schedule (Fig.3.1.A).

Prepulse inhibition (PPI) in an acoustic setting is a phenomenon, where a weak acoustic pulse that cannot produce a startle response by itself alone reduces the startle response produced by a stronger acoustic pulse when presented before that stronger pulse (Fig.3.1.B). When basal startle responses were measured presenting an acoustic pulse at sound pressure levels (SPL) of 80 dB, 90 dB, 100 dB and 110 dB, the startle responses of 24-week dox-induced mice with a 90xCGG tract did not differ from their uninduced counterparts (Fig.3.1.C; N(dox-)=11, N(dox+)= 13, 2-way RM ANOVA, dox-effect; F(1,22)=0.2033, P=0.6565). The increase in the basal startle responses with increasing SPL also excludes potential hearing deficiencies that may influence the results (2-way RM ANOVA, SPL-effect; F(1.195,26.30)=40.33, P<0.0001). Unlike the similarities in the basal startle responses, dox-induced mice showed reduced prepulse inhibition compared to controls under an experimental setting, where 70 dB, 75 dB, 80 dB and 85 dB acoustic pulses that preceded the 110 dB main pulse were presented (Fig.3.1.D; N(dox-)=11, N(dox+)=13, 2-way RM ANOVA, dox-effect; F(1,22)=4.992, P=0.0359).

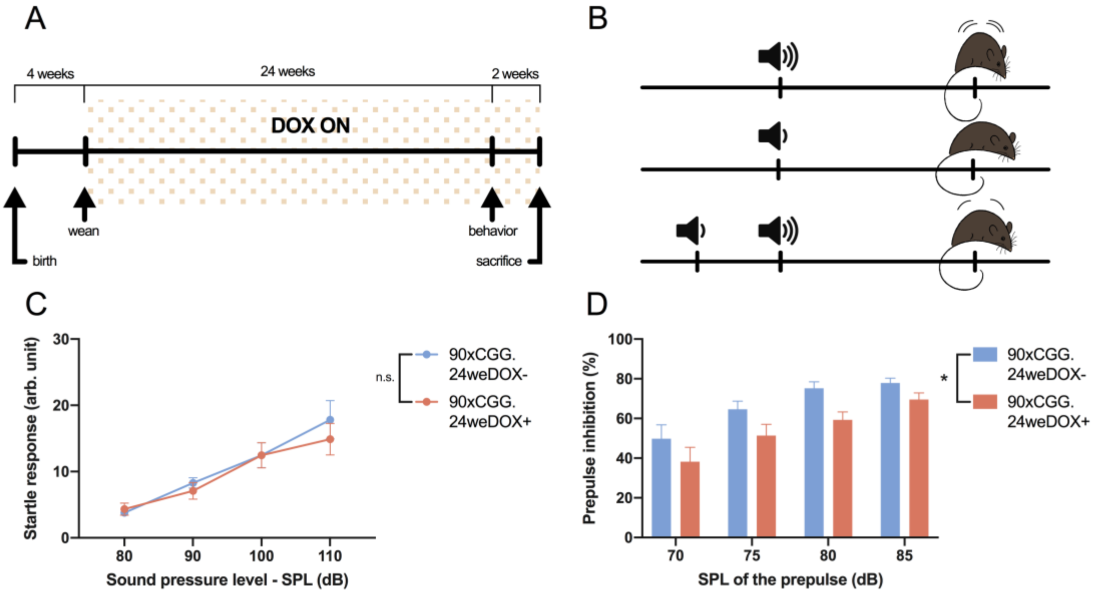

Figure 3.1: 24 weeks extended induction timeline and sensorimotor behavior of 90xCGG mice
A. *Timeline showing the 24 weeks-long dox induction schedule that is used to investigate later-occurring phenotypes related to the premutation.* ***B.*** *Graphical representation of the prepulse inhibition phenomenon: a weak acoustic pulse that cannot produce a startle response by itself alone reduces the startle response produced by a stronger pulse when presented before that pulse.* ***C.*** *Baseline startle responses recorded from 90xCGG.24we mice showed no significant differences in the responses produced by acoustic pulses of various sound pressure levels between the dox induced mice and the dox- controls.* ***D.*** *Reduced prepulse inhibition observed in dox+ mice as compared to their dox- counterparts. Data presented as mean ± S.E.M. *p<0.05. For details on ANOVA results see* ***Table S1****.*

In order to investigate the specificity of the PPI deficits seen with the 24 weeks dox-induced mice with the expanded 90xCGG repeats, two additional groups were subjected to the same experimental setting. First, inducible mice with 11xCGG repeats that correspond to a normal repeat length were tested for their basal startle responses and PPI levels (N(dox-)=7, N(dox+)=9). There were no differences between the basal startle response levels between 24 weeks dox-induced mice with 11xCGG repeat length and their dox- counterparts (Fig.3.2.A; 2-way RM ANOVA, dox-effect; F(1,14) = 0.5299, P=0.4786, SPL-effect, F(1.556,21.78)=29.76, P<0.0001). Also, no differences were observed in the PPI levels (Fig.3.2.B; 2-way RM ANOVA, dox-effect; F(1,14)=4.054, P=0.0637), reflecting the repeat length dependent manifestation of the PPI deficits. Second, inducible mice with 90xCGG repeats that were subjected to a shorter 12 weeks dox-induction were tested in the acoustic startle setup (N(dox-)=11, N(dox+)=11). There were no differences between the basal startle response levels between 12 weeks dox-induced mice with 90xCGG repeat length and their dox- counterparts (Fig.3.2.C; 2-way RM ANOVA, dox-effect; F(1,20)=0.001249, P=0.9722, SPL-effect; F(1.436,28.71)=29.71, P<0.0001). Again, no differences were observed also in the PPI levels (Fig.3.2.D; 2-way RM ANOVA, dox-effect; F(1,20)=0.2725, P=0.6074).

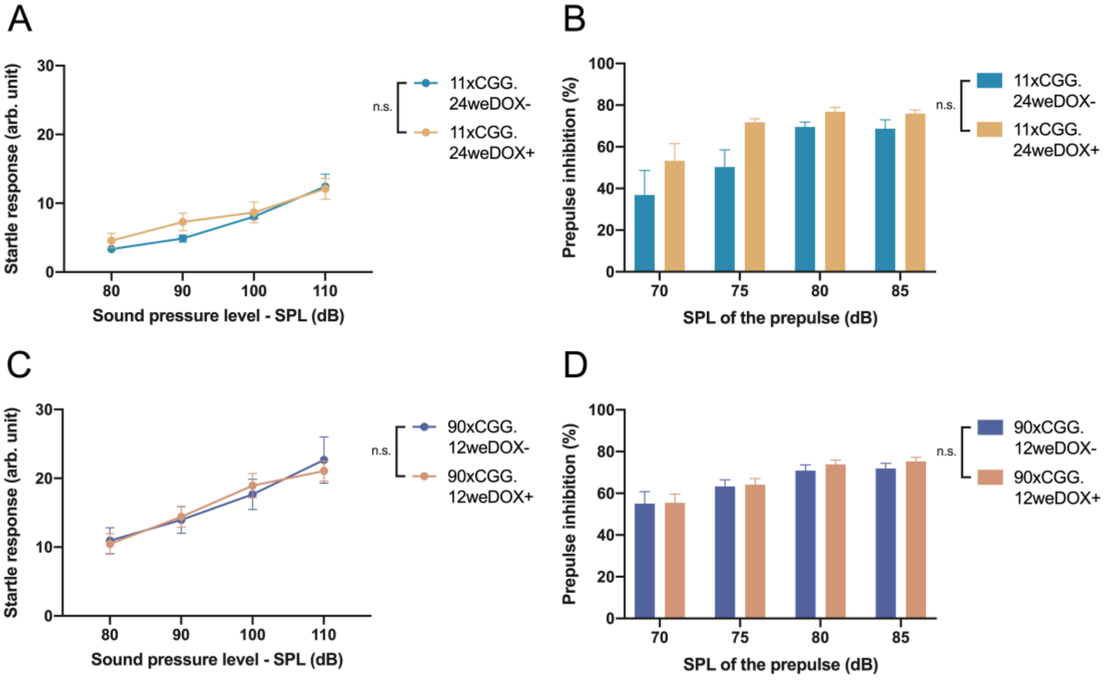

Figure 3.2: Sensorimotor behavior of the 11xCGG.24we and 90xCGG.12we control groups
A. *Baseline startle responses were comparable between dox-induced and uninduced 11xCGG.24we mice.* ***B.*** *Prepulse inhibition levels between dox+ and dox- mice from the 11xCGG.24we group showed no differences.* ***C.*** *Baseline startle responses of 90xCGG mice that were treated with dox for a shorter 12-week period and their dox- counterparts showed no differences.* ***D.*** *Prepulse inhibition levels remained comparable between 90xCGG mice that were induced with dox for 12 weeks and their dox- counterparts. Data presented as mean ± S.E.M. For details on ANOVA results see* ***Table S2****.*

Parkinsonian features are another type of phenotype that manifests with considerably high prevalence in FXTAS patients and this prevalence also increases with advancing clinical stage. Parkinsonism is classically associated with motor features such as abnormal posture, bradykinesia and decreased step length (Niu et al. 2014). However, these features have not yet been identified with the PrP.90xCGG model. Castro and colleagues have already shown gait abnormalities with the model after 12 weeks of dox-induction as well as following a 12-week recovery period also known as the wash-out period. Despite other gait abnormalities, no differences were observed in the stride length at these two time-points. Moreover, their locomotion measures were also unchanged (Castro et al. 2017). In order to investigate parkinsonian features of decreased stride length and bradykinesia, 24 weeks dox-induced groups with 90xCGG and 11xCGG repeat length were subjected to paw print analysis and open field test. Paw prints taken from 24 weeks dox-induced 90xCGG mice that were made to walk on blank sheet of paper with colored paws revealed that they cover a smaller distance with a given number of steps (Fig.3.3.A) with a significantly reduced stride length as compared to their dox- counterparts (Fig.3.3.B; N(dox-)=14, N(dox+)=16, Student's t-test, t=3.767, df=28, P= 0.0008). On the other hand, 24 week-long dox-induced mice with 11xCGG repeat length did not show any difference in their stride length as compared to their dox- counterparts (Fig.3.3.C; N(dox-)=9, N(dox+)=8, Student’s t-test, t=0.2230, df=15, P=0.8266). In order to assess bradykinesia, 24 weeks dox-induced mice were subjected to an open field test, in which the distance that they cover during a 20-minute exposure to the arena was recorded in 5 mins bins, together with the time they spent in the center of the arena to ensure the locomotion parameter is not affected by differences in the exploration of certain areas of the arena (N(dox-)=14, N(dox+)=16). No differences in the distance they covered (Fig.3.3.D; 2-way RM ANOVA, dox-effect; F(1,28)=0.7263, P=0.4013) or in the time they spent in the center of the open field arena (Fig.3.3.F; 2-way RM ANOVA, dox-effect; F(1,28)=2.201, P=0.1491) were observed when 24 weeks dox-induced 90xCGG mice were compared to their dox- counterparts. To control for the repeat-length 11xCGG.24we mice were also subjected to the same tests (N(dox-)=9, N(dox+)=9) and no differences were observed between dox+ and dox- groups (Fig3.3.E; distance covered: 2-way RM ANOVA, dox-effect; F(1,16)=0.1120, P=0.7423, time-bin x dox-effect; F(3,48)=3.020, P=0.0387, Fisher’s LSD; ns for all time-points and Fig3.3.G; time in the center: 2-way RM ANOVA, dox-effect; F(1,16)=4.158, P=0.0583. For details on the post-hoc analysis see Table S3.).

Decreased striatal dopamine transporter (DAT) density is a molecular phenotype related to nigrostriatal dysfunction reported with varied severity in some FXTAS patients (Madeo et al. 2013), (Scaglione et al. 2008) but not all (Ceravolo et al. 2005) and is used as an alternative diagnostic criterion Parkinson’s Disease (PD) (reviewed in Kägi, Bhatia, and Tolosa 2010). Moreover, decreased DAT density in the striatum has been associated with PPI deficits in PD patients (Zoetmulder et al. 2014) as well as in various DAT-deficient and knock-out mouse models (Vuillermot, Feldon, and Meyer 2011), (Ralph et al. 2001). In relation to the PPI deficits identified with the 24 weeks dox-induced 90xCGG mice, a DAT expression analysis based on immunohistochemistry was performed and quantified for fluorescence intensity from coronal brain sections containing striatum. (Fig.3.4.A). Significantly lower signal intensity density specific to DAT in the striatum was observed with dox-induced mice as compared to dox- control mice (Fig3.4.B; N(dox-)=4, N(dox+)=4, Mann-Whitney U-test, U=0, P=0.0286).

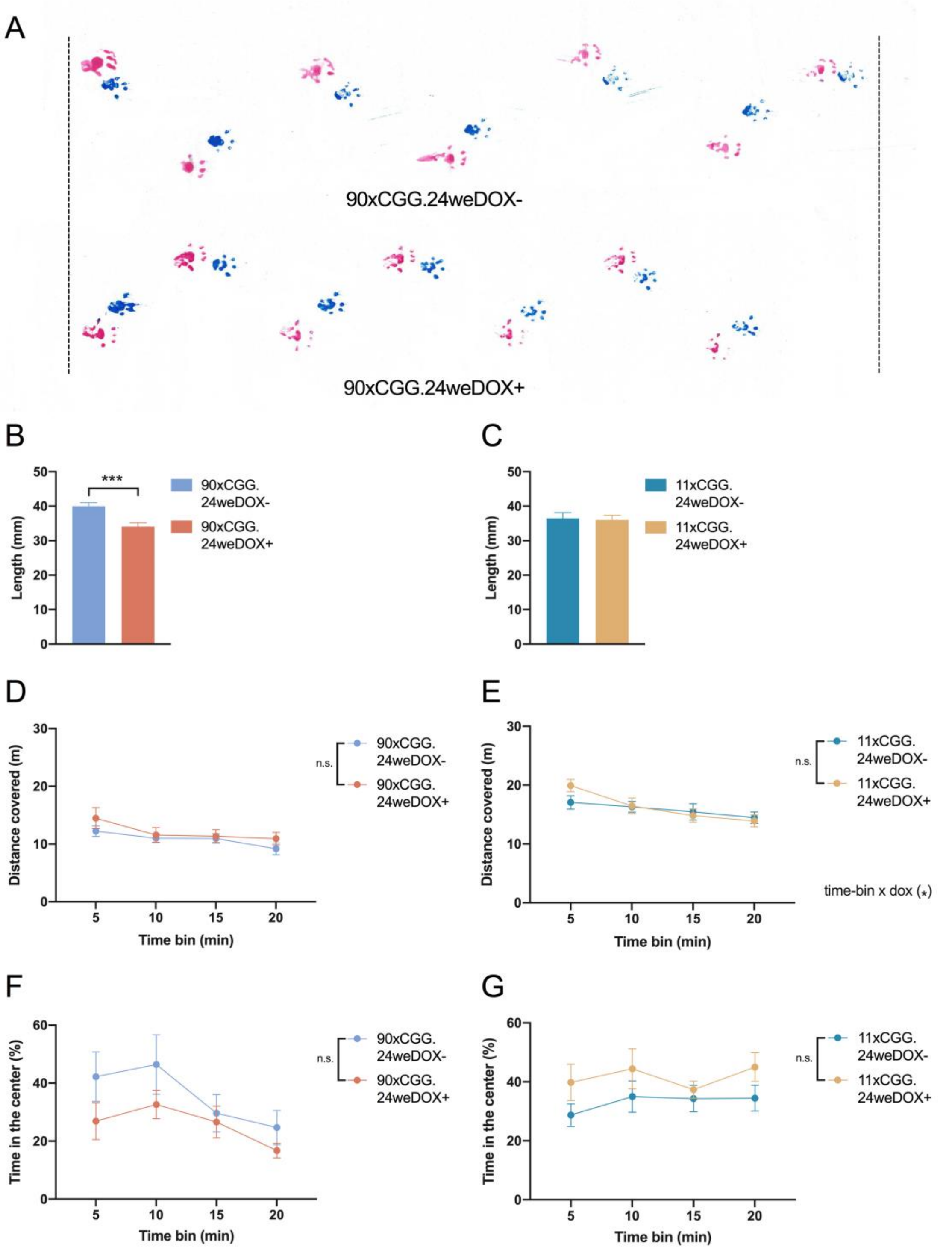

Figure 3.3: Gait and locomotor activity of 11xCGG and 90xCGG groups under the 24 week-long induction schedule

A. *Visual representation of paw prints that were used to quantify stride length. Notice that the dox-induced 90xCGG.24we mouse covers a shorter distance as compared to dox- control with the same number of steps.* ***B.*** *Stride length of dox-induced 90xCGG.24we mice was significantly reduced as compared to their dox- counterparts.* ***C.*** *No differences were observed between the stride length of dox-treated 11xCGG.24we mice and their dox- controls.* ***D.*** *No differences in the distance covered in the open field arena were observed between dox-induced 90xCGG.24we mice and their uninduced counterparts.* ***E.*** *The distance covered measure was also unchanged between dox-induced 11CGG.24we mice and their dox- counterparts.* ***F.*** *In the open field arena, no differences were observed in the time spent in the center between the dox-induced 90xCGG.24we mice and the dox-*

*control mice. **G.** No differences were observed in the time spent in the center of the open field arena between dox+ and dox- mice within the 11xCGG.24we group. Data presented as mean ± S.E.M. ***p<0.001. For details on ANOVA results see **Table S3**.*

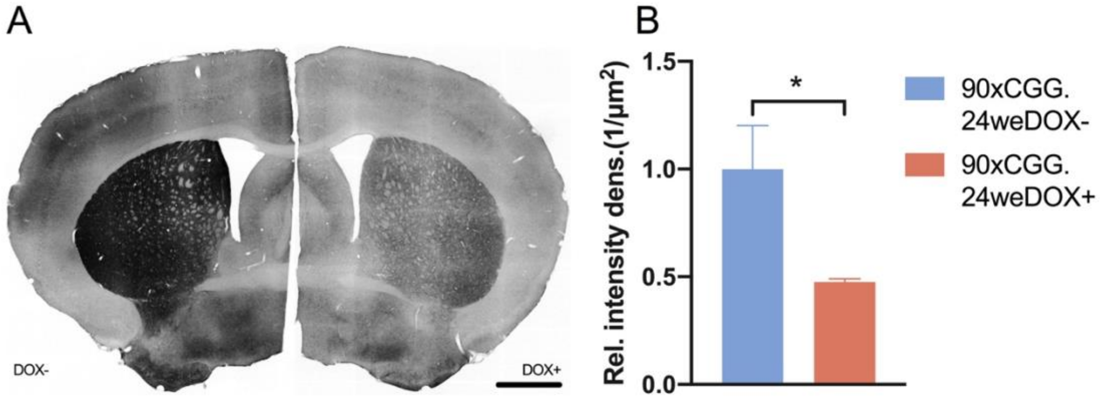

Figure 3.4: Dopamine transporter expression of the 90xCGG.24we mice in the striatum
***A.** Representative photomicrograph of the fluorescent immunohistochemical staining against dopamine transporter (DAT). Left: dox- control slice, right: slice from a dox-induced mouse. Darker shades indicate higher signal specific to DAT. Scale bar indicates 500 μm. **B.** Signal intensity density related DAT was significantly reduced in the striatum of dox-induced 90xCGG.24we mice as compared to the dox- control mice. Data presented as mean ± S.E.M. *p<0.05.*

Given the lower intensity density identified with the 24 weeks dox-induced 90xCGG mice, the next step was to check for abnormalities in the dopaminergic neurons in relation to nigrostriatal dysfunction, as DAT in the striatum is presynaptic and originates from tyrosine hydroxylase (Th)-positive neurons of the substantia nigra pars compacta (SNpc). To this end, coronal brain sections containing SNpc were stained for Th and quantified for the intensity density specific to Th (Fig.3.5.A). The signal intensity density of Th was found to be significantly reduced in 24 weeks dox-induced 90xCGG mice as compared to their dox- counterparts (Fig.3.5.B; N(dox-)=4, N(dox+)=4, Student's t-test, t=4.667, df=6, P= 0.0034).

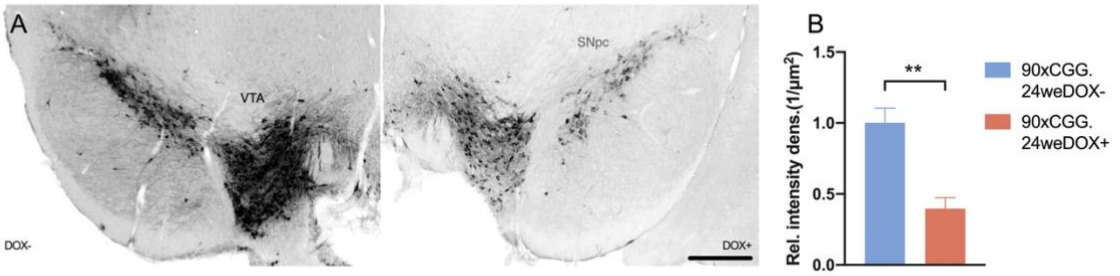

Figure 3.5: Tyrosine hydroxylase expression of the 90xCGG.24we mice in the substantia nigra pars compacta
***A.** Representative photomicrograph of the fluorescent immunohistochemical staining against tyrosine hydroxylase (Th). Left: dox- control slice, right: slice from a dox-induced mouse. Darker shades indicate higher signal specific to Th. Scale bar indicates 500 μm. **B.** Signal intensity density related to Th was significantly reduced in the substantia nigra pars compacta (SNpc) of dox-treated*

*90xCGG.24we mice as compared to the dox- counterparts. Data presented as mean ± S.E.M. **p<0.01.*

Lower Th intensity density represents a potential dysfunction with these neurons, however this result does not address whether there is a loss of Th+ neurons due to a neurodegenerative process. Therefore, SNpc sections stained against Th were quantified for the number of Th+ (yellow) cells and number of nuclei (blue) per area contained within the SNpc from fluorescent photomicrographs (Fig.3.6.A). Significantly lower number of Th+ neurons (Fig.3.6.B; Student's t-test, t=3.904, df=6, P= 0.0080) as well as DAPI+ nuclei (Fig.3.6.C; Student's t-test, t=2.687, df=6, P=0.0362) were encountered in the SNpc region of the 24 weeks dox-induced 90xCGG mice as compared to the dox- controls (N(dox-)=4, N(dox+)=4).

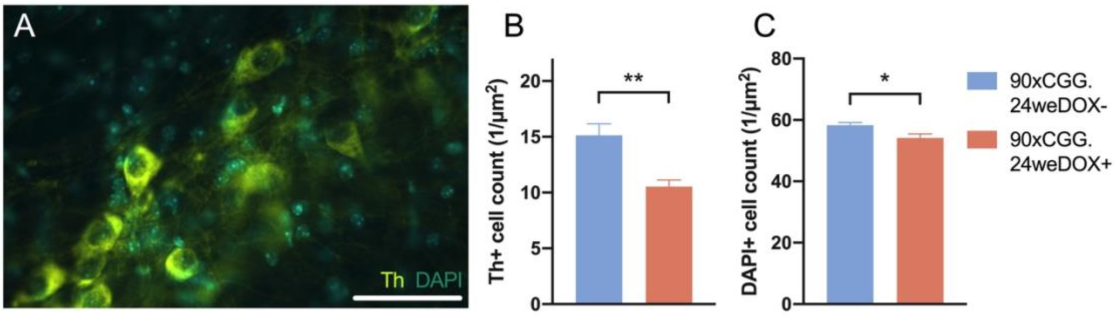

Figure 3.6: Cell counts in the substantia nigra pars compacta of the 90xCGG.24we mice
***A.** Representative photomicrograph of the fluorescent immunohistochemical staining against Th (yellow) and DAPI staining (blue) used for cell number quantifications. Partial caption obtained from SNpc. Scale bar indicates 50 µm. **B.** Number of cells that stain positively for Th was significantly reduced in the SNpc of dox-induced 90xCGG.24we mice as compared to dox- control mice. **C.** Number of nuclei within the same region of dox-treated 90xCGG.24we mice was also significantly reduced as compared to dox- controls. Data presented as mean ± S.E.M. *p<0.05, **p<0.01.*

Next, the intranuclear inclusion pathology of FXTAS was investigated within the context of Th+ neurons of SNpc. Coronal brain sections of 24 weeks dox-induced 90xCGG mice containing SNpc as well as parts of hippocampus that has already been demonstrated to form inclusions (Castro et al. 2017) were stained for Th (yellow) and FMRpolyG (red) (Fig.3.7.A). No FMRpolyG focus was encountered within the Th+ neurons of the SNpc (Fig.3.7.B), whereas positive FMRpolyG labeling of the nuclei (blue) within the pyramidal layer of cornu ammonis-3 (CA3) region of the hippocampus was observed (Fig.3.7.C).

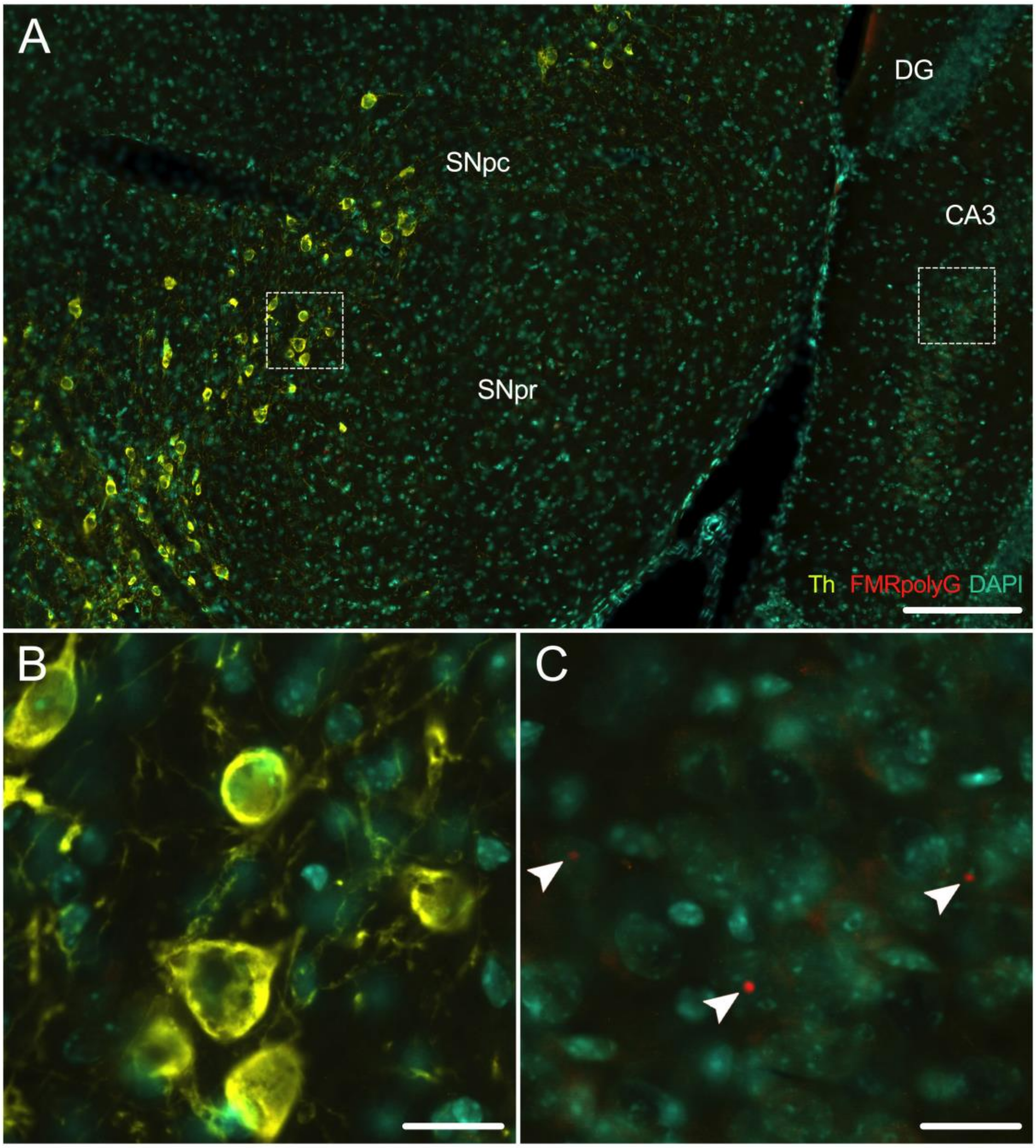

Figure 3.7: Tyrosine hydroxylase-positive cells of 90xCGG.24we mice do not form intranuclear inclusion bodies despite dox-induction

A. *Photomicrograph of the fluorescent immunohistochemical staining against Th (yellow) and FMRpolyG (red) in a broder region that encapsulates substantia nigra and parts of ventral hippocampus. DAPI: Blue. Scale bar indicates 200μm.* ***B.*** *Closeup caption from A(left) showing the lack of colocalization of FMRpolyG signal with Th signal. Scale bar indicates 20μm.* ***C.*** *Closeup caption from A(right) showing the intranuclear inclusions in the cornu ammonis-3 (CA3) region of the ventral hippocampus that stain positively for FMRpolyG on the same section. White arrowheads: FMRpolyG foci. Scale bar indicates 20 μm.*

Despite the lack of inclusion pathology, Th+ neurons in the SNpc of the 24 weeks dox-induced 90xCGG animals expressed the TRE-90xCGG-eGPF transgene under the prion-protein driver upon dox exposure. Double staining against Th and GFP in the SNpc of these mice (Fig.3.8.A) revealed complete colocalization of Th signal (red) with GFP signal (green)

(Fig.3.8.A-B-C). Also, a small number of GFP+ cells that do not stain positively for Th were encountered in the SNpc (Arrowhead in Fig.3.8.A-B-C).

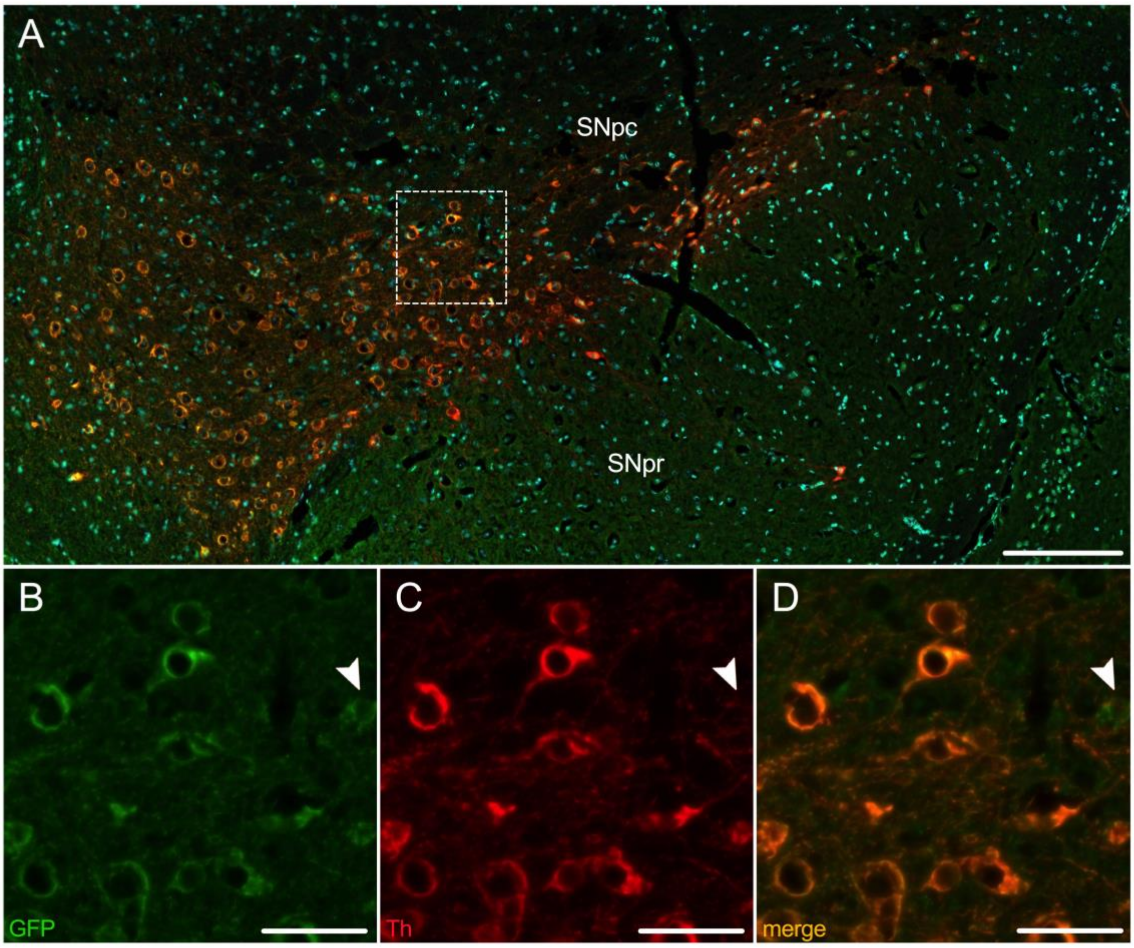

Figure 3.8: Tyrosine hydroxylase-positive cells express the 90xCGG transgene upon 24 weeks of dox administration

__A.__ Photomicrograph of the fluorescent immunohistochemical staining against Th (red) and GFP (green) in the SNpc of dox-induced 90xCGG mice. Blue: DAPI. Scale bar indicates 200 μm. Caption is represented as closeups in __B__. indicating GPF+ cells, in __C.__ indicating Th+ cells and in __D.__ indicating colocalization of the Th and the GFP signal. Arrowheads show a GFP+ cell that stains negatively for Th. Scale bars indicate 20μm.

3.1.2 Early induction timeline and phenotyping

RATIONALE - The early induction timeline has been designed to capture the pre-motor symptoms of the premutation. This timeline avoids the use of shorter than 12 weeks induction schedules that do not result in behavioral phenotypes but allows for testing the mice at a younger age by initiating the induction from conception onwards (Fig.3.9.A). In an effort to investigate rescue possibilities for the potential phenotypes encountered under this early induction timeline, an additional schedule with a 12-week long wash-out (WO) period following the 12 weeks of dox-induction has also been introduced (Fig.3.9.B).

First, the mice have been tested for motor deficits on a rotarod setup following the 12 weeks dox-induction (N(dox-)=11, N(dox+)=10). The dox+ and dox- groups did not differ from each other in their latency to fall off the rod either of the training session (Fig.3.9.A; 2-way RM ANOVA, dox-effect, F(1,19)=3.329, P=0.0838) or the constant speed test session (Fig.3.9.D; 2-way RM ANOVA, dox-effect, F(1,19)=0.1859, P=0.6712) or the accelerating rod test session (Fig.3.9.E; Mann-Whitney test, U= 34.50, P= 0.1510).

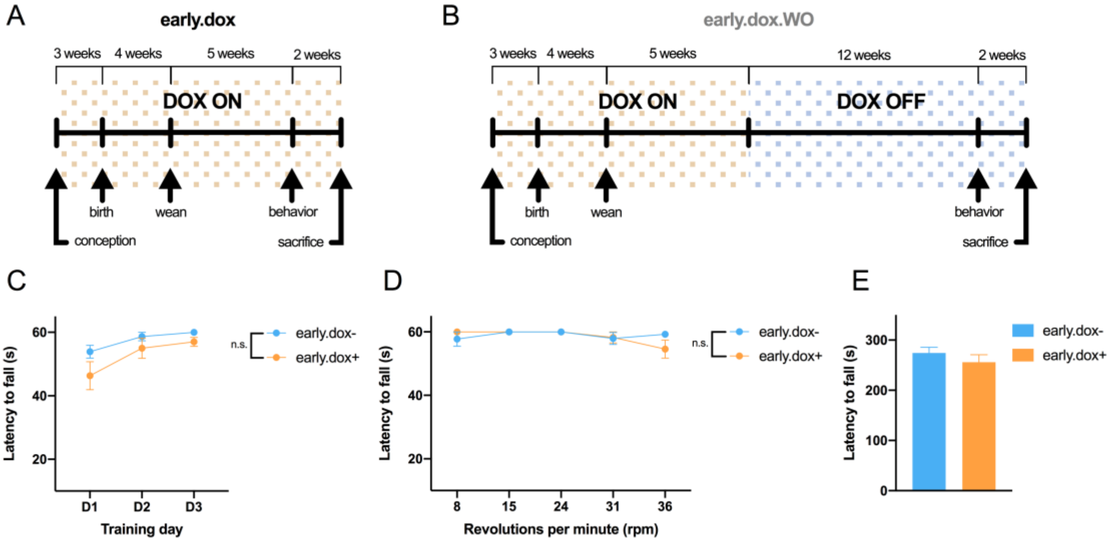

Figure 3.9: Early induction timeline and motor performance of 90xCGG mice
A. *Timeline showing the early dox induction schedule that is used to investigate early occurring phenotypes related to the premutation.* ***B.*** *Timeline showing the wash-out (WO) schedule that is used to investigate rescue possibilities of the phenotypes identified upon an early dox induction.* ***C.*** *On a rotating rod at 15-rpm during a 3-day training session no differences were observed between the dox+ mice and the dox- controls in their latency to fall off the rod.* ***D.*** *During the constant speed rotarod test dox-induced mice showed no differences in their latency to fall off the rod as compared to dox- controls when tested on a rotating rod at various speeds.* ***E.*** *Dox-induced mice did not show any differences in their latency to fall off the rod as compared to their dox- counterparts when they are tested in a speed ramp setting during the accelerating rotarod test. Data presented as mean ± S.E.M. Data obtained in collaboration with Dr. Mónica Santos. For details on ANOVA results see* ***Table S4****.*

In order to investigate the dominant pre-motor symptom of the premutation that falls in the domain of FXAND, mice were subjected to a light/dark transition test that assesses anxiety-like behavior. The dox-induced group spent significantly less time in the lit compartment of apparatus compared to dox- control group, providing evidence for an anxiety-like phenotype (Fig.3.10.A; N(dox-)=11, N(dox+)=7, t=3.505, df=16, P= 0.0029). To address the possibility of a recovery in this phenotype, another group of mice were subjected to the same test following a period of transgene shutdown. Dox+ and dox- groups did not differ from each other in the time they spent in the lit compartment following the wash-out period (Fig.3.10.B; N(dox-.WO)=14, N(dox+.WO)=18, t=0.2901, df=30, P= 0.7737).

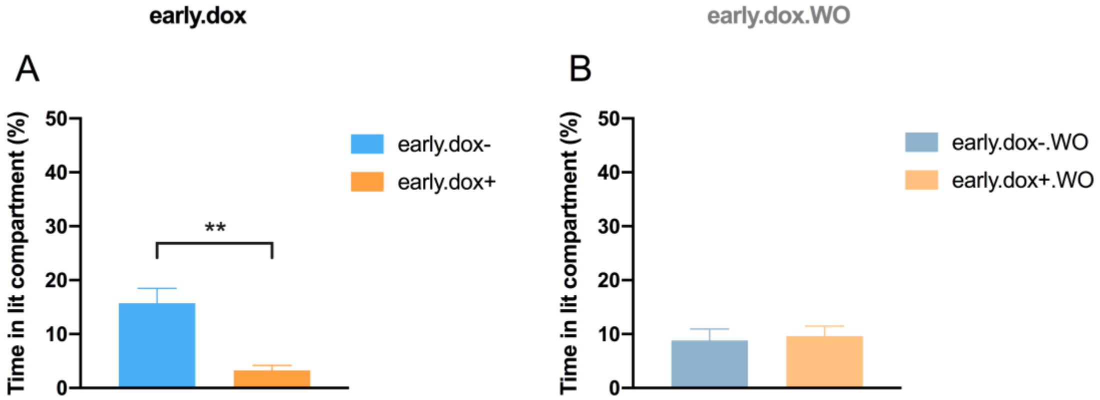

Figure 3.10: Anxiety-like behavior and its rescue following the wash-out
A. *Dox-induced mice spent significantly less time in the lit compartment of the light/dark transition setup as compared to dox- controls.* ***B.*** *Following a 12-week wash-out period, dox-induced mice did not show any differences in the time spent in the lit compartment as compared to dox-.WO controls during the light/dark transition test. Data presented as mean ± S.E.M. **p<0.01. Data obtained in collaboration with Dr. Mónica Santos.*

Next, the intranuclear inclusion pathology was investigated for the early induction timeline via ubiquitin immunohistochemistry in the cerebellum and limbic brain (Fig.3.11.A-B). To assess the possibility of a recovery in the number inclusions, sections obtained from dox+ mice as well as from dox+.WO group were stained for ubiquitin and the percent number of nuclei with ubiquitin focus were determined. No differences were identified in the percent number of ubiquitin foci between dox+ and dox+.WO groups in the cerebellum lobule X (Fig.3.11.C, Lob.X; N(dox+)=8, N(dox+.WO)=6, Student’s t-test, t=1.076, df=12, P= 0.3031), in cornu ammonis-1 (CA1) (Fig.3.11.C, CA1; N(dox+)=7, N(dox+.WO)=6, Student’s t-test, t=0.5700, df=11, P= 0.5801) and CA3 (Fig.3.11.C, CA3; N(dox+)=7, N(dox+.WO)=6, Student’s t-test, t=0.03287, df=11, P=0.9744) of the hippocampus. On the other hand, the percent number of ubiquitin foci was significantly reduced after the wash-out in the dentate gyrus (DG) (Fig.3.11.C, DG; N(dox+)=7, N(dox+.WO)=12, Mann-Whitney test, U=18, P= 0.0430) of the hippocampus and in basolateral amygdala (BLA) (Fig.3.11.C, BLA; N(dox+)=8, N(dox+.WO)=6, Student’s t-test, t=5.327, df=12, P= 0.0002).

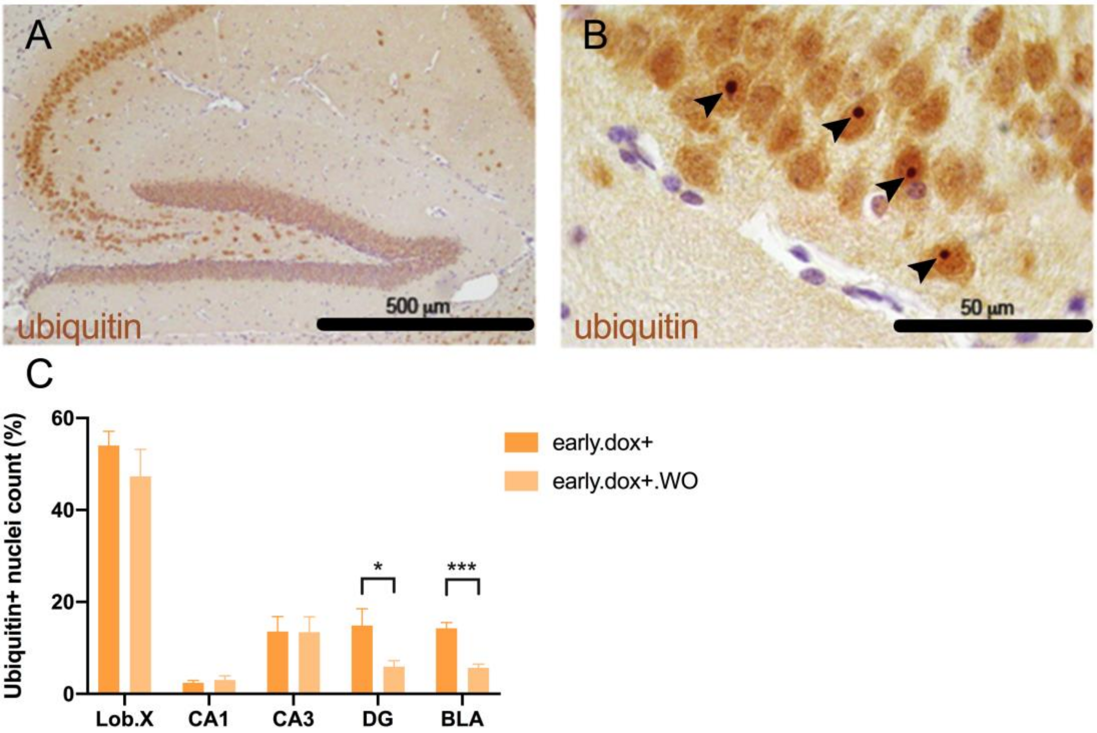

Figure 3.11: Presence of intranuclear inclusions after the early induction schedule and the decrease in the inclusion load in a region-specific manner following wash-out
A. *Representative photomicrograph showing an immunohistochemical staining against ubiquitin (brown) in the hippocampus of dox-induced PrP.90xCGG mouse. Scale bar indicates 500 µm.* ***B.*** *Closeup caption of CA3 showing ubiquitin-foci (dark brown) in the pyramidal neurons. Violet: hematoxylin. Black arrowheads: Ubiquitin foci. Scale bar indicates 50 µm. (A,B: taken from Castro et al. 2017)* ***C.*** *The number of nuclei with ubiquitin-positive intranuclear inclusions have significantly decreased following the wash-out in the dentate gyrus (DG) of the hippocampus and in the basolateral amygdala (BLA), whereas no differences were found either in CA1 and CA3 of the hippocampus or lobule X (lob.X) of the cerebellum. Data presented as mean ± S.E.M. *p<0.05, ***p<0.001. Data obtained in collaboration with Dr. Renate Hukema.*

The two regions, where the there is a possibility of recovery in the percent number of inclusions were then selected for further evaluation via slice electrophysiology. These regions are critical loci with relevance to the modulation of anxiety and depression (Engin et al. 2016), (Y. Yang and Wang 2017). First, lateral amygdala (LA), a nucleus within the BLA was subjected to slice electrophysiology, where a stimulating electrode was placed on the external capsule with the recording electrode on the LA. An input/output curve was obtained by applying stimulation with intensities ranging from 10 to 200 µA. Increased fEPSP amplitudes were observed for dox-induced group as compared to dox- controls for stimulation intensities of 75 µA, 100 µA, 150 µA and 200 µA (Fig.3.12.A; n(dox-)=31, n(dox+)=22, 2-way RM ANOVA, dox-effect; F(1,51)=5.030, P=0.0293, dox x stimulation intensity; F(8,408)=6.736, P<0.0001, Fisher's LSD; 75 µA: P=0.0245, 100 µA: P=0.0257, 150 µA: P=0.0104, 200 µA: P=0.0157, n.s. for other intensities). This difference was, however, normalized when the dox+ group was compared to dox- group following the wash-out period (Fig.3.12.B; n(dox-.WO)=24, n(dox+.WO)=26, 2-way RM ANOVA, dox-effect; F(1,48)=0.2909, P=0.5921, dox x stimulation intensity; F(8,384)=3.944, P=0.0002, Fisher's LSD; n.s. for all intensities). On the other hand, no differences were observed in the high frequency stimulation (HFS) induced LTP between dox+ groups and dox- control groups when tested both before the wash-out period (Fig.3.12.C; n(dox-)=16, n(dox+)=12, 2-way RM ANOVA, dox-effect; F(1,26)=0.08049, P=0.7789, dox x time point; F(19,494)=1.616, P=0.0481, Fisher's LSD; n.s. for all time points) and after the wash-out (Fig.3.12.D; n(dox-.WO)=16, n(dox+.WO)=14, 2-way RM ANOVA, dox-effect; F(1,28)=0.3540, P=0.5566, dox x time point; F(19,532)=2.442, P=0.0006, Fisher's LSD; n.s. for all time points).

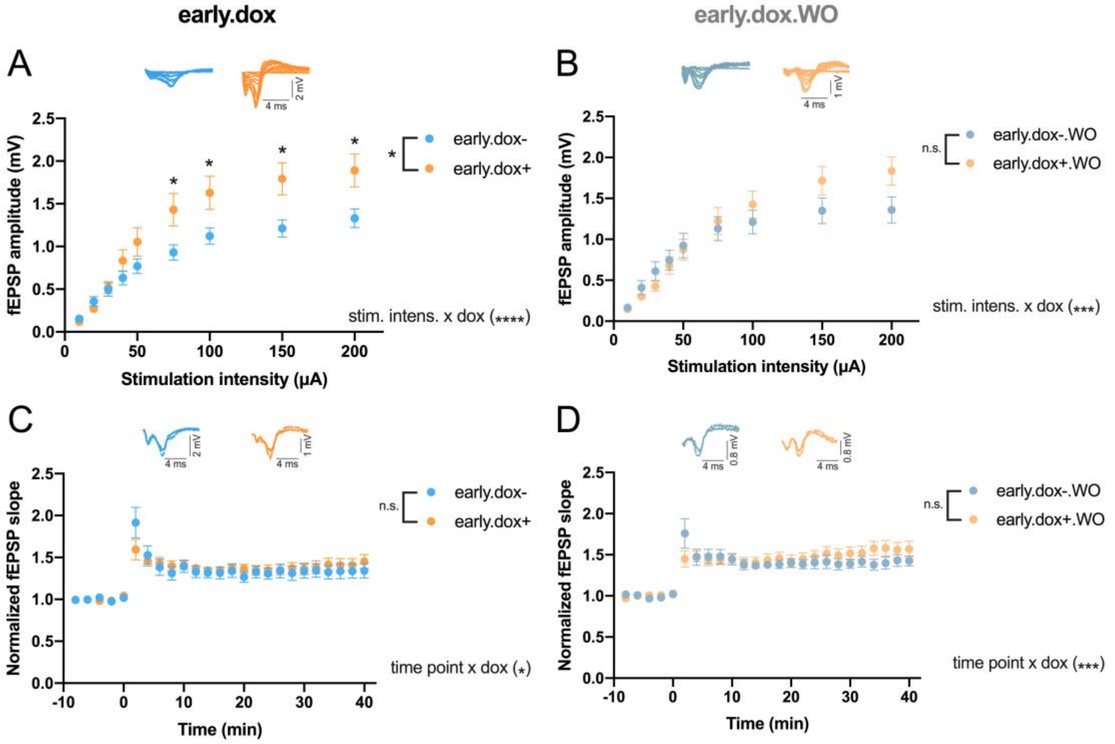

Figure 3.12: Increased excitability in the lateral amygdala and its rescue following the wash-out

*__A.__ Increased field EPSP amplitudes have been recorded from lateral amygdala (LA) slices of dox-induced mice as compared to dox- controls. Field EPSP amplitudes were significantly higher for the dox+ group for stimulation intensities of 75, 100, 150 and 200 μA. __B.__ After the wash-out, no differences have been observed in the field EPSP amplitudes between the slices from dox-treated mice and the dox- mice. __C.__ No differences were observed in the field EPSP slopes obtained from recordings following high frequency stimulation (HFS) between the dox+ and dox- groups. __D.__ After the wash-out, no differences were observed in the EPSP slopes obtained from recordings following the HFS between the dox-treated and dox- groups. Data presented as mean ± S.E.M. *p<0.05, ***p<0.001, ****p<0.0001. Data obtained in collaboration with Dr. Gürsel Çalışkan. For details on ANOVA results see __Table S5__.*

On the contrary in the DG, when the input/output curves were compared, decreased fEPSP amplitudes were observed for the dox+ group as compared to dox- group for all of the stimulation intensities (Fig.3.13.A; n(dox-)=54, n(dox+)=43, 2-way RM ANOVA, dox-effect; F(1,95)=10.77, P=0.0014, dox x stimulation intensity; F(4,380)=3.685, P=0.0059, Fisher's LSD; 10 μA: P=0.0021, 20 μA: P=0.0014, 30 μA: P=0.0021, 40 μA: P=0.0016, 50 μA: P=0.0011). Following the wash-out, no differences were observed between the dox-induced group and the control group in the same parameters (Fig.3.13.B; n(dox-.WO)=24, n(dox+.WO)=46, 2-way RM ANOVA, dox-effect; F(1,68)=0.1258, P=0.7240). HFS induced LTP in the DG revealed higher LTP induction only in the early time points for the dox+ group as compared to the dox- group (Fig.3.13.C; n(dox-)=13, n(dox+)=12, 2-way RM ANOVA, dox-effect; F(1,23)=2.976, P=0.0979, dox x time point; F(19,437)=1.779, P=0.0229, Fisher's LSD; 2 min: P= 0.0140, 4 min: P= 0.0422, n.s. for all other time points). This difference in the early phase LTP was then normalized when dox-induced group and dox- controls were compared after a wash-out period (Fig.3.13.D; n(dox-.WO)=8, n(dox+.WO)=11, 2-way RM ANOVA, dox-effect; F(1,17)=0.9310, P=0.3481).

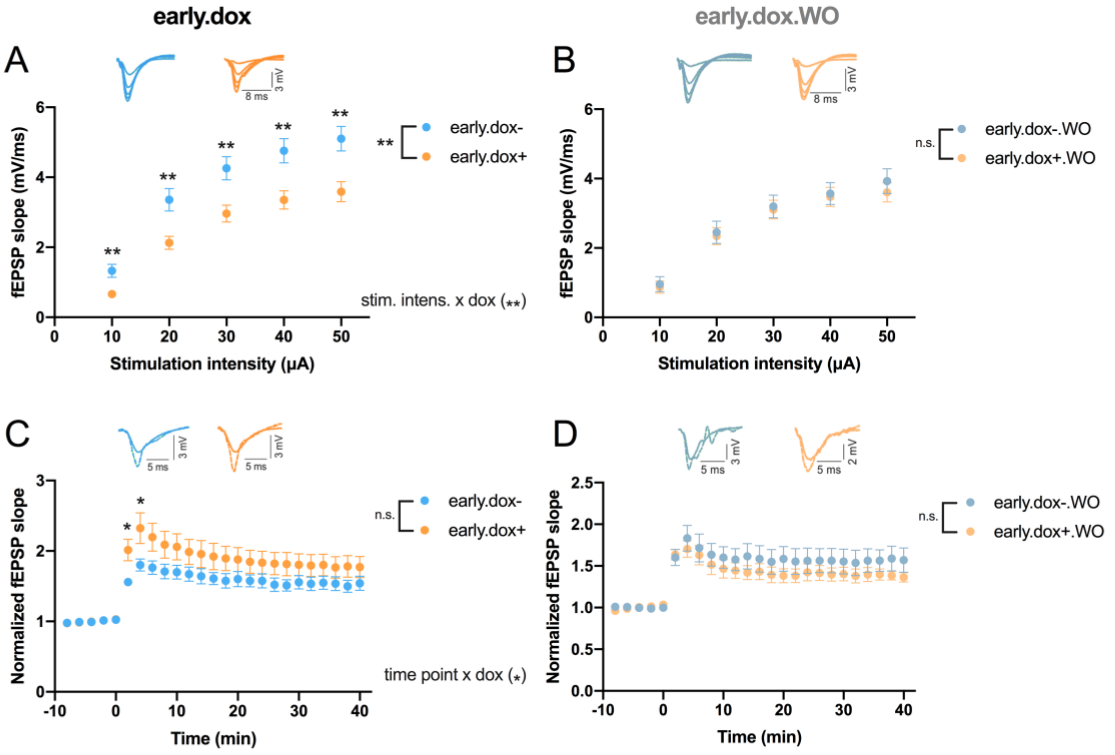

Figure 3.13: Decreased excitability coupled with an increase in the early long-term potentiation in the dentate gyrus and their rescue following the wash-out

A.** Decreased field EPSP slopes have been observed in the DG of dox-induced mice as compared to dox- controls. Field EPSP slopes were significantly lower for the dox+ group for all of the individual stimulation intensities. **B.** After the wash-out, no differences have been observed in the field EPSP* *slopes between the slices from dox-treated mice and the dox- mice.* ***C. *Field EPSP slopes HFS were significantly higher only at time points 2 and 4 minutes following the HFS.* ***D.*** *After the wash-out, no differences were observed in the EPSP slopes obtained from recordings following the HFS between the dox-treated and dox- groups. Data presented as mean ± S.E.M. *p<0.05, **p<0.01. Data obtained in collaboration with Dr. Gürsel Çalışkan. For details on ANOVA results see* ***Table S6****.*

3.2 Novel treatment strategies against FXTAS in the PrP.90xCGG mouse model

Rescue possibilities for the phenotypes observed in the PrP.90xCGG model have been previously explored using the wash-out regime (Castro et al. 2017). However, simply shutting down the transgene containing the expanded repeats and allowing the organism time to recover has proven to be insufficient, especially for cerebellar phenotypes. Therefore, two distinct, potentially therapeutic strategies that are based on intervention by external agents have been explored.

3.2.1 Induction of autophagy by trehalose supplementation

RATIONALE - The aggregation that gives rise to the intranuclear inclusion pathology has been proposed to reflect a neurotoxic action and been linked to dysfunctions involving the ubiquitin proteasome system (UPS) in FXTAS (Oh et al. 2015). FXTAS inclusions have been shown to contain P62, an adapter protein that can bind aggregated proteins and direct them to the autophagosome for degradation (Wooten et al. 2006) suggesting they are targeted for degradation via autophagy-lysosome pathway but could not exit the nucleus (Ma et al. 2019). In an effort to fight aggregation as it occurs, trehalose, an autophagy inducer (Mardones, Rubinsztein, and Hetz 2016) has been supplemented to the PrP.90xCGG mice for 12 weeks starting and ending simultaneously with the dox-induction (Fig.3.14.A).

The inclusions found in the cerebellum lobule X of the 12 weeks dox-induced mice stain positively for P62 (Fig.3.14.B) as well as for FMRpolyG (Fig.3.14.C). The percent number of nuclei with FMRpolyG focus quantified from the granular layer of the cerebellum lobule X (Fig.3.14.D) has been significantly reduced in the trehalose supplemented group (Fig.3.14.E; Student's t-test, N(dox+.treh-)=11, N(dox+.treh+)=11, t=3.154, df=20, P= 0.0050). The average size of the FMRpolyG foci has also been reduced upon trehalose supplementation (Fig.3.14.F; N(dox+.treh-)=11, N(dox+.treh+)=11, Student's t-test, t=2.832, df=20, P= 0.0103).

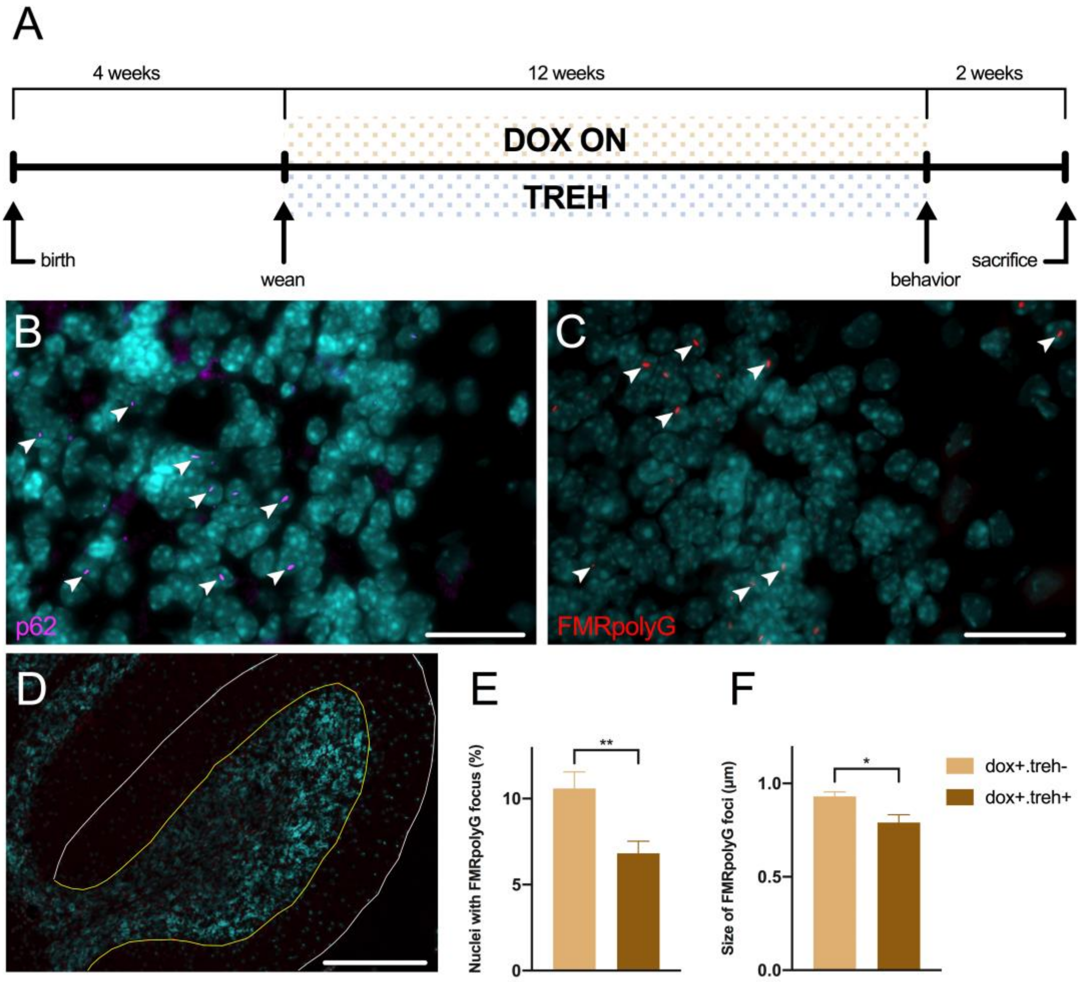

Figure 3.14: Trehalose supplementation schedule and recovery in the inclusion load upon treatment

***A.** Timeline showing the dox-induction and trehalose supplementation schedule used in order to investigate the therapeutic potential of trehalose (treh) in vivo. **B.** High magnification photomicrograph showing the P62-positive inclusions (magenta) colocalizing with various nuclei within the granular layer of the cerebellum lobule X. Blue: DAPI. White arrowheads: p62 foci (not all foci marked). Scale bar indicates 25 μm. **C.** High magnification photomicrograph showing the FMRpolyG-positive inclusions (red) colocalizing with various nuclei within the granular layer of the cerebellum lobule X. Blue: DAPI. White arrowheads: FMRpolyG foci (not all foci marked). Scale bar indicates 25 μm. **D.** Representative photomicrograph showing cerebellum lobule X, the read-out region used for FMRpolyG foci quantifications. Blue:DAPI. Outer contour (white): lobule X, inner contour (yellow): granular layer of lobule X. Scale bar indicates 250 μm **E.** Quantified from the granular layer of cerebellum lobule X, trehalose-treated mice had significantly smaller number of nuclei with FMRpolyG focus as compared to treh- controls. **F.** The FMRpolyG foci were significantly smaller in size with the trehalose-treated group as compared to treh- group. Data presented as mean ± S.E.M. *p<0.05, **p<0.01.*

In order to assess whether trehalose supplementation has indeed induced autophagy or not western blots against LC3-II (Fig.3.15.A) of trehalose supplemented groups versus non supplemented groups were quantified (N(dox-.treh-)=8, N(dox-.treh+)=8, N(dox+.treh-)=8, N(dox+.treh+)=8). Trehalose supplementation has been found to increase LC3-II levels as quantified from cerebellum tissue of a group of naïve mice (Fig.3.15.B; 2-way ANOVA, treh-effect; F(1,28)=5.655, P=0.0245).

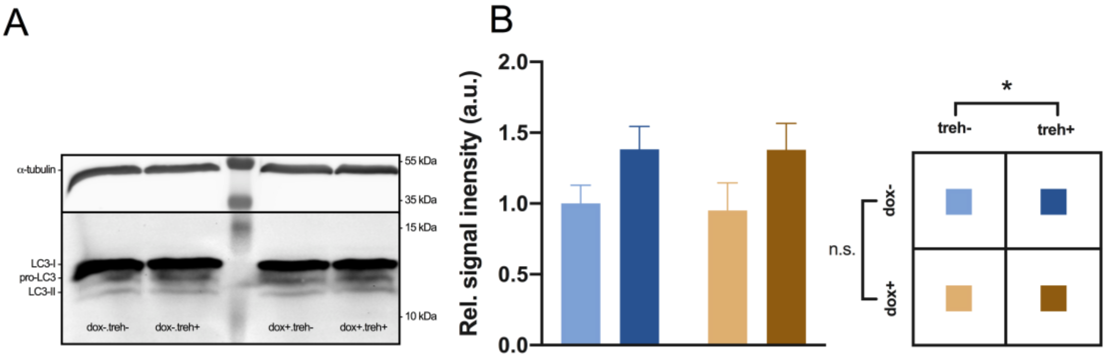

Figure 3.15: Increased LC3-II levels upon trehalose supplementation

***A.** Representative western blot image showing fluorescent signal specific to α-tubulin and LC3 under four different dox and trehalose conditions. Notice the three isoforms of LC3 detected by the primary antibody. **B.** Quantification of the LC3-II signal relative to α-tubulin signal. Trehalose treatment significantly increased the LC3-II signal. Data presented as mean ± S.E.M. *p<0.05. For details on ANOVA results see **Table S7**.*

Next, the motor performance has been evaluated under the trehalose supplementation (N(dox-.treh-)=10, N(dox-.treh+)=10, N(dox+.treh-)=11, N(dox+.treh+)=11). On a rotating rod at slow speed (15 rpm) during the training session, no significant effects of either dox or trehalose were observed (Fig.3.16.A; 3-way ANOVA, dox-effect; F(1,38)=2.506, P=0.1217, treh-effect; F(1,38)=2.098, P=0.1557) and all four groups reached a comparable acclimation level at the end of the training session. During the constant speed rotarod test, when the mice were made to run on a rotating rod at various constant speeds, an adverse effect of dox on latencies to fall off the rod was observed together with a positive trehalose effect improving the motor performance (Fig.3.16.B; 3-way ANOVA, dox-effect; F(1,38)=26.39, P<0.0001, treh-effect; F(1,38)=6.482, P=0.0151). A significant dox x treh interaction was also present pointing out to differential effects of trehalose supplementation on dox-induced and dox- groups, counteracting the detrimental effect of dox-induction on motor performance (3-way ANOVA, dox-effect x treh-effect; F(1,38)=6.521, P=0.0148, Fisher's LSD; 31rpm; dox-.treh- vs. dox+.treh-: P=0.0110, dox-.treh+ vs. dox+.treh-: P=0.0073, 36rpm; dox-.treh- vs. dox+.treh-: P=0.0072, dox-.treh+ vs. dox+.treh-: P=0.0153, dox+.treh- vs. dox+.treh+: P=0.0448, 40rpm; dox-.treh- vs. dox+.treh-: P=0.0078, dox-.treh+ vs. dox+.treh-: P=0.0008. For details on the post-hoc analysis see Table S8.). On the last session of the rotarod-test, mice were tested for their latencies to fall off the rod during a speed ramp of 4-40 rpm. An adverse effect of dox on the performance on the accelerating rod was observed and trehalose was able to exert a positive effect on the performance (Fig.3.16.C; 2-way ANOVA, dox-effect; F(1,38)=24.77, P<0.0001, treh-effect; F(1,38)=10.66, P=0.0023). Again, trehalose acted differentially on the motor performance of the dox-induced and dox- groups (2-way ANOVA, dox-effect x treh-effect; F(1,38)=7.622, P=0.0088, Fisher's LSD; dox-.treh- vs. dox+treh-: P<0.0001, dox-.treh+ vs. dox+.treh-: P<0.0001, dox-.treh+ vs. dox+.treh+: P<0.0001, other pair-wise comparisons n.s. For details on the post-hoc analysis see Table S8). The weight of the mice subjected to the rotarod-test have also been recorded and compared in order to identify changes that may have been resulted by dox-induction or trehalose supplementation because body weight differences may influence motor performance (N(dox-.treh-)=10, N(dox-.treh+)=10, N(dox+.treh-)=11, N(dox+.treh+)=11). No significant effects of either dox or trehalose has been found on the body weights of mice (Fig.3.16.D; 2-way ANOVA, dox-effect; F(1,38)=2.352, P=0.1334, treh-effect; F(1,38)=0.9545, P=0.2318).

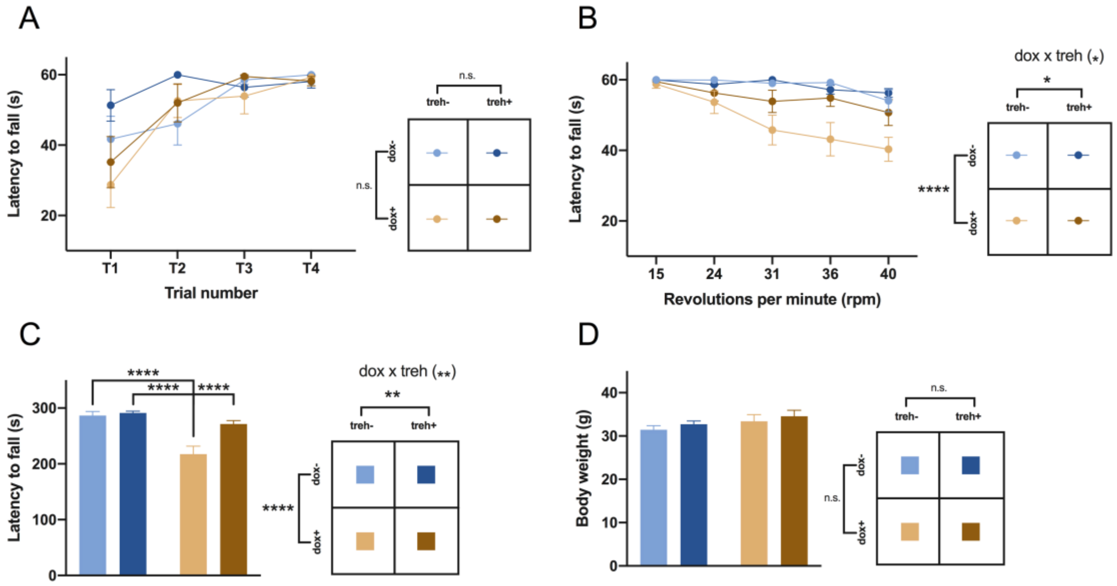

Figure 3.16: Recovery in the motor performance upon trehalose treatment

_A._ _On a rotating rod at 15-rpm during a 1-day, 4-trial training session no significant effects were observed either for dox or trehalose treatment in the latency to fall off the rod._ **_B._** _During the constant speed rotarod test dox-induction significantly decreased the latency to fall off the rod whereas trehalose treatment significantly increased the time the mice spent on the rod that rotates at various speeds before they fall_ **_C._** _Dox-induction significantly decreased the latency to fall off the rod when the mice are tested in a speed ramp setting during the accelerating rotarod test. Contrastingly, trehalose treatment significantly increased the latency of the mice to fall off the rod._ **_D._** _Neither dox-induction nor trehalose supplementation significantly affected the body weights of the mice. Data presented as mean ± S.E.M. *p<0.05, **p<0.01, ****p<0.0001. For details on ANOVA results see_ **_Table S8_**_._

A series of correlation analyses have been performed to investigate whether number of inclusions and their size are predictors of the motor performance or not (N(dox+.treh-)=11, N(dox+.treh+)=11). When the latencies to fall off the rod of each individual dox-induced mouse during the accelerating rotarod-test were paired with the percent number of nuclei each mouse has with a FMRpolyG focus a significant negative correlation was observed (Fig.3.17.A; Pearson correlation, r=-0.4457, P=0.0376). A similar negative correlation was also observed when the motor performance on the accelerating rotarod was crossed with intranuclear inclusions size (Fig.3.17.B; Pearson correlation, r=-0.4423, P=0.0393). Moreover, the percent number of nuclei with inclusions significantly correlated positively with the size of the inclusions (Fig.3.17.C; Pearson correlation, r=0.7605, P<0.0001).

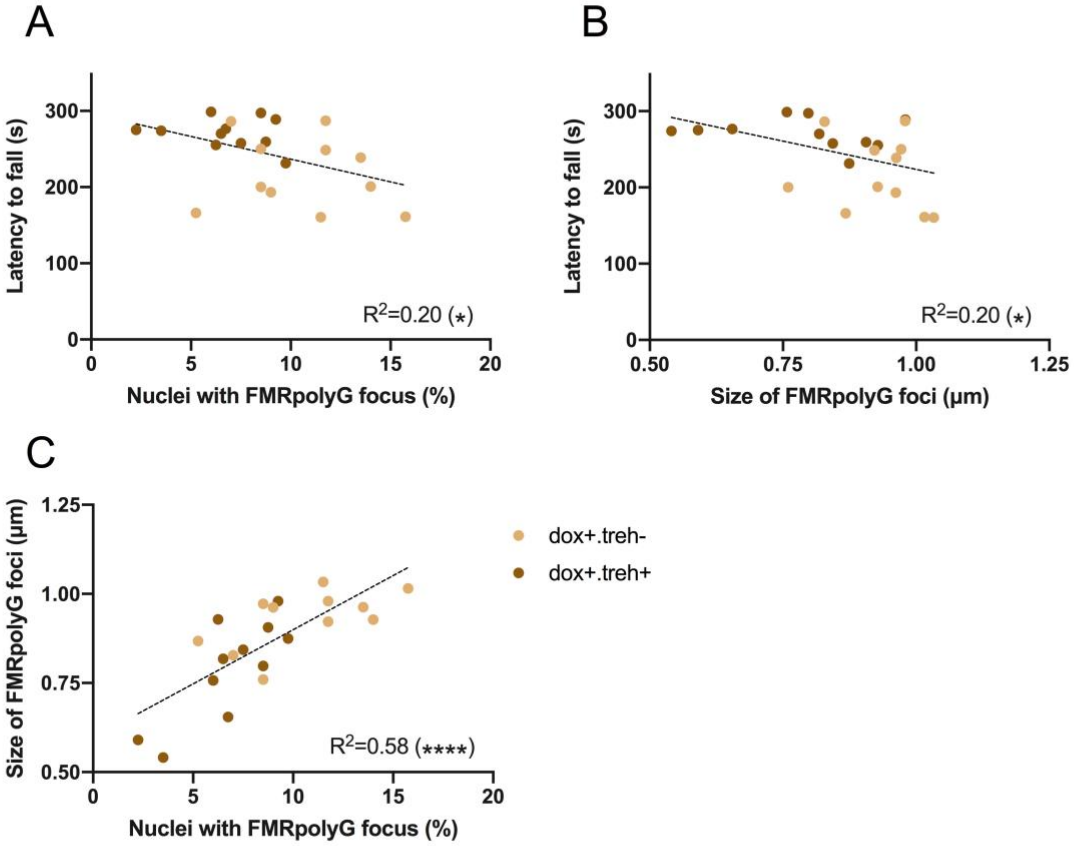

Figure 3.17: Motor performance correlates with the inclusion load in the lobule X
Statistically significant negative correlation was identified between the latencies to fall off the rod of individual mice during the accelerating rotarod task and ***A.*** *their number of nuclei with FMRpolyG focus in the lobule X,* ***B.*** *the size of the FMRpolyG foci.* ***C.*** *Statistically significant positive correlation was identified between the number of nuclei with FMRpolyG focus in the lobule X and the size of these FMRpolyG foci. Data presented as individual values. *p<0.05, ****p<0.0001.*

On top of the motor performance parameters that are the most crucial read-outs for assessing potential benefits of any intervention strategy within the context of FXTAS, potential effects of trehalose on other previously investigated behavioral domains (Castro et al. 2017) were also explored. For paw-print analyses mice were made to walk on a straight line on a white sheet of paper with their fore- and hind paws colored in blue and red respectively (Fig.3.18.A). Six different gait parameters were measured from the paw prints. Neither dox nor trehalose had any significant effects on any of the six parameters analyzed (N(dox-.treh-)=10, N(dox-.treh+)=11, N(dox+.treh-)=11, N(dox+.treh+)=13), including uniformity of step alternation (Fig.3.18.B; 2-way ANOVA, dox-effect; F(1,41)=0.9365, P=0.3389, treh-effect; F(1,41)=0.2659, P=0.6089), forepaw width (Fig.3.18.C; 2-way ANOVA, dox-effect; F(1,41)=1.018, P=0.3188, treh-effect; F(1,41)=0.1568, P=0.6942), hind paw width (Fig.3.18.D; 2-way ANOVA, dox-effect; F(1,41)=0.01672, P=0.8977, treh-effect; F(1,41)=0.004277, P=0.9482), stride length (Fig.3.18.E; 2-way ANOVA, dox-effect; F(1,41)=3.465, P=0.0699, treh-effect; F(1,41)=0.7212, P=0.4007), overlap symmetry (Fig.3.18.F; 2-way ANOVA, dox-effect; F(1,41)=0.6407, P=0.4281, treh-effect; F(1,41)=2.665, P=0.1102) and alternation coefficient (Fig.3.18.G; 2-way ANOVA, dox-effect; F(1,41)=1.004, P=0.3221, treh-effect; F(1,41)=0.8086, P=0.3738).

Within the domain of anxiety, three different tests that are sensitive to changes in the anxiety levels were performed. In the light/dark transition test the duration of the visits of the mice to the two distinct compartments of the setup was recorded (N(dox-.treh-)=10, N(dox-.treh+)=11, N(dox+.treh-)=11, N(dox+.treh+)=13) . No effects related either to dox or trehalose was observed in the percent time the mice spent in the lit compartment (Fig.3.19.A; 2-way ANOVA, dox-effect; F(1,41)=2.898, P=0.0963, treh-effect; F(1,41)=0.08333, P=0.7743). In the marble burying task mice were exposed to 15 glass marbles laying on a thick cover of bedding in a standard mouse cage and the number of marbles they bury in the bedding was recorded (N(dox-.treh-)=9, N(dox-.treh+)=11, N(dox+.treh-)=11, N(dox+.treh+)=13). Dox-induction has significantly increased the number of marbles buried during the task, but no effect related to trehalose was observed (Fig.3.19.B; 2-way ANOVA, dox-effect; F(1,40)=5.115, P=0.0292, treh-effect; F(1,40)=0.004864, P=0.9447). In the open field arena, the time the mice spent in the center of the arena under dim light conditions were recorded as an anxiety parameter and the total distance they covered exploring the arena as a measure of locomotion (N(dox-.treh-)=10, N(dox-.treh+)=11, N(dox+.treh-)=11, N(dox+.treh+)=13). Dox-induction had no significant effects on the time mice spent in the center of the arena (Fig.3.19.C; 3-way ANOVA, dox-effect; F(1,41)=1.150, P=0.2899).

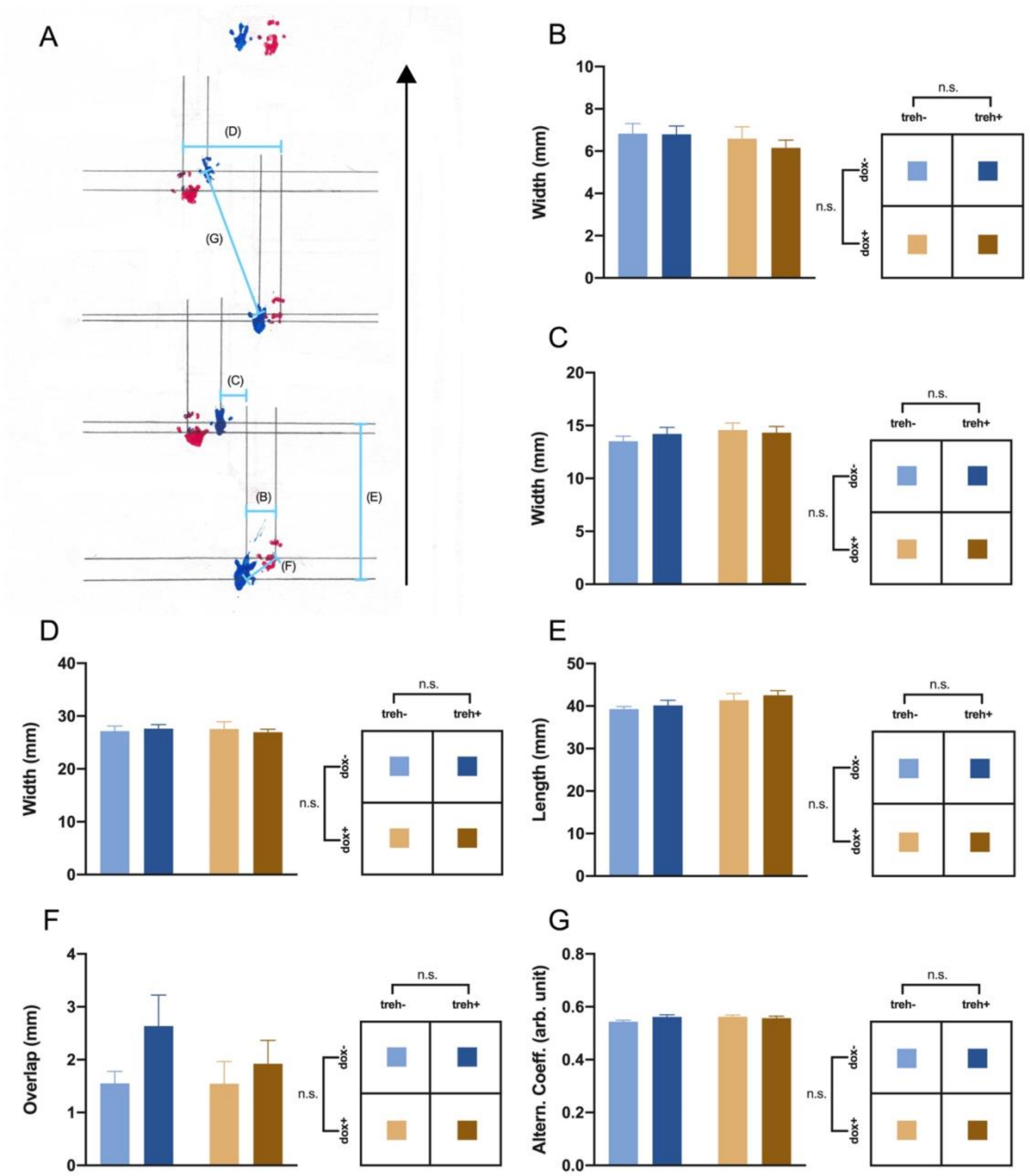

Figure 3.18: Gait parameters under trehalose treatment

***A.** Visual representation of a pawprint that is used to quantify various gait measures. Blue prints: forepaws, red prints: hind paws, black arrow: walking direction. No significant effects were observed either for dox-induction or trehalose treatment in the measures **B.** uniformity of step alternation, **C.** forepaw width, **D.** hind paw width, **E.** stride length, **F.** overlap symmetry, **G.** alternation coefficient. Data presented as mean ± S.E.M. For details on ANOVA results see **Table S9**.*

Additionally, a significant dox x treh interaction was present, indicating that trehalose affects dox-induced and dox- groups differentially without having an intrinsic effect on the time spent in the center parameter (3-way ANOVA, treh-effect; F(1,41)=3.692, P=0.0616, dox-effect x treh-effect; F(1,41)=8.551, P=0.0056, Fisher's LSD; 5min; dox-.treh- vs. dox-.treh+: P=0.0469, dox-.treh- vs. dox+.treh-: P=0.0236, 10min; dox-.treh- vs. dox-.treh+: P=0.0390, other pair-wise comparisons n.s. For details on the post-hoc analysis see **Table S10**). The distance covered in the open field arena was also unaffected by both dox and trehalose (Fig.3.19.D; 3-way ANOVA, dox-effect; F(1,41)=1.813, P=0.1855, treh-effect; F(1,41)=0.4517, P=0.5053).

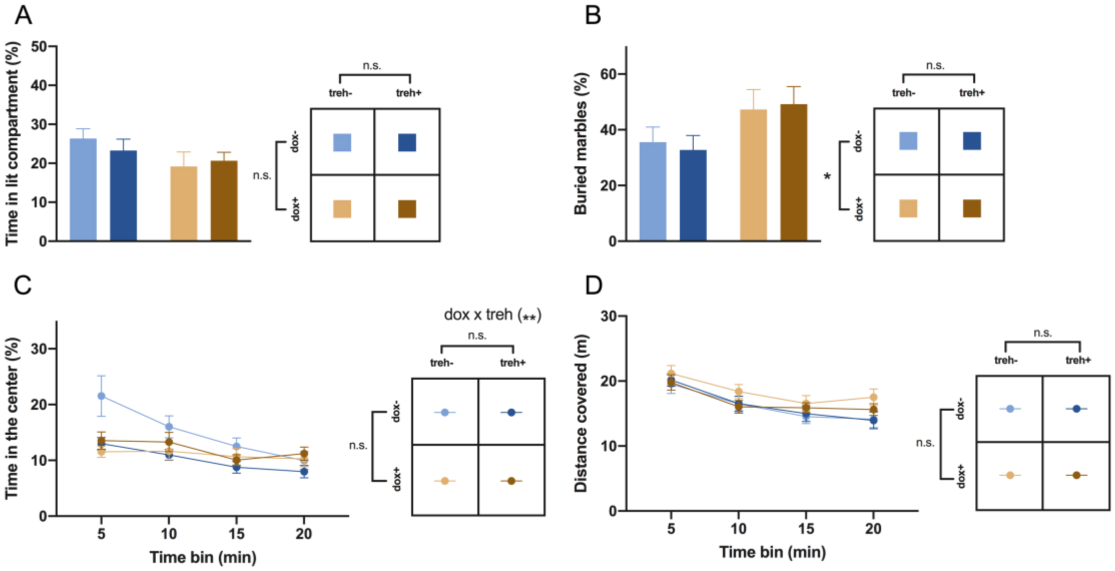

Figure 3.19: Anxiety and locomotion under trehalose treatment
A. *No significant effects were observed either for dox-induction or trehalose treatment in the time spent in the lit compartment of the light/dark transition setup.* ***B.*** *Dox-induction significantly increased the number of marbles buried during the marble burying task, whereas trehalose treatment had no significant effects on the task.* ***C.*** *No significant effects were observed either for dox-induction or trehalose treatment in the time spent in the center of the open field arena.* ***D.*** *Distance covered measure in the open field arena was not affected either by the dox-induction or the trehalose treatment. Data presented as mean ± S.E.M. *p<0.05, **p<0.01. For details on ANOVA results see* ***Table S10****.*

Potential effects of dox-induction and trehalose supplementation on associative learning and memory has been investigated under a trace fear conditioning paradigm (N(dox-.treh-)=10, N(dox-.treh+)=11, N(dox+.treh-)=11, N(dox+.treh+)=13). In the trace fear conditioning paradigm, an auditory cue is presented together with a mild foot-shock to the mice in an uncoupled manner with the aim of inducing a freezing behavior. The tone and the foot-shock are separated by a time interval called the trace interval (Fig.3.20.A). During the training session of the trace fear conditioning paradigm, freezing levels of the mice were recorded before and after the training. No significant effects of either dox or trehalose on the freezing behavior were observed (Fig.3.20.B; 2-way ANOVA, pre: dox-effect; F(1,41)=1.536, P=0.2223, treh-effect; F(1,41)=0.001156, P=0.9730, post: dox-effect; F(1,41)=1.273, P=0.2658, treh-effect; F(1,41)=1.338, P=0.2540). Then, the mice were tested for their context dependent fear memory. Memory retrieval in the shock context as well as in the neutral context was not affected by dox-induction and by trehalose supplementation (Fig.3.20.C; 2-way ANOVA, shock: dox-effect; F(1,41)=0.1961, P=0.6602, treh-effect; F(1,41)=0.1143, P=0.7370, neutral: dox-effect; F(1,41)=0.5226, P=0.4738, treh-effect; F(1,41)=0.0003970, P=0.9842). Next, the fear memory of the mice was retrieved upon the auditory cue presentation. Neither dox nor trehalose had significant effects on the freezing levels upon conditioned stimulus (CS+) presentation or during the trace interval (Fig.3.20.D; 2-way ANOVA, CS+: dox-effect; F(1,41)=0.004162, P=0.9489, treh-effect; F(1,41)=1.909, P=0.1746, trace: dox-effect; F(1,41)=0.2257, P=0.6373, treh-effect; F(1,41)=0.7053, P=0.4059).

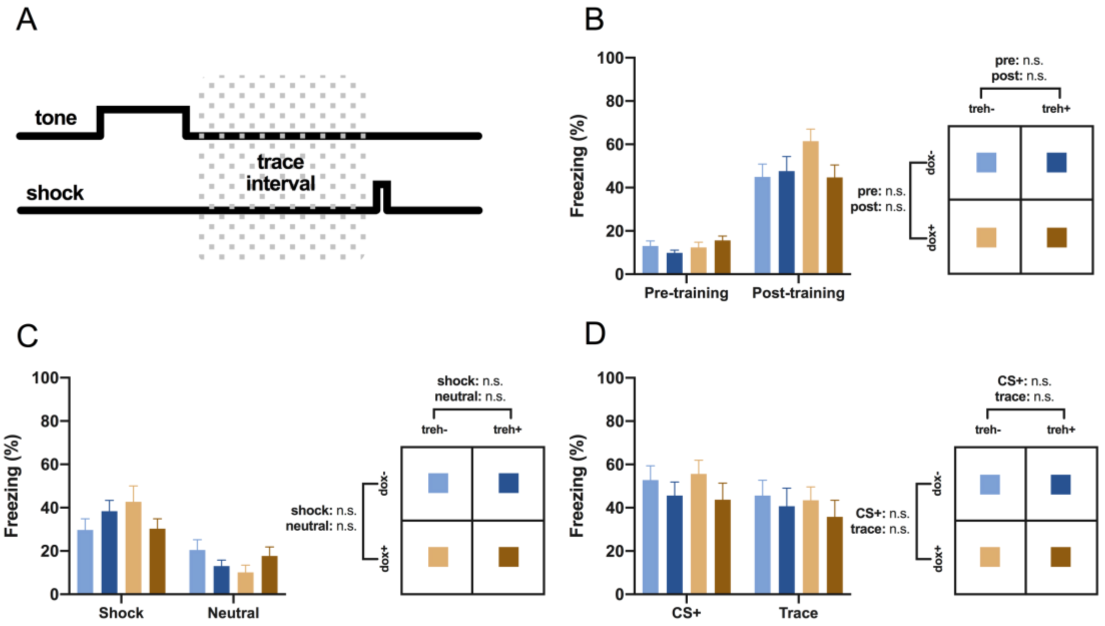

Figure 3.20: Associative learning and memory under trehalose treatment
A. *Schematic presentation of the trace fear conditioning protocol, where a tone and a mild foot-shock are presented in an uncoupled manner, separated with a time gap that is called the trace interval.* ***B.*** *No significant effects were observed either in the pre-training or in the post-training freezing levels for any of the treatments as recorded during the training session* ***C.*** *During the context retrieval session, the freezing levels of the mice remained unaffected by any of the treatments both in the shock context and in a neutral context.* ***D.*** *In the cue retrieval session, no significant effects on the freezing levels were observed either to the conditioned tone (CS+) or during the trace interval. Data presented as mean ± S.E.M. For details on ANOVA results see* ***Table S11****.*

3.2.1.1 Timing control of trehalose by supplementation in the wash-out

RATIONALE - Under assumption that induction of autophagy may be viable for degradation of aggregates only before they are fully formed and are too big to exit the nucleus (Ma et al. 2019), trehalose was supplemented to the PrP.90xCGG mice in the wash-out for 12 weeks following a 12 week dox-induction period as a control experiment (Fig.3.21.A).

First, the motor performance of the mice was tested on the rotarod (N(dox-.WOtreh-)=10, N(dox-.WOtreh+)=9, N(dox+.WOtreh-)=10, N(dox+.WOtreh+)=9). No effects of either dox-induction or trehalose supplementation in the wash-out were observed during the training session and all groups reached similar acclimation levels at the end of the session (Fig.3.21.B; 3-way ANOVA, dox-effect; F(1,34)=2.649, P=0.1128, treh-effect; F(1,34)=1.472, P=0.2334). During the constant speed rotarod test, dox-induction has found to adversely affect the motor performance (lower latency to fall), whereas no significant effects of trehalose could be established (Fig.3.21.C; 3-way ANOVA, dox-effect; F(1,34)=15.56, P=0.0004, treh-effect; F(1,34)=0.8237, P=0.3705). Dox-induction was revealed to have detrimental effects on motor performance also on the accelerating rotarod test but trehalose supplementation in the wash-out had no significant effects (Fig.3.21.D; 2-way ANOVA, dox-effect; F(1,34)=10.99, P=0.0022, treh-effect; F(1,34)=1.011, P=0.3219). Moreover, the body weights of the mice were affected by dox-induction but not from trehalose supplementation; dox+ groups suffered from increased body weight (Fig.3.21.E; 2-way ANOVA, dox-effect; F(1,34)=35.81, P<0.0001, treh-effect; F(1,34)=1.278, P=0.2662). In order to determine if this body weight change had in any way interfered with the rotarod results, a correlation analysis was done pairing the individual performance of the mice on the acceleration rotarod with their body weight. However, this analysis was performed separately for dox-induced groups and non-induced groups in two rounds, in order to avoid finding effects related to the already determined differences in both of these parameters between dox+ and dox- groups. No significant correlation was identified when the latency to fall parameter was crossed with the body weights either for dox-induced or for dox- groups (Fig.3.21.F-G; Pearson correlation, dox-: r=-0.2234, P=0.3579, dox+: r=-0.2873, P=0.2330).

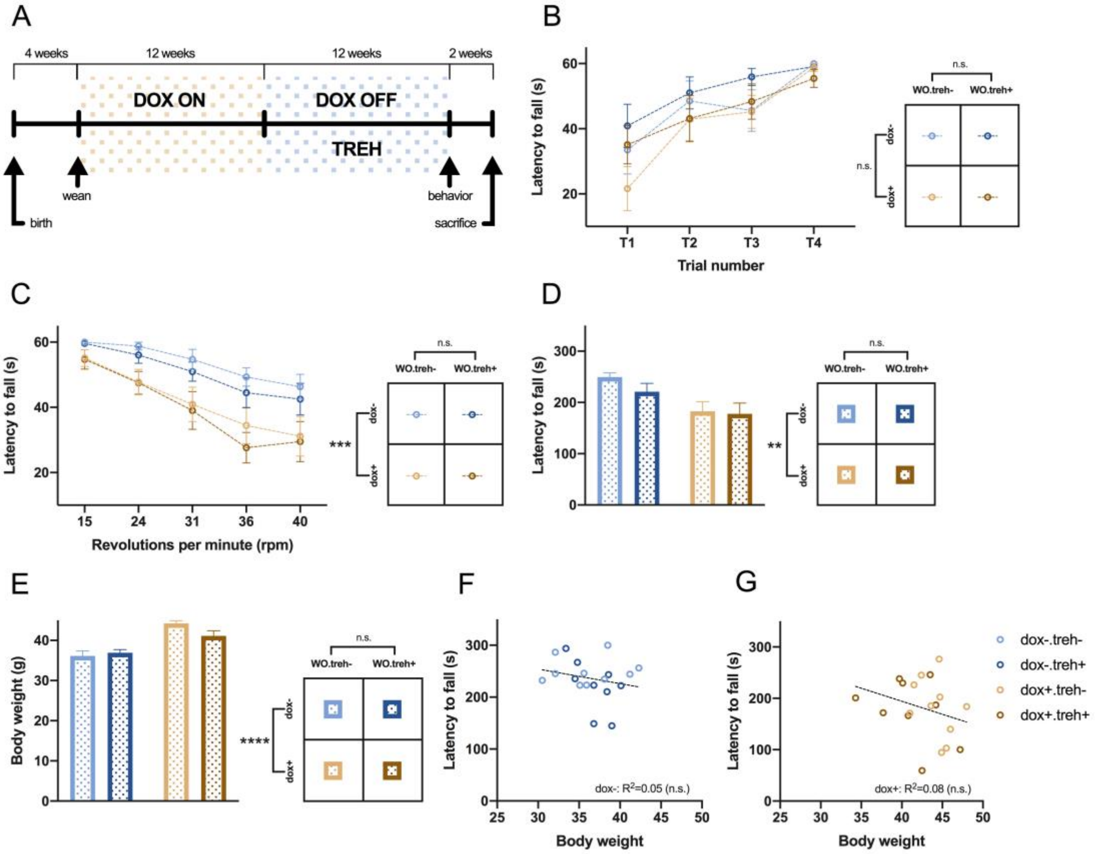

Figure 3.21: Trehalose supplementation schedule in the wash-out and motor performance
A. *Timeline showing the dox-induction and trehalose supplementation schedule used in order to control for the timing of trehalose as a therapeutic strategy in vivo.* ***B.*** *On a rotating rod at 15-rpm during a 1-day, 4-trial training session no significant effects were observed either for dox or trehalose treatment in the latency to fall off the rod.* ***C.*** *During the constant speed rotarod test dox-induction significantly decreased the latency to fall off the rod whereas trehalose treatment had no effect on the time the mice spent on the rod that rotates at various speeds before they fall* ***D.*** *Dox-induction significantly decreased the latency to fall off the rod when the mice are tested in a speed ramp setting during the accelerating rotarod test. Trehalose treatment had no effect on the latency of the mice to fall off the rod.* ***E.*** *Dox-induction significantly increased the body weights of the mice after the wash-out, whereas no treatment effect was observed for trehalose on body weight. Data presented as mean ± S.E.M. No significant correlation was identified between the latencies to fall off the rod of individual mice during the accelerating rotarod task and their body weights neither for* ***F.*** *the dox-induced groups or for* ***G.*** *the dox- groups***).** *Data presented as individual values. **p<0.01, ***p<0.001, ****p<0.0001. For details on ANOVA results see* ***Table S12****.*

Next, paw prints of the mice were analyzed for the six gait parameters (N(dox-.WOtreh-)=10, N(dox-.WOtreh+)=9, N(dox+.WOtreh-)=10, N(dox+.WOtreh+)=9). Neither dox nor trehalose had any significant effects on any of the parameters analyzed including uniformity of step alternation (Fig.3.22.A; 2-way ANOVA, dox-effect; F(1,34)=0.008394, P=0.9275, treh-effect; F(1,34)=0.03430, P=0.8542), forepaw width (Fig.3.22.B; 2-way ANOVA, dox-effect; F(1,34)=0.6429, P=0.4282, treh-effect; F(1,34)=1.085, P=0.3050), hind paw width (Fig.3.22.C; 2-way ANOVA, dox-effect; F(1,34)=0.1192, P=0.7321, treh-effect; F(1,34)=0.6121, P=0.4394), stride length (Fig.3.22.D; 2-way ANOVA, dox-effect; F(1,34)=0.0009927, P=0.9750, treh-effect; F(1,34)=3.743, P=0.0614), overlap symmetry (Fig.3.22.E; 2-way ANOVA, dox-effect; F(1,34)=0.1080, P=0.7445, treh-effect; F(1,34)=0.3412, P=0.5630) and alternation coefficient (Fig.3.22.F; 2-way ANOVA, dox-effect; F(1,34)=0.1788, P=0.6751, treh-effect; F(1,34)=0.1674, P=0.6850).

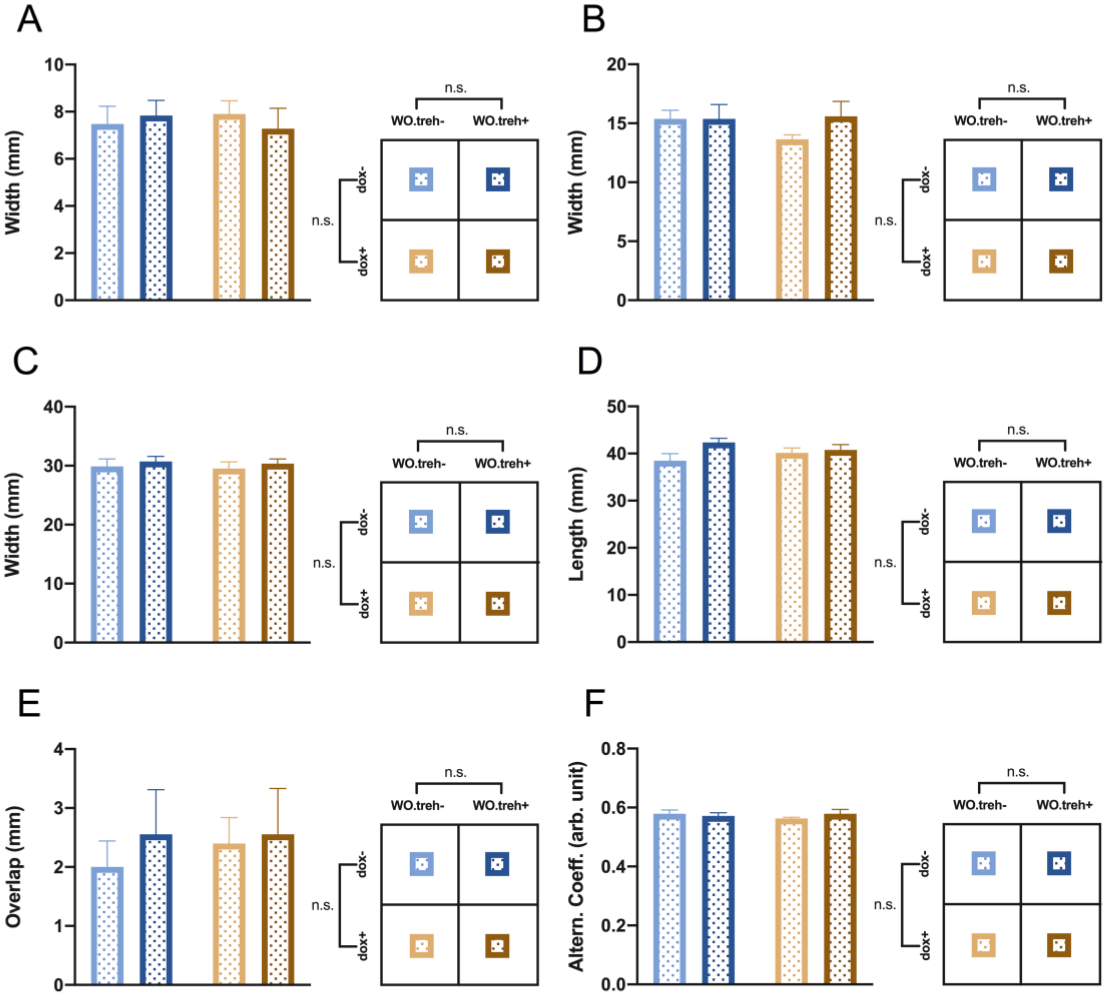

Figure 3.22: Gait parameters under trehalose treatment in the wash-out
No significant effects were observed either for dox-induction or trehalose treatment in the measures ***A.*** *uniformity of step alternation,* ***B****. forepaw width,* ***C.*** *hind paw width,* ***D.*** *stride length,* ***E.*** *overlap symmetry,* ***F.*** *alternation coefficient. Data presented as mean ± S.E.M. For details on ANOVA results see* ***Table S13****.*

For the anxiety measures tested (N(dox-.WOtreh-)=10, N(dox-.WOtreh+)=9, N(dox+.WOtreh-)=10, N(dox+.WOtreh+)=9), dox-induction significantly decreased the time mice spent in the lit compartment of the light/dark transition setup (Fig.3.23.A; 2-way ANOVA, dox-effect; F(1,34)=12.71, P=0.0011), increased the number of marbles buried (Fig.3.23.B; 2-way ANOVA, dox-effect; F(1,34)=25.96, P<0.0001) and decreased the time mice spent in the center of the open field arena (Fig.3.23.C; 3-way ANOVA, dox-effect; F(1,34)=4.309, P=0.0455). Trehalose supplemented in the wash-out had no significant effects on those three anxiety tests (2-way ANOVA, light/dark: treh-effect; F(1,34)=0.4375, P=0.5128, marble burying: treh-effect; F(1,34)=0.002773, P=0.9583, 3-way ANOVA, open field (center): treh-effect; F(1,34)=3.219, P=0.0817). Neither dox nor trehalose had any significant effects on the distance travelled by the mice on the open field arena (Fig.3.23.D; 3-way ANOVA, dox-effect; F(1,34)=0.0007230, P=0.9787, treh-effect; F(1,34)=0.1792, P=0.6747).

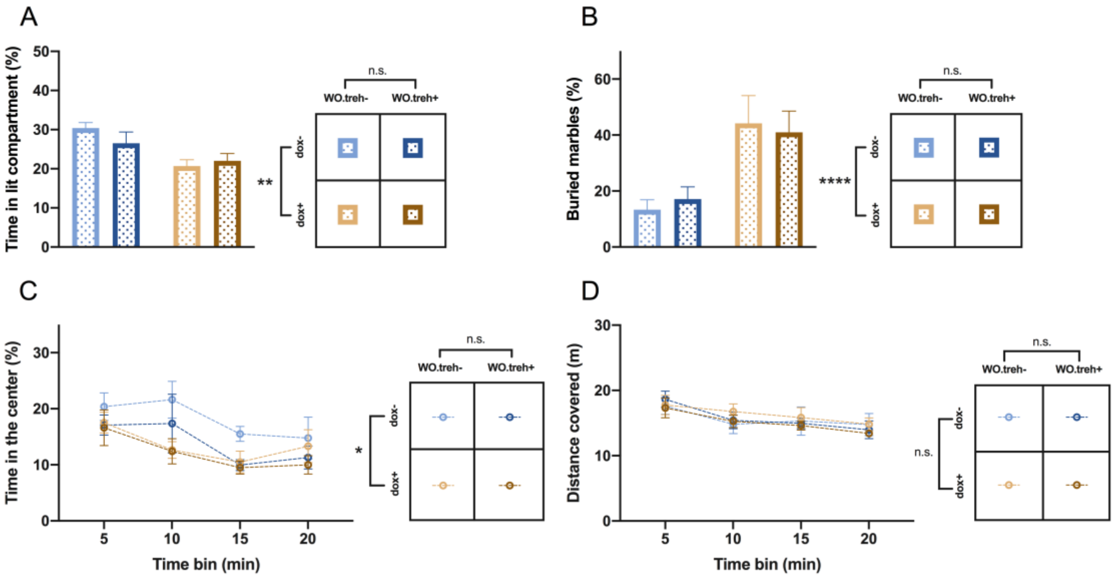

Figure 3.23: Anxiety and locomotion under trehalose treatment in the wash-out
A. *Dox-induction significantly reduced the time mice spent in the lit compartment of the light/dark transition setup after the wash-out. No significant effects were observed for trehalose treatment.* ***B.*** *Dox-induction significantly increased the number of marbles buried during the marble burying task, whereas trehalose treatment did not have any significant effects on the task.* ***C.*** *Dox-induction interfered negatively with the time mice spent in the center of the open field arena. Trehalose supplementation in the wash-out lacked any significant effects for this measure.* ***D.*** *Distance covered measure in the open field arena was not affected either by the dox-induction or the trehalose treatment. Data presented as mean ± S.E.M. *p<0.05, **p<0.01, ****p<0.0001. For details on ANOVA results see* ***Table S14****.*

When the mice have been subjected to the trace fear conditioning paradigm (N(dox-.WOtreh-)=10, N(dox-.WOtreh+)=9, N(dox+.WOtreh-)=10, N(dox+.WOtreh+)=9) their freezing levels in the training session were not found to be affected by dox-induction or trehalose supplementation (Fig.3.24.A; 2-way ANOVA, pre: dox-effect; F(1,34)=1.960, P=0.1706, treh-effect; F(1,34)=0.08704, P=0.7698, post: dox-effect; F(1,34)=0.1932, P=0.6630, treh-effect; F(1,34)=0.05361, P=0.8183). However, in the context retrieval dox has increased the freezing levels of the mice both in the shock context and in the neutral context, whereas no significant effects were observed associated with trehalose (Fig.3.24.B; 2-way

ANOVA, shock: dox-effect; F(1,34)=9.333, P=0.0044, treh-effect; F(1,34)=0.5415, P=0.4669, neutral: dox-effect; F(1,34)=7.098, P=0.0117, treh-effect; F(1,34)=0.04200, P=0.8388). The freezing levels of the mice remained unaffected both by doxycycline and by trehalose in the cue retrieval session (Fig.3.24.C; 2-way ANOVA, CS+: dox-effect; F(1,34)=0.1498, P=0.7011, treh-effect; F(1,34)=0.08921, P=0.7670, trace: dox-effect; F(1,34)=2.874, P=0.0992, treh-effect; F(1,34)=1.939, P=0.1728).

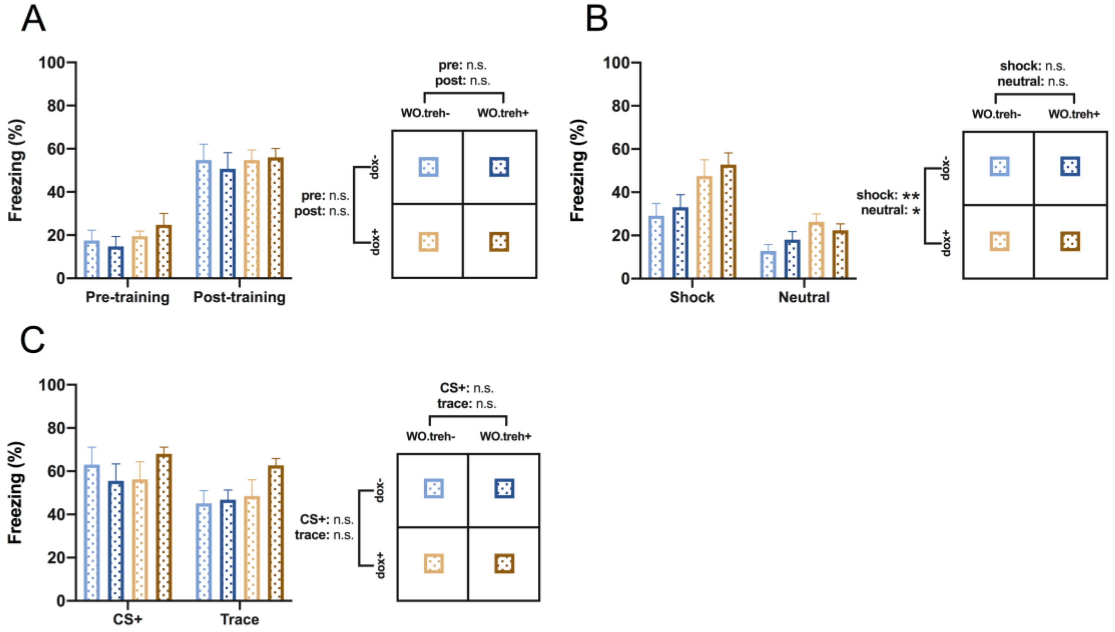

Figure 3.24: Associative learning and memory under trehalose treatment in the wash-out
A. *No significant effects were observed either in the pre-training or in the post-training freezing levels for any of the treatments as recorded during the training session* ***B.*** *During the context retrieval session, dox-induction significantly increased the freezing levels of the mice both in the shock context and in a neutral context, whereas trehalose treatment had no effect on the freezing levels in either of the contexts.* ***C.*** *In the cue retrieval session, no significant effects on the freezing levels were observed either to the conditioned tone (CS+) or during the trace interval. Data presented as mean ± S.E.M. *p<0.05, **p<0.01. For details on ANOVA results see* ***Table S15****.*

Sensorimotor deficits have been identified with the 24 weeks dox-induced 90xCGG mice (see Fig.3.1.D). These 90xCGG.24we mice are age-matched with the mice that constitute the control study of trehalose supplementation in the wash-out. In order to investigate any potential effects of a shorter 12 weeks of dox-induction on sensorimotor gating with mice that are further aged, an additional acoustic startle test was performed (N(dox-.WOtreh-)=10, N(dox-.WOtreh+)=9, N(dox+.WOtreh-)=10, N(dox+.WOtreh+)=9). This test also allows for evaluation of any potential effects of trehalose supplementation in the wash-out. When basal startle responses of the mice to single acoustic stimuli with various SPLs were analyzed, no significant effects of either dox or trehalose were observed (Fig.3.25.A; 3-way ANOVA, dox-effect; F(1,34)=0.04534, P=0.8326, treh-effect; F(1,34)=0.4762, P=0.4948). Neither dox nor trehalose supplementation in the wash-out had significant general effects on the prepulse inhibition (Fig.3.25.B; 3-way ANOVA, dox-effect; F(1,34)=0.1825, P=0.6719, treh-effect; F(1,34)=0.2694, P=0.6071).

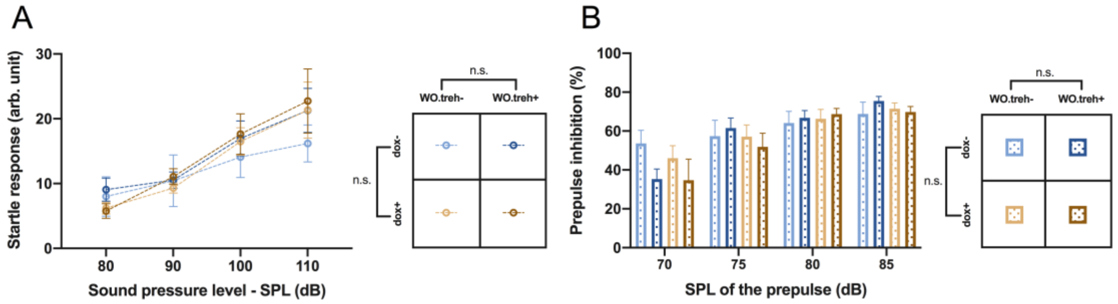

Figure 3.25: Sensorimotor behavior after trehalose supplementation in the wash-out
A. *Baseline startle responses were unaffected either by dox-induction or trehalose treatment in the wash-out.* ***B.*** *No significant effects of either dox-induction or trehalose-treatment were identified on the prepulse inhibition levels. Data presented as mean ± S.E.M. For details on ANOVA results see* ***Table S16****.*

3.2.1.2 Control of genotype independent effects of doxycycline and trehalose

RATIONALE - The genotype independent effects of both dox and trehalose were investigated under this control study with black6 (BL6) mice. Dox by definition induces transgene expression in the PrP.90xCGG model and trehalose exert effects both at the molecular and behavioral level. In order to confirm the authenticity of these effects, BL6 mice were treated either with dox or with trehalose adhering to the time schedule, when both dox and trehalose had effects (Fig.3.26.A). Control group (ctrl) was not treated either with dox or trehalose. Under this investigation BL6 mice were subjected to the behavioral tasks that were previously affected either by dox or trehalose.

First, motor performance of BL6 mice was evaluated with the rotarod rest (N(ctrl)=8, N(treh)=9, N(dox)=8). During the training session no differences were observed in the latencies to fall off the rod between the groups (Fig.3.26.B; 2-way RM ANOVA, treatment-effect; F(2,22)=1.138, P=0.3385). When the motor performance of three groups of BL6 mice were evaluated with the constant speed rotarod test no differences were observed between the groups (Fig.3.26.C; 2-way RM ANOVA, treatment-effect; F(2,22)=1.129, P=0.3413). On the accelerating rod, the groups did not differ from each other in their latency to fall off the rod (Fig.3.26.D; Kruskal-Wallis test, K-W stat.=1.711, P=0.4250). The body weights of the mice were also not different between groups (Fig.3.26.E; 1-way ANOVA, treatment-effect; F(2,22)=2.535, P=0.1021).

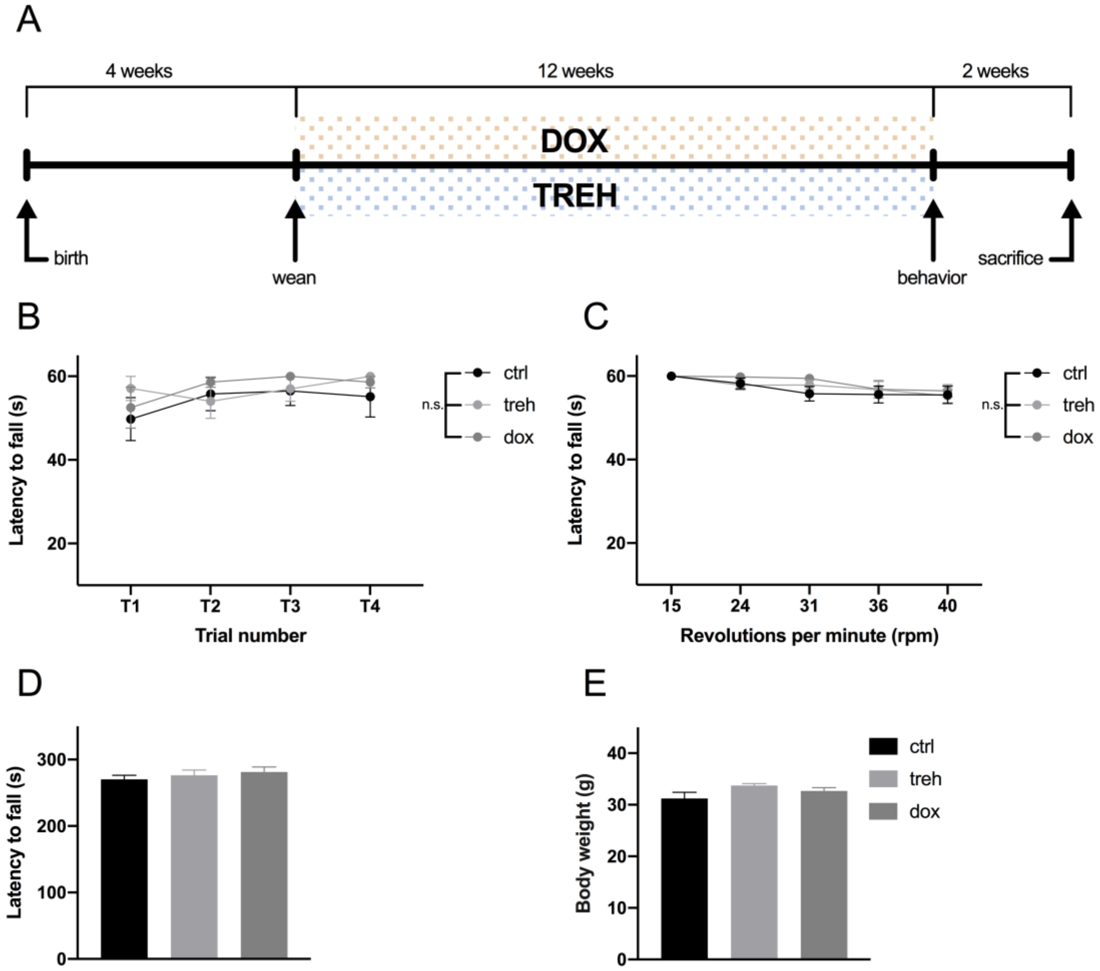

Figure 3.26: Dox and trehalose supplementation schedule for BL6-mice and motor performance ***A.*** *Timeline showing the dox or trehalose supplementation schedule used in order to control for potential genotype-independent effects of dox and trehalose in vivo.* ***B.*** *On a rotating rod at 15-rpm during a 1-day, 4-trial training session no differences were observed between the dox+, treh+ and control mice* ***C.*** *During the constant speed rotarod test all three groups displayed comparable latencies to fall off the rod when tested on a rotating rod at various speeds.* ***D.*** *No differences were observed between latencies to fall off the rod for any of the three groups of mice when they are tested in a speed ramp setting during the accelerating rotarod test.* ***E.*** *No differences were observed in the body weights of the dox+, treh+ and control mice. Data presented as mean ± S.E.M. For details on 2-way ANOVA results see* ***Table S17****.*

Next, BL6 mice were subjected to anxiety sensitive tests (N(ctrl)=8, N(treh)=9, N(dox)=8). In the light/dark transition test (Fig.3.27.A; 1-way ANOVA, treatment-effect; F(2,22)=1.599, P=0.2247) and marble burying test (Fig.3.27.B; 1-way ANOVA, treatment-effect; F(2,22)=1.851, P=0.1807) no differences were observed between groups. In the open field arena, no differences were observed between groups in the time mice spent in the center (Fig.3.27.C; 2-way RM ANOVA, treatment-effect; F(2,22)=1.445, P=0.2572). The locomotion parameter “distance covered in the arena” was also evaluated as differences here may interfere with “the time spent in the center” parameter. No differences were observed between groups in the distances they traveled in the open field arena (Fig.3.27.D; 2-way RM ANOVA, treatment-effect; F(2,22)=1.204, P=0.3189).

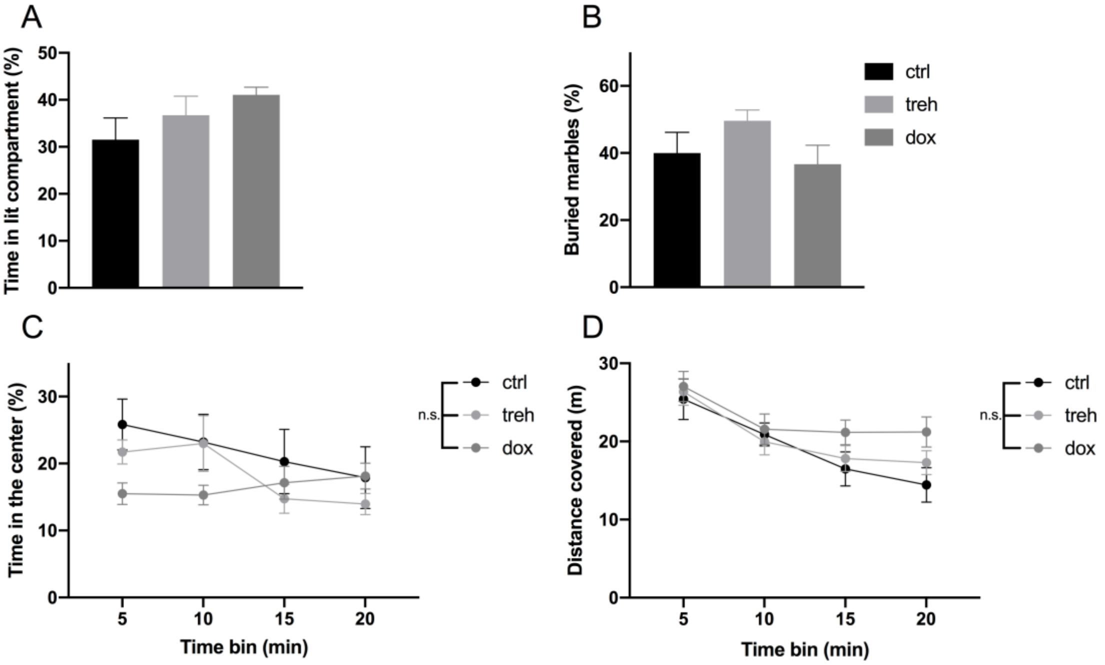

Figure 3.27: Anxiety and locomotion in BL6-mice
A. *No differences were observed between dox+, treh+ and control mice in the time they spent in the lit compartment of the light/dark transition setup.* ***B.*** *No differences were observed between any of the three groups in the number of marbles buried during the marble burying task.* ***C.*** *No differences were observed in their time spent in the center of the open field arena between any of the three groups of mice.* ***D.*** *No differences in the distance the mice covered in the open field arena were observed between dox+, treh+ and control groups. Data presented as mean ± S.E.M. For details on 2-way ANOVA results see* ***Table S18****.*

Lastly, BL6 mice were subjected to the trace fear conditioning paradigm (N(ctrl)=8, N(treh)=9, N(dox)=8). The freezing levels of the mice did not differ between groups before or after the training session (Fig.3.28.A; pre: Kruskal-Wallis test, K-W stat.=2.678, P=0.2621, post: 1-way ANOVA, treatment-effect; F(2,22)=1.456, P=0.2548). In the context retrievals, freezing levels were not different between the groups in neither of the contexts (Fig.3.28.B; Kruskal-Wallis test, shock: K-W stat.=1.196, P=0.5499, neutral: K-W stat.=2.981, P=0.2252). In the cue retrieval session, the groups did not differ from each other in the freezing levels to the CS+ and during the trace interval (Fig.3.28.C; CS+: 1-way ANOVA, treatment-effect; F(2,22)=0.7617, P=0.4788, trace: Kruskal-Wallis test, K-W stat.=0.9193, P=0.6315).

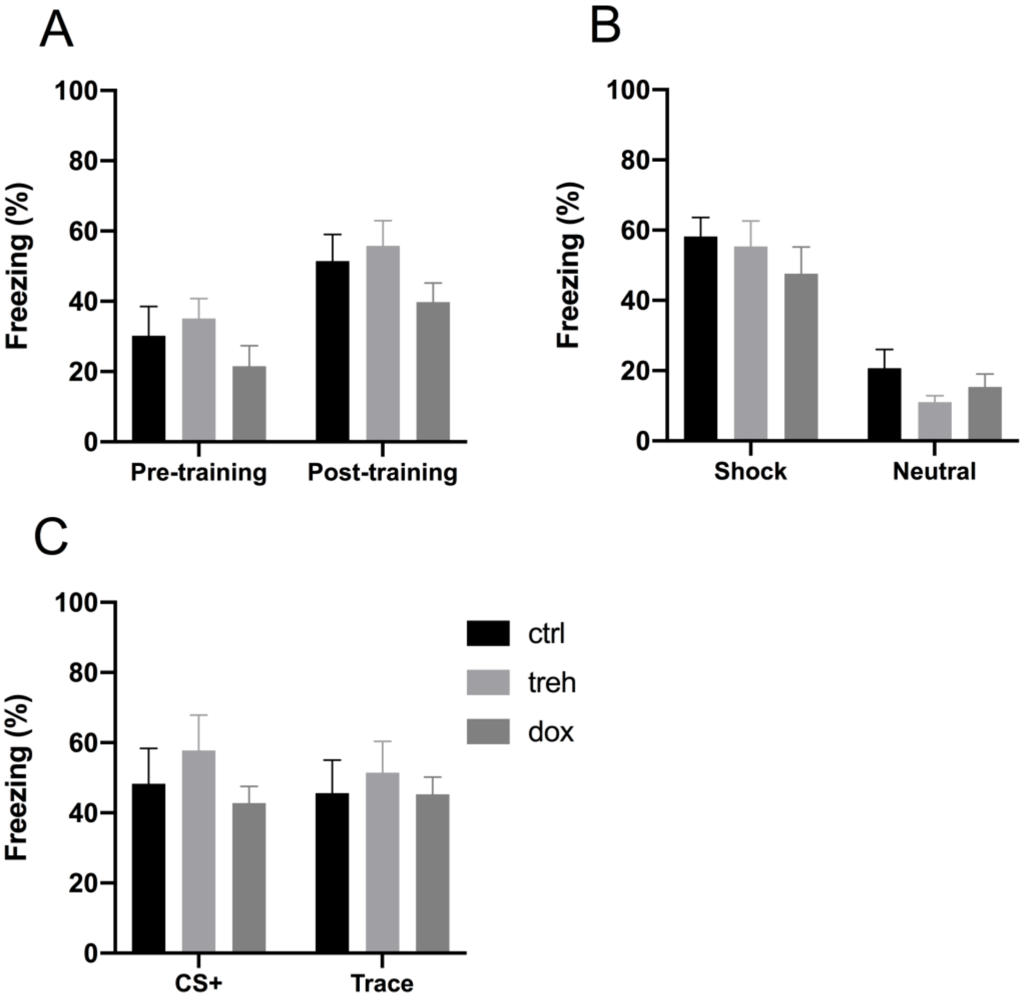

Figure 3.28: Associative learning and memory in BL6-mice
A. *No differences were observed either in the pre-training or in the post-training freezing levels between dox+, treh+ and control mice as recorded during the training session* ***B.*** *During the context retrieval session, the freezing levels of all three groups of mice remained comparable both in the shock context and in a neutral context.* ***C.*** *In the cue retrieval session, no differences in the freezing levels of the dox+, treh+ and control groups were observed either to the conditioned tone (CS+) or during the trace interval. Data presented as mean ± S.E.M.*

3.2.2 Gene therapy by antisense oligonucleotides

RATIONALE - Antisense oligonucleotides (ASOs) are small single stranded DNA fragments designed specifically to target mRNA and inactivate it. Here, the viability of an 11 nucleotide long ASO consisted of antisense CCG sequences that can bind mRNA containing expanded CGG stretches (CGG^{exp}) tested as an *in vivo* therapeutic strategy. This ASO has been shown to reduce the biosynthesis of FMRpolyG and decrease the number of inclusions *in vitro*. The ASO is highly stable with low toxicity and can move across the plasma membrane and enter the cells even in the absence of a carrier (data not shown; unpublished collaboration data obtained by M. Derbis; K. Sobczak's group, AMU, Poznań, Poland). In order to evaluate the *in* *vivo* therapeutic potential of the ASO the 12 week dox-induction schedule is used starting at weaning. This schedule produces a motor phenotype and FMRpolyG foci in the cerebellum.

A 4+4+4 schedule has been adopted for the ASO delivery to dox-induced PrP.90xCGG mice (Fig.3.29.A). Under this schedule, the ASO has been delivered for four weeks into the cerebrospinal fluid via intracerebroventricular infusion at the right lateral ventricle. A continuous infusion was made possible by an osmotic pump that has been implanted subcutaneously (Fig.3.29.B). At the end of the ASO treatment FMRpolyG-positive intranuclear inclusions were identified in the cerebellum lobule X (Fig.3.29.C) but the percent number of the nuclei with FMRpolyG focus was significantly reduced in the aso-infused group as compared to controls that were infused with a saline solution (Fig.3.29.D; N(aso-)=6, N(aso+)=7, Student's t-test, t=2.838, df=11, P=0.0161). Moreover, the size of the FMRpolyG foci was decreased in the aso-treated mice when compared to untreated mice (Fig.3.29.E; N(aso-)=6, N(aso+)=7, Student's t-test, t=2.896, df=11, P=0.0146).

The motor performance under aso-treatment was assessed in a rotarod task (N(aso-)=6, N(aso+)=7). During the training session, on a rotating rod at slow speed no differences were observed in the latencies to fall off the rod between the groups (Fig.3.30.A; 2-way RM ANOVA, aso-effect; F(1,11)=1.117, P=0.3131). During the constant speed rotarod test, however, aso-infused group showed higher latencies to fall of the rod as compared to aso- controls (Fig.3.30.B; 2-way RM ANOVA, aso-effect; F(1,11)=5.994, P=0.0323). Also, on the accelerating rod aso+ group remained on the rotated rod longer than the aso- group (Fig.3.30.C; Student's t-test, t=5.103, df=11, P=0.0003). No changes in the body weight were observed between the aso-treated group and the aso- control group (Fig.3.30.D; Student's t-test, t=1.163, df=11, P=0.2693).

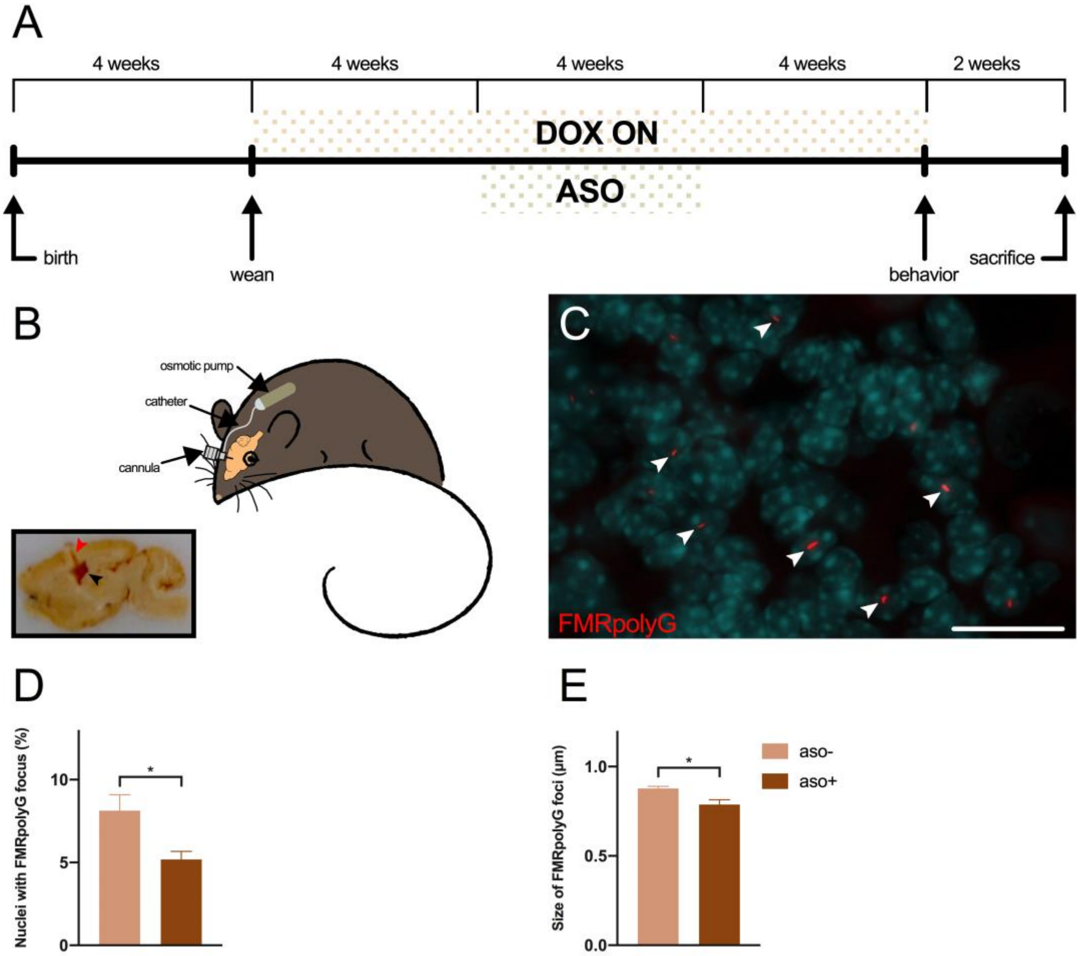

Figure 3.29: Antisense oligonucleotide intervention schedule and recovery in the inclusion load upon treatment

A. *Timeline showing the dox-induction and antisense oligonucleotide (ASO) intervention schedule used in order to investigate the potential of antisense gene therapy in vivo.* ***B.*** *Graphical representation describing the intracerebroventricular infusion method of the ASO via an osmotic pump implanted subcutaneously. Bottom-left: Photograph showing the cannula placement on post-mortem brain tissue. Red arrowhead: cannula entry site, black arrowhead: lateral ventricle.* ***C.*** *High magnification photomicrograph showing the FMRpolyG foci colocalizing with various nuclei within the granular layer of the cerebellum lobule X. Red: FMRpolyG, blue: DAPI. White arrowheads: FMRpolyG foci (not all foci marked). Scale bar indicates 20 µm.* ***D.*** *Quantified from the granular layer of cerebellum lobule X, aso-treated mice had significantly smaller number of nuclei with FMRpolyG focus as compared to aso- controls.* ***E.*** *The FMRpolyG foci were significantly smaller in size with the aso-treated group as compared to aso- group. Data presented as mean ± S.E.M. *p<0.05.*

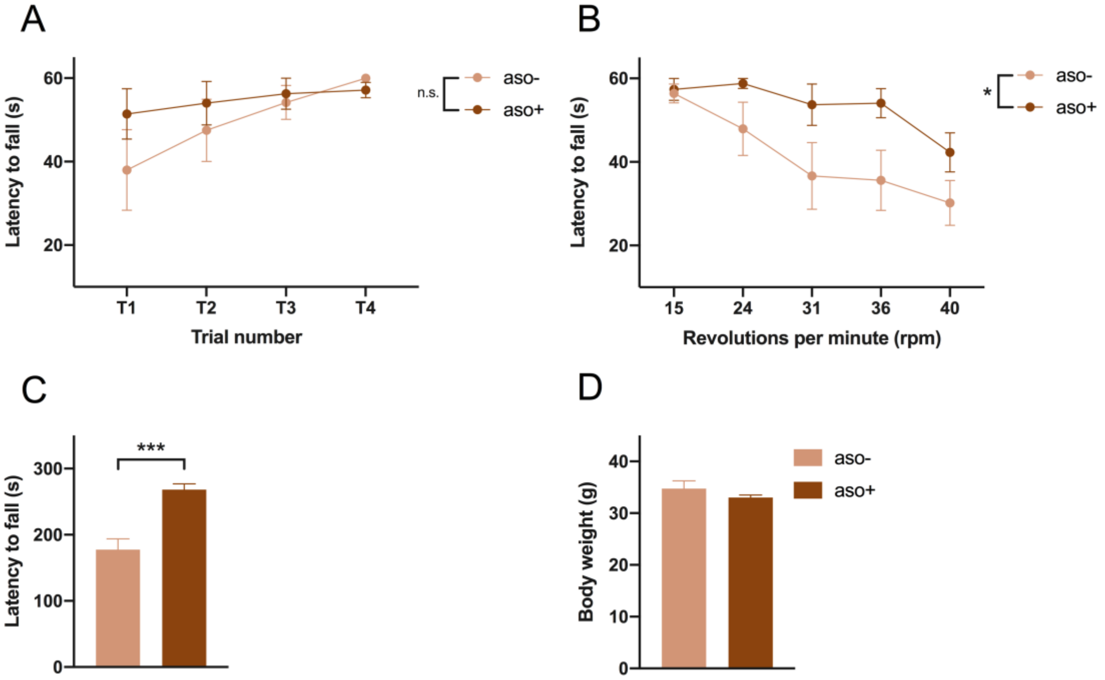

Figure 3.30: Recovery in the motor performance upon antisense oligonucleotide treatment
A. *On a rotating rod at 15-rpm during a 1-day, 4-trial training session no differences were observed between the aso-infused mice and the aso- controls in their latency to fall off the rod.* ***B.*** *During the constant speed rotarod test aso-treated mice displayed significantly higher latency to fall off the rod as compared to aso- controls when tested on a rotating rod at various speeds.* ***C.*** *Aso-infused mice showed higher latency to fall off the rod as compared to their aso- counterparts when they are tested in a speed ramp setting during the accelerating rotarod test.* ***D.*** *No differences were observed between the body weights of the aso-infused mice and aso- mice. Data presented as mean ± S.E.M. *p<0.05, ***p<0.001. For details on ANOVA results see* ***Table S19****.*

Next, a series of correlation analyses have been performed to see if the number of inclusions and their size predict the performance on accelerating rotarod (N(aso-)=6, N(aso+)=7). When the latencies to fall off the rod of each mouse were paired with the percent number of nuclei they have with a FMRpolyG focus in the cerebellum lobule X, a significant negative correlation was observed (Fig.3.31.A; Pearson correlation, r=-0.6301, P=0.0210). The same type of correlation was also present when the motor performance was paired with intranuclear inclusions size (Fig.3.31.B; Pearson correlation, r=-0.5707, P=0.0417). The percent number of nuclei with inclusions also correlated significantly with the size of the inclusions (Fig.3.31.C; Pearson correlation, r=0.6121, P=0.0262).

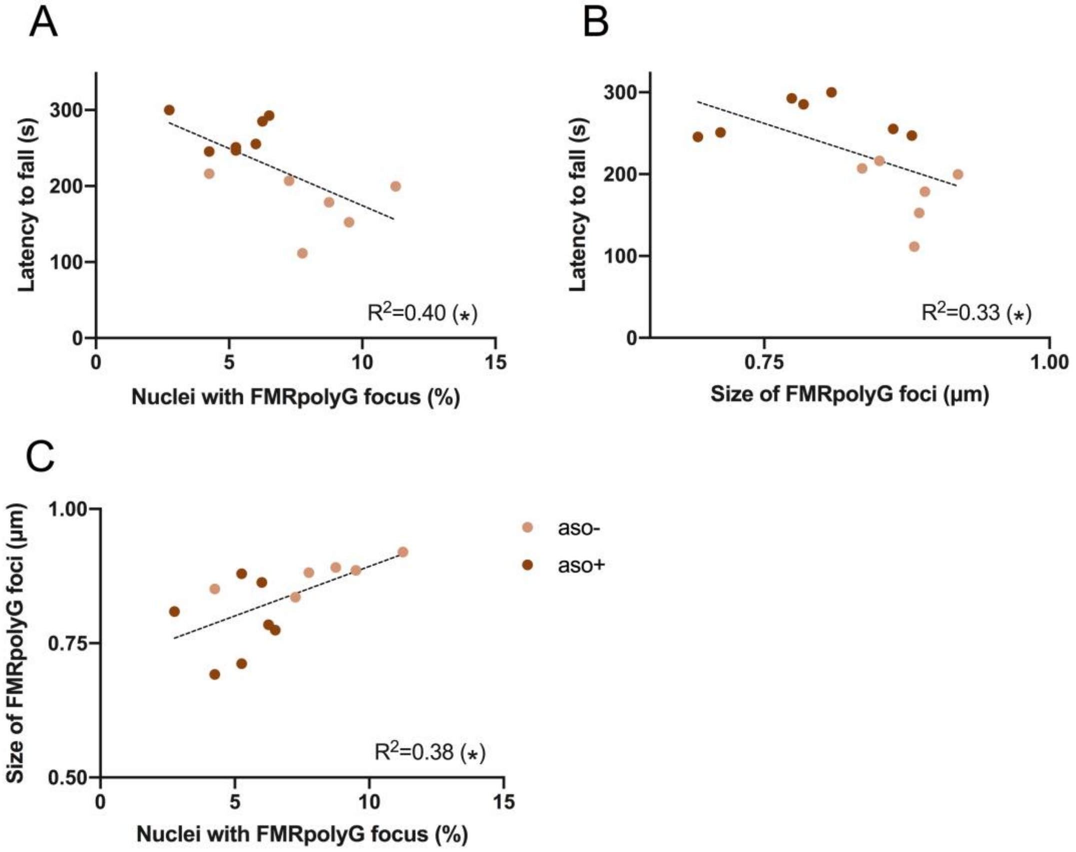

Figure 3.31: Motor performance correlates with the inclusion load in the lobule X
Statistically significant negative correlation was identified between the latencies to fall off the rod of individual mice during the accelerating rotarod task and ***A.*** *their number of nuclei with FMRpolyG focus in the lobule X,* ***B.*** *the size of the FMRpolyG foci.* ***C.*** *Statistically significant positive correlation was identified between the number of nuclei with FMRpolyG focus in the lobule X and the size of these FMRpolyG foci. Data presented as individual values. *p<0.05.*

The potential effects of the ASO have also been tested in the other behavior domains, where significant effect have been previously observed under various dox-induction schedules. Gait parameters under aso-treatment have been quantified from paw prints of the mice (N(aso-)=6, N(aso+)=8). Of the six gait parameters analyzed, none of them were found to be different between the aso-infused mice and their saline-infused counterparts. No changes were observed in the parameters uniformity of step alternation (Fig.3.32.A; Student's t-test, t=0.5786, df=12, P=0.5735), forepaw width (Fig.3.32.B; Student's t-test, t=1.463, df=12, 0.1690), hind paw width (Fig.3.32.C; Mann-Whitney test, U=22.50, P=0.8765), stride length (Fig.3.32.D; Student's t-test, t=0.7696, df=12, P=0.4564), overlap symmetry (Fig.3.32.E; Student's t-test, t=0.6556, df=12, P=0.5245) or alternation coefficient (Fig.3.32.F; Student's t-test, t=0.3756, df=12, P=0.7138).

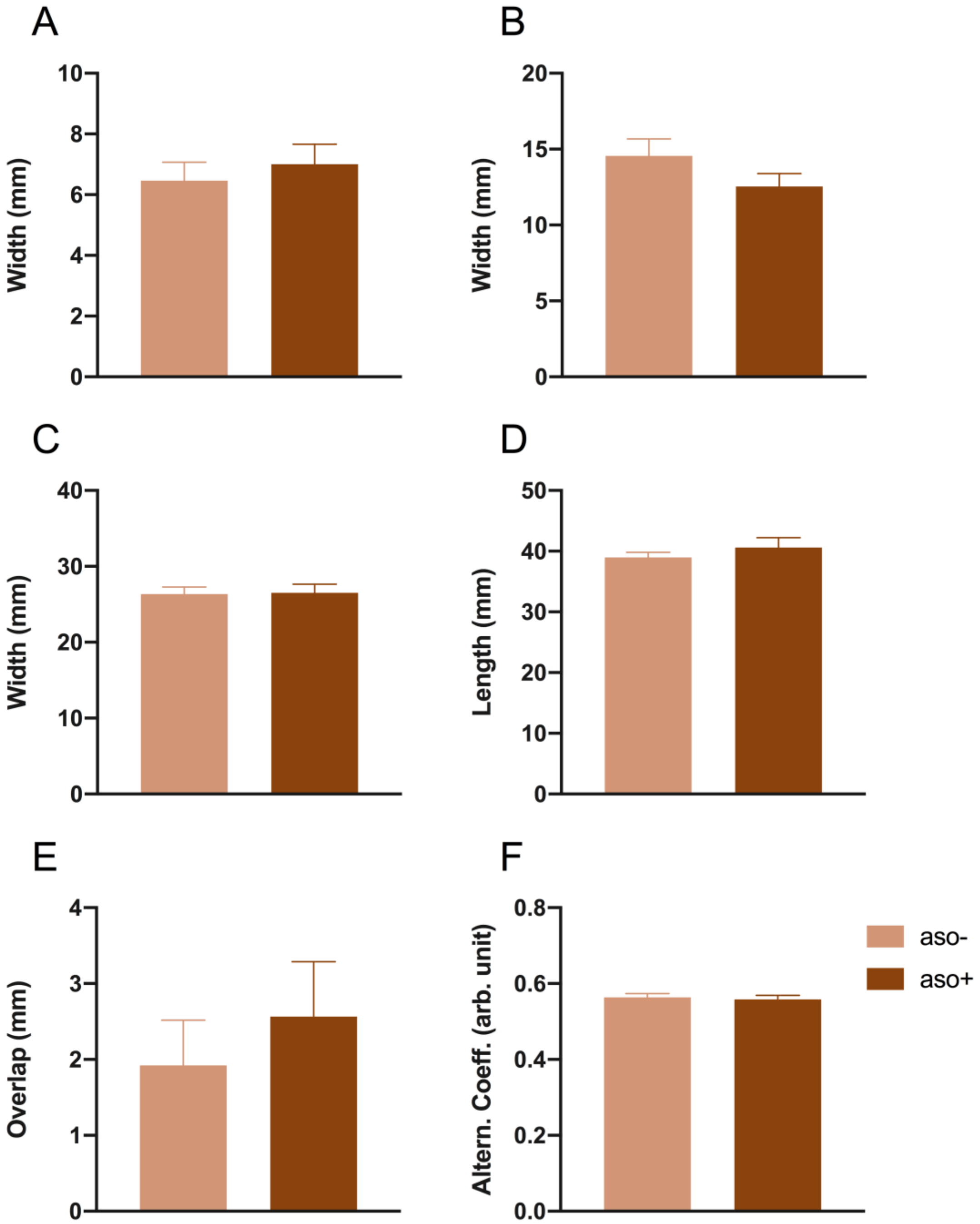

Figure 3.32: Gait parameters under antisense oligonucleotide treatment
No differences were observed between aso-infused group and aso- controls in the measures ***A.*** *uniformity of step alternation,* ***B****. forepaw width,* ***C.*** *hind paw width,* ***D.*** *stride length,* ***E.*** *overlap symmetry,* ***F.*** *alternation coefficient. Data presented as mean ± S.E.M.*

Mice were then subjected to three different anxiety sensitive tests including an open field test, for which a read-out on locomotor behavior is also reported (N(aso-)=6, N(aso+)=8). No differences were observed between the aso+ group and the saline-infused controls in the light/dark transition test (Fig.3.33.A; Student's t-test, t=0.4666, df=12, P=0.6491), in the marble burying test (Fig.3.33.B; Student's t-test, t=1.303, df=12, P=0.2171) or in the open field for the parameter "the time spent in the center" (Fig.3.33.C; 2-way RM ANOVA, aso-effect; F(1,12)=0.2341, P=0.6372). The distance mice covered in the open field arena was not different between groups (Fig.3.33.D; 2-way RM ANOVA, aso-effect; F(1,12)=1.853, P=0.1985).

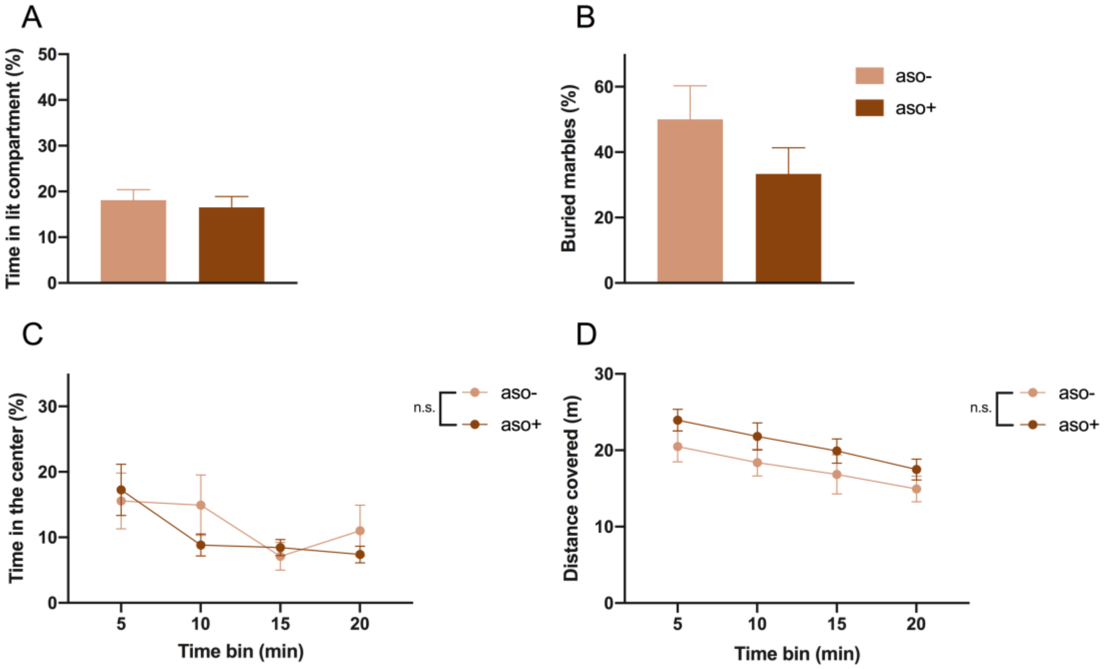

Figure 3.33: Anxiety and locomotion under antisense oligonucleotide treatment
A. *No differences were observed between aso-treated mice and their aso- counterparts in the time spent in the lit compartment of the light/dark transition setup.* ***B.*** *No differences were observed between aso+ group and aso- controls in the number of marbles buried during the marble burying task.* ***C.*** *No differences were observed in the time spent in the center of the open field arena between aso+ and aso- mice.* ***D.*** *No differences in the distance covered in the open field arena were observed between aso+ and aso- mice. Data presented as mean ± S.E.M. For details on ANOVA results see* ***Table S20****.*

Under the trace fear conditioning paradigm (N(aso-)=6, N(aso+)=8), no differences were observed between the aso-treated group and the saline-infused controls during the training session (Fig.3.34.A; pre: Mann-Whitney test, U=20, P=0.6324, post: Student's t-test, t=1.030, df=12, P=0.3235). The freezing levels were not different between the groups also in the context retrievals (Fig.3.34.B; shock: Student's t-test, t=0.08342, df=12, P=0.9349, neutral: Mann-Whitney test, U=16, P=0.3290). In the cue retrieval session, the freezing levels either to the conditioned cue or during the trace interval were not different between the groups (Fig.3.34.C; Mann-Whitney test, CS+: U=18.50, P=0.5085, trace: U=14, P=0.2171).

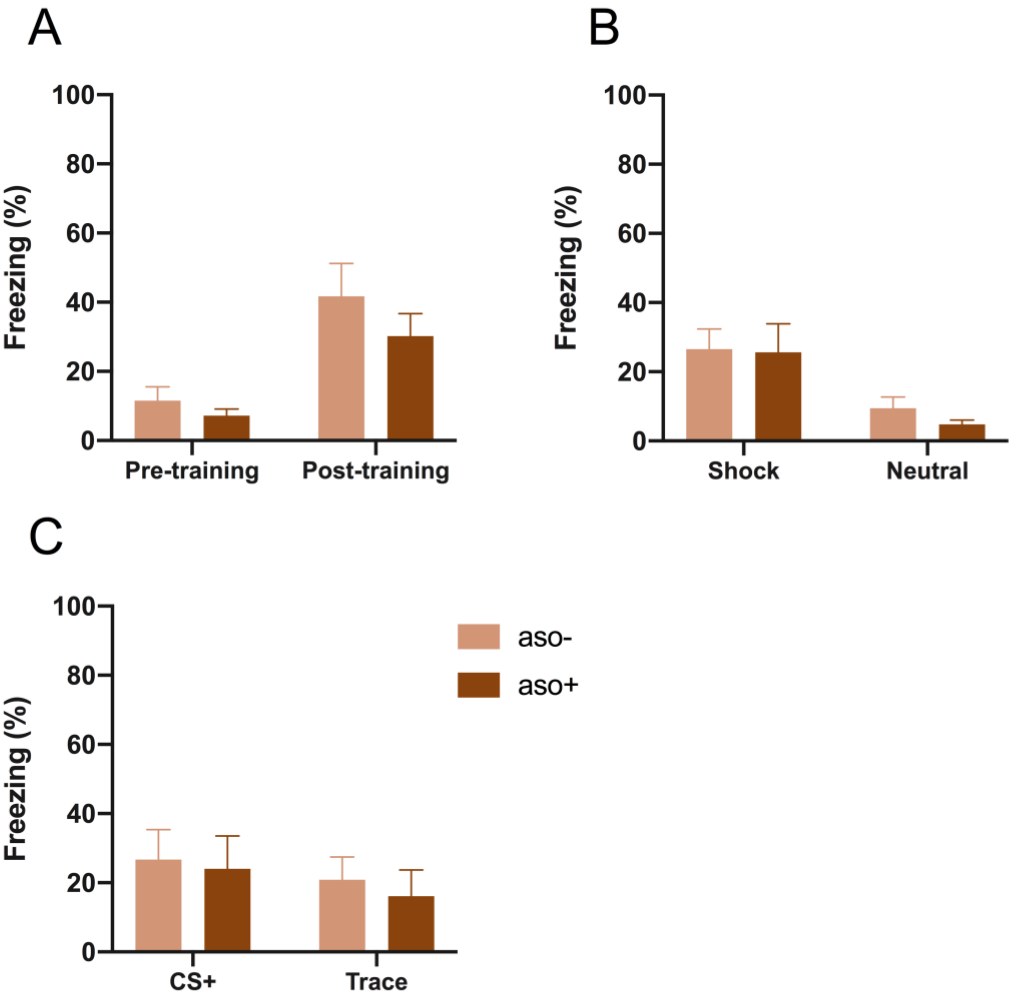

Figure 3.34: Associative learning and memory under antisense oligonucleotide treatment
A. *No differences were observed either in the pre-training or in the post-training freezing levels between the aso+ and aso- group as recorded during the training session* ***B.*** *During the context retrieval session, the freezing levels of the aso+ mice remained unaltered as compared to aso- control mice both in the shock context and in a neutral context.* ***C.*** *In the cue retrieval session, no differences in the freezing levels of the aso+ mice were observed either to the conditioned tone (CS+) or during the trace interval as compared to aso- controls. Data presented as mean ± S.E.M.*

4 Discussion

Triplet expansions in the 5’ UTR of the *fmr1* gene are responsible for four distinct incurable disorders with intergenerational implications. The premutation (PM) disorders affect not only the carrier individuals but entire families and causes hardship especially to PM carrier mothers, who with very high probability raising children with FXS. FXTAS is a devastating neurodegenerative disorder of the PM affecting the older population. Without a viable cure in sight, model organisms that better replicate FXTAS features are needed to understand the pathology and progression of the disorder in order to develop viable treatment strategies and test their success in the preclinical setting. Rather than treating the individual symptoms, intervening with the core pathomechanisms of the disorder has more potential towards developing a universal therapy for FXTAS. Any successful intervention strategy developed with this aim should also have high applicability for FXAND and FXPOI.

4.1 The late phenotypes of FXTAS

In a previous study, the PrP.90xCGG model has been behaviorally phenotyped and major features of FXTAS have been identified under the common 12-week induction schedule but some key aspects of FXTAS have not been replicated (Castro et al. 2017). Given the progressive nature of the disorder, this time, PrP.90xCGG model was subjected to a longer 24-week induction schedule in order to investigate phenotypes that may become apparent at a later time point. Indeed, a sensorimotor phenotype that is highly specific to the longer treatment duration and the expression of CGG^{exp} was identified in the form of PPI deficits (see Fig.3.1.) Studies with the CGG^{exp}-KI model showed that deficits in PPI occur also only at a later age (Renoux et al. 2014). Surely, deficits PPI deficits have been described in FXTAS patients (Schneider et al. 2012) and PD patients with decreased striatal dopamine transporter levels (Zoetmulder et al. 2014). Although Parkinsonism is seen with a large fraction of FXTAS patients, sensorimotor gating impairments has not been investigated within the context of nigrostriatal degeneration and dopamine signaling.

The investigation of other Parkinsonism features in the PrP.90xCGG mice at this later time-point revealed that they also present with a decreased stride-length (see Fig.3.3.), a typical Parkinsonism feature observed in various mouse models of PD and also with PD and FXTAS patients (Hall et al. 2009), (Taylor, Greene, and Miller 2010). Another typical feature is bradykinesia, which can be measured in animal models by the distance mice travel during a specific time interval in an open field arena. When the dox-induced PrP.90xCGG animals were tested for this parameter under the 24-week induction schedule, they did not show any differences that distinguish them from controls. Unfortunately, some mouse models of PD also fail to replicate this feature (Taylor, Greene, and Miller 2010). Perhaps, the distance mice travel in the open field arena is not a very sensitive measure to detect bradykinesia in a complex disease model because it may be easily affected by factors that may be associated with the environment or by features of the disease other than bradykinesia alone. As a control measure, the time the mice spent in the center of the arena was also quantified in order to get an impression on whether or not the mice explore the arena equally under red light conditions. Although this measure was not statistically significant between dox+ and dox- PrP.90xCGG mice, there may be small factors that create the trend seen in this data and influences the distance mice travel. An analysis based on live gait tracking might be more suitable to assess bradykinesia. An alternative can be the catwalk method that is the automated version of the gait analysis performed here from the pawprints.

In order to investigate the PPI deficits seen at this time-point in relation to Parkinsonism and nigrostriatal degeneration, the dopamine transporter (DAT) levels have been quantified from the striatal sections of the PrP.90xCGG animals and been found to be severely reduced (see Fig.3.4.). Striatal DAT levels have been reported to be low in PD patients as well as in some FXTAS patients (Kagi, Bhatia, and Tolosa 2010), (De Pablo-Fernandez et al. 2015). One study correlates the decreased levels of striatal DAT with decreased PPI in PD patients (Zoetmulder et al. 2014). However, a decrease in striatal DAT levels can have two distinct effects on striatal dopamine depending on the underlying mechanism. DAT in striatum is presynaptic and functions in the reuptake of released dopamine from the synaptic cleft back into the presynapse. Therefore, a decrease in DAT levels can induce a hyperdopaminergic state if there are no other functional abnormalities with the presynaptic dopaminergic neuron residing in the substantia nigra pars compacta (SNpc). However, PD is associated with dopamine depletion caused by the degeneration of the SNpc neurons, whereas hyperdopaminergic states are usually linked to Schizophrenia (Weinstein et al. 2017). Therefore, it is necessary to look at the dopaminergic neurons in the SNpc. These neurons express tyrosine hydroxylase (Th), an essential enzyme that functions in the synthesis of dopamine (Daubner, Le, and Wang 2011).

The quantification of the Th level in the SNpc revealed that the decrease in striatal DAT might actually be caused by a dysfunction of the SNpc neurons that produce decreased levels of Th (see Fig.3.5.). Moreover, a decrease in the total number of Th+ cells have been observed that suggest a degenerative process leading to Th+ cell death in the SNpc (see Fig.3.6.). However, because the Th levels were already low in the SNpc neurons, it is possible that the cell counts based on Th-labeling could not detect some of the dopaminergic neurons that are actually still residing in the SNpc. On the other hand, a decrease was observed in the total nuclei counts in the SNpc suggesting that there has indeed been a certain amount of cell loss in the SNpc. The decrease in the Th counts between dox+ and dox- PrP.90xCGG mice were found to be much more prominent (~30%) than the decrease in the nuclei counts (~7%) in the same region and this can be attributed to the above argument that some of the Th+ neurons might have been omitted from the cell counts due to their very low Th signal. Also, Th+ neurons are the dominant cell population in the SNpc but they are not the only cells in this region. A decrease in the Th+ neuron population will have a smaller impact on the decrease in the total cell population of the SNpc.

Intranuclear inclusions and intracytoplasmic Lewy bodies have been reported to be present in the pigmented neurons of the SNpc for some but not all FXTAS patients (Greco et al. 2002). However, no FMRpolyG-positive inclusions have been encountered in the Th+ neurons of the SNpc of the 24 weeks dox-induced PrP.90xCGG mice (see Fig.3.7.). This raises the question whether or not these neurons express the CGG^{exp}. The expression of the transgene containing the CGG^{exp} is under the control of the PrP promotor in this model and although PrP is expressed throughout the brain in neurons and glia, its expression levels change drastically from one brain structure to another (Hukema et al. 2015). However, a co-staining of Th together with GFP, that is the reporter of the TRE-90CGG transgene expression in the PrP.90xCGG model, revealed a complete colocalization in the SNpc along with occasional GFP+ cells that do not stain positively for Th (see Fig.3.8.). These latter cells may still be dopaminergic neurons with undetectable levels of Th expression or belong to a different cell type in the same region that also express the CGG^{exp} under the control of the PrP promotor.

4.2 Intranuclear inclusions: Toxic or protective?

The evidence suggesting that the Th+ neuron population in the SNpc of the dox-induced PrP.90xCGG mice degenerates without forming inclusions raises the question whether inclusions are toxic or protective in FXTAS. One might argue that the dopaminergic neurons that were already lost until the 24-week time point could have contained inclusions and these inclusions simply cannot be detected anymore because those cells are now dead. This is a possible but highly unlikely scenario because more than two thirds of the Th+ population remains in the SNpc and the odds of not finding a single Th+ cell with an intranuclear inclusion are very low if they indeed form inclusions. A similar observation has also been reported on the cerebellar Purkinje cells of the NIH-mouse. Although they do not form inclusions, Purkinje cell loss has been observed with these mice (Entezam et al. 2007). This points out to a potentially increased vulnerability in certain cell types by the inability to form inclusions.

Whether the inclusions are toxic or incidental or protective is in fact, a very controversial topic in FXTAS research as well as in research encompassing other neurodegenerative diseases. The mechanisms, by which the FXTAS inclusions are formed -RNA gain-of-function and RAN translation- are shown to be toxic to cells in numerous models (Oh et al. 2015), (Hukema et al. 2014), (Todd et al. 2013), (Berman et al. 2014). Therefore, the occurrence of inclusions reflect that a toxic action is taking place in the cell and the magnitude of the toxicity may depend on cell type specific dynamics in relation to the expression of CGG^{exp}. However, it is possible that inclusions are formed as an endogenous reaction of the cell to the production of toxic components. The presence of FMRpolyG in the intranuclear inclusions raises the possibility of the existence of a deliberate mechanism because FMRpolyG is produced in the cytoplasm. This means that it has to be actively translocated into the nucleus. Whether this translocation is incidental and related to the toxic protein gain-of-function of FMRpolyG or indeed a deliberate result of a cellular defense mechanism is an open question.

There is evidence from the neurodegeneration literature supporting the notion that the presence of toxic products outside of the inclusions induces even more toxicity. One study on mutant-huntingtin shows that neurons can die without forming any inclusions and the amount of intracellular expanded-huntingtin in a diffuse state predicts when they would die.

On the other hand, the inclusion body formation was found to be associated with improved survival and decreased levels of the diffuse mutant huntingtin (Arrasate et al. 2004). Moreover, evidence from protein quality control studies suggest that inclusion formation may not be incidental. Misfolded proteins, depending on their ubiquitination state have been found to be purposefully sorted to two distinct cellular compartments known as juxtanuclear and perivacuolar compartments (Kaganovich, Kopito, and Frydman 2008). However, the above arguments do not imply that cells that form inclusions would be protected.

4.3 A potential FXAND model

The early dox-induction schedule captured a pre-motor era of the PM and allowed for the investigation of the phenotypes relevant to FXAND. The rotarod protocol has been performed with exactly the same standards of the previously published phenotyping study of the PrP.90xCGG model to ensure compatibility (Castro et al. 2017). Despite applying the same dox-induction duration, motor deficits were not yet apparent (see Fig.3.9.). However, an anxiety-like behavior has been observed from the light-dark transition paradigm (see Fig.3.10.), suggesting that anxiety precedes the motor phenotype when previously used standards for the phenotyping of the PrP.90xCGG model have been applied. If intervened in this pre-motor era of the PM by introducing a period without transgene expression of 12 weeks (wash-out), the occurrence of the inclusions can be selectively reversed in the DG and BLA but not in CA3 or in cerebellum lobule X (see Fig.3.11.). This was accompanied by a normalization of the initially observed anxiogenic behavior. DG and BLA are structures with well-established relation to anxiety (Rau et al. 2015), (Engin et al. 2016). Therefore, potential physiological changes in these regions were evaluated in relation to the reduction in the inclusion load and normalization of the behavior phenotype.

Slice electrophysiology experiments have been first performed from the general structure of lateral amygdala (LA) that harbors BLA (see Fig.3.12.). An increase in the excitability was recorded from LA, an observation that can explain the anxiety-like behavior of the dox-induced PrP.90xCGG mice in the light-dark transition test. Hyperexcited BLA is associated with anxiety-related disorders, such as post-traumatic stress disorder (PTSD) (Sharp 2017). The hyperexcited state of the LA in the PrP.90xCGG mice has then recovered after the wash-out, coinciding with the normalization of the anxiogenic behavior and reduction of the inclusion pathology. Long term potentiation (LTP) as a measure of plasticity has also been evaluated in LA. LTP is considered as a mechanism involved for creation, storage and retrieval of memories via long-term changes in the synaptic strength associated with hippocampus and amygdala. LTP in the LA is believed to be involved in generation fearful memories with an established link to the fear-conditioning paradigm (Sigurdsson et al. 2007). However, no changes in the LTP were observed either before or after the wash-out in LA.

DG is the other region, where a recovery in the inclusion load was observed following the wash-out phase. In relation to the role of DG on anxiogenic behavior, slice electrophysiology experiments have also been performed from this structure (see Fig.3.13.). Overall, no changes in the LTP were detected either before or after wash-out between the dox- and dox+ mice. Nevertheless, there was an increase in the early-phase LTP only after the dox-induction and not after the wash-out. However, this observation might not reflect a well-described LTP-related phenotype (i.e. learning and memory). The increase in the early-phase LTP may in fact be related to the experimentally applied high frequency stimulation (HFS) in order to induce LTP. The applied HFS initially induces a short-term potentiation (STP) that is followed by generation of LTP that lasts up to 2 hours. Therefore, STP has been long considered to be a biproduct of LTP induction (Volianskis and Jensen 2003). More recently, STP and LTP have been linked to differential recruitment of distinct subtypes of NMDA receptors to the postsynapse indicating that STP might be a process separate from LTP. Unlike LTP, the role of STP in synaptic encoding or the functional implications of changes related to STP are largely unknown (Volianskis et al. 2013). On the other hand, a decrease in excitability has been observed in the DG following the dox-induction that like every other parameter, also normalized after the wash-out. However, decreased excitability in the DG does not explain the heightened anxiety-like behavior observed in the light-dark transition test. According to the available literature, increased inhibition of the DG is associated with anxiolysis (Engin et al. 2016) and anxiety drugs decrease the its excitability (Lempel et al. 2017).

The contradictory result obtained from the investigation of DG physiology in relation to anxiety, warrants further investigation of this early induction schedule. There is still a directional relationship between the changes in the inclusion load and the changes in the physiology in the DG. However, the lack of link to the observed anxiety-like behavior suggests that the decreased excitability in the DG might be related to an independent phenotype not captured by the light-dark paradigm. Considering the behaviors relevant to DG function, the phenotyping needs to be extended with the inclusion of paradigms associated with learning and memory, pattern separation and encoding of spatial information (Kesner 2007). A few examples could be fear-conditioning, object pattern separation and Morris water maze. The behaviors that may potentially be affected by a functional alteration of the DG are also related to the cognitive and memory deficits seen in the PM carriers. Further investigation of this early induction timeline may prove to be relevant for FXAND with a promising possibility of reversibility.

4.4 Continued toxic action in the absence of further pathogenesis

The absence of motor deficits in the dox-induced PrP.90xCGG mice, in spite of 12 weeks of dox exposure, a duration that has previously resulted in poor Rotarod performance in a previous study (Castro et al. 2017), can be attributed to the younger age of the mice at the time of the testing. This situation signals the existence of a period of incubation considering the already high inclusion load present in the cerebellum. An inverse situation that allows drawing the same conclusion can also be found in the same study. In this study, motor deficits have been reported to be absent in the PrP.90xCGG mice after a dox-induction of 8 weeks but became apparent following a 12-week wash-out period (Castro et al. 2017). This means that the damage caused by the initial genetic insult can continue to degrade cell viability even in the absence of further insult and the normal ageing process may also have a role here.

Considering the late onset nature of FXTAS symptoms, it is not implausible to think that some, if not all features of FXTAS may result from additive insults associated both with FXTAS pathogenesis and the normal ageing process. A good example indicating that this might actually be happening is the ubiquitin proteasome system (UPS). The UPS that has been shown to be impaired in FXTAS (Oh et al. 2015), is also known to exhibit a decrease in its function with increasing age (Löw 2011). For the PrP.90xCGG model, the continued toxicity may be the dominant factor rather than the normal ageing process because even the oldest mice that were tested should still be considered as relatively young. However, in the human case, both factors may interact to influence the outcome for the worse. Regardless of this interaction, the continued toxicity in the absence of further pathogenesis would then have very dire implications for the progression of FXTAS and for treatment strategies aiming to interfere with the disease progression. Interventions that successfully halt the pathogenesis of the PM, even before the carriers exhibit any FXTAS symptoms, still cannot guarantee that FXTAS will not surface as the individual ages. Nevertheless, this pessimistic scenario does not occlude the importance and the need for novel treatment strategies that may halt further pathogenesis in the absence of any kind of viable cure.

4.5 Modulation of protein degradation pathways

The UPS is the major mechanism, by which misfolded and aggregated proteins can be degraded and the impaired function of the UPS in FXTAS (Oh et al. 2015) makes it a compelling target for intervention strategies aiming to exploit the endogenous degradation mechanisms. On the other hand, the simple fact that aggregated proteins need to be unfolded in order to pass through the narrow pore of the proteasomal barrel makes them poor substrates for UPS degradation. Also, despite the ubiquitin-positive nature of the FXTAS inclusions, very few of the proteins sequestered into the inclusions were found to be ubiquitinated (Raske and Hagerman 2009). Moreover, no evidence was found that those ubiquitinated proteins were actually polyubiquitinated, a signal for proteins destined for proteasomal degradation. This finding suggests that the impairment related to the UPS in FXTAS may not be related to an overwhelming of the proteasomal degradation pathway due to excessive aggregation, which is indeed the case in some other neurodegenerative disorders (Raske and Hagerman 2009). In this case, the ubiquitin found in the inclusions may signal targeting for degradation through a different endogenous mechanism; i.e. autophagy. The presence of p62 in the inclusions also supports this (Waguri and Komatsu 2009). Unlike the UPS, autophagy can degrade aggregated proteins in bulk, thus aggregates are good candidates for degradation via autophagy. However, the autophagy faces a limitation that the UPS is spared from that is, the autophagic degradation occurs strictly in the cytoplasm (Levine and Kroemer 2008).

Despite the limitation that the autophagic degradation takes place exclusively in the cytoplasm, autophagy is a better candidate as a treatment strategy that is based on modulation endogenous degradation pathways. Autophagy can potentially attenuate the aggregation of FMRpolyG directly in the cytoplasm and thus interfere with one of the two major sources of pathology in FXTAS. Therefore, the induction of autophagy via oral supplement of an autophagy inducer, trehalose was evaluated as an intervention and a potential therapeutic strategy for FXTAS in the PrP.90xCGG model. For this purpose, first the presence of p62 in the inclusions formed by dox-induced PrP.90xCGG mice were confirmed as this was not previously reported for the model. The inclusions formed by cerebellar granule cells of the dox-induced PrP.90CGG mice are “cat-eye” shaped, unlike other brain structures, where inclusions are roughly globular. Antibody raised against p62 stained the inclusions in cerebellum lobule X in a pattern very similar to the antibody raised against FMRpolyG (see Fig.3.14.). Granular layer of the cerebellum lobule X, being the structure that is the most impacted by the presence of the inclusions in this model was selected for quantification of the inclusions. Upon oral trehalose treatment that has been started together with dox-induction and again terminated together, the number of FMRpolyG-positive inclusions decreased in the lobule X. The inclusions of the trehalose treated mice were also found to be smaller in size.

The reduction in the inclusion load in lobule X, where the transgene containing the CGG^{exp} expression is the highest, is an important readout that should potentially affect the behavioral outcome. This beneficial effect of trehalose should be related to increased autophagy levels. However, changes in the autophagy levels are already hard to detect in tissue cultures and even more challenging *in vivo* (Thorburn 2018). When using immunoblotting for quantifications, the preferred method to assess changes related to the autophagy levels is the comparison of the amount of LC3-II among samples (Mizushima and Yoshimori 2007). When tissue samples extracted from cerebellum of four groups of mice compared in an immunoblot setting, LC3-II levels of the groups that were treated with trehalose have been found to be increased (see Fig.3.15.). For this quantification naïve groups of animals were used that were sacrificed while they were still under trehalose treatment in order to be able to detect the increase in autophagy levels induced acutely by trehalose. Moreover, these mice were sacrificed at the same time of the day as autophagy levels fluctuate with the circadian rhythm (Ryzhikov et al. 2019). Nevertheless, it is worth noting that LC3-II can accumulate within the cells via either one of the two autophagic processes; increased autophagosome generation (i.e. induction of autophagy) or incomplete autophagosome fusion and degradation (i.e. inhibition of autophagy) (Thorburn 2018).

Trehalose treatment was indeed beneficial also at the behavior level. On the Rotarod, the detrimental effects of dox-induction on motor performance were evident after 12 weeks of exposure (see Fig.3.16.). However, trehalose was able to reverse this negative effect of dox and brought the performance of the dox-induced group to the levels of non-induced groups both on the constant speed test and the speed ramp test. Trehalose also did not alter the performance of the non-induced group suggesting that it has specifically worked against the harmful mechanisms activated by dox exposure. Bodyweight recordings were also analyzed in relation to the motor performance because differences in the body weight can affect the motor behavior on the Rotarod. No differences were observed between the average body weights of the groups suggesting that the motor performance was not affected by the body weight. Moreover, the motor performance on the accelerating Rotarod was found to be inversely correlated with the number of inclusions in the lobule X and their size (see Fig.3.17.), suggesting that the improvement in the behavioral outcome can result from the improvement in the pathology. However, this correlation should not be interpreted in a relationship with the functions associated with lobule X and motor performance on Rotarod. Rather, this correlation is only suggestive of a recovery of the functions of the cerebellum in general that can be partially observed by looking at the pathological changes in the lobule X. On the other hand, the overall recovery associated with the cerebellum might even be more substantial than the recovery observed at the lobule X alone, given the very high level of transgene expression in this region.

Under the trehalose treatment schedule additional behavioral parameters relevant to FXTAS, other than the motor performance on the Rotarod have been evaluated. These include pawprint patterns for ataxic gait (see Fig.3.18.), trace fear-conditioning (see Fig.3.20.) for hippocampus dependent associative learning and memory, and various anxiety parameters (see Fig.3.19.). No dox-effect were observed for most of these parameters under the conditions these tests have been performed, thus the lack of trehalose effect can only suggest absence of side effects related to this treatment. However, the conditions, under which these experiments were performed were different than the ones applicable to the phenotyping experiments presented earlier. Because the phenotyping experiments were meant as an extension of the previously published work on PrP.90xCGG phenotyping (Castro et al. 2017), the experiments and the dox-induction were performed with complete obedience to the conditions applied in this previous publication. Two key details are; dox-induction was performed by supplying doxycycline in drinking water with sucrose and the training session in the Rotarod experiments comprised of an extensive 3-day exposure to the rotating rod at slow speed that can be considered as an overtraining protocol. For the trehalose treatment experiments dox-induction was achieved by providing dox-containing food pellets and trehalose-containing drinking water to the mice due to palatability problems related to dox in drinking water in the absence of sucrose. For Rotarod experiments, the training session was performed for one day instead of three days. This was done in order to increase the sensitivity of the test to detect smaller differences in the motor performance while ensuring same level of acclimation between different groups (see section 2 - *methods* for more details).

The differences in the conditions between the phenotyping and the trehalose treatment experiments seemed to have implications for the comparability of these two types of studies. Although, the dox exposure in feed also resulted in formation of numerous FMRpolyG-positive inclusions in lobule X, the percent number of these inclusions for the dox+.treh-group is lower than that of the reported numbers for dox+ groups exposed to dox in drinking water. Differences in the total dox intake between these two methods of dox delivery can explain the differences in the detected inclusion numbers. The concentration of dox in feed was carefully adjusted so that it results in a total intake that is comparable to the intake with dox in water. However, it is impossible to have total control over the dox intake in an *ad libitum* setting. This might have resulted in a comparatively less efficient dox-induction via supplementation of dox in feed. On the other hand, the inclusion quantification experiments for the published studies were performed at the Erasmus MC, Rotterdam using slightly different methods in comparison to the ones applied here, from tissue processing to signal detection and to counting.

A lower level of dox induction via supplementation in feed might also explain some differences seen at the behavior level. The previous phenotyping study reports differences in gait parameters upon dox-induction whereas no dox-effect has been detected in any of the gait parameters measured under the trehalose treatment even though the dox-induction schedules are very similar for both studies. On the other hand, the detrimental effect of dox was easily detectable in the Rotarod test. It is then possible that the lower level of dox-induction via dox in feed did not result in a FXTAS manifestation that is strong enough to produce gait impairments but the increased sensitivity of the Rotarod was already able to pick up the differences in the motor performance. The differences in the gait parameters can also be attributed to the non-automated method of the paw-print collection and analysis that may be subject to experimenter bias. A lower level of dox induction might explain the lack of dox-effect in the anxiety measures of the trehalose treatment. Anxiety has also been reported to be detectable at this time-point in the published phenotyping study upon dox induction. However, anxiety measures under the trehalose treatment did not show any dox-effect, except for the marble burying task. Marble burying test may not be a good stand-alone measure for the anxiety because this test is also sensitive to repetitive behaviors related to OCD. Another possibility creating these differences could be that, despite the use of similar anxiety tests under the trehalose treatment and in the published phenotyping work, there are differences in the lighting conditions such as red light versus dim light (open field) and in the reported parameters such as time versus activity in the lit compartment (light/dark transition test).

4.6 Autophagy is ineffective in reversing sustained damage

The improvements observed in the pathology and behavior upon co-administration of trehalose with dox is in line with the notion that the RAN translation product, FMRpolyG can be degraded via autophagy as it accumulates in the cytoplasm. However, FMRpolyG should become inaccessible to autophagy once it is translocated into the nucleus. In the nucleus, FMRpolyG is able to assert its toxicity by contributing to the inclusion formation via a protein gain-of-function mechanism or simply by its aggregation prone nature. Thus, the damage could be permanent even in the absence of more FMRpolyG production and perhaps worsen due to continued toxic action. In order to check the validity of this theory, a second trehalose treatment schedule has been designed. Under this schedule PrP.90xCGG mice were started the oral trehalose supplementation only after they were administered dox for 12 weeks.

The theory seems to hold true at least at the behavior level as there was no beneficial effect related to trehalose despite the detrimental effect of dox on Rotarod motor performance (see Fig.3.21.). In fact, no changes related to trehalose supplementation were observed in any of the behavior parameters. Moreover, the transgene shut down alone was also ineffective complying with the previously published studies. This also indicates the need of a strategy that is not only able to halt the expression of CGG^{exp} but also capable of reversing the already sustained damage in order to cure FXTAS. A substantial worsening due to an interaction between the continued presence of FMRpolyG and increasing age does not seem to be observable from this data. Again, no dox-induction related effects were detected in the gait parameters (see Fig.3.22.). Although the adverse effects of dox-induction on motor performance were comparatively worse at this later time-point, the performance of the dox-control groups compared to their younger counterparts was also worse, signifying a general decline in motor performance with increasing age. However, at this later time point the dox-induced mice gained excessive weight suggesting a potential manifestation of CGG^{exp} driven metabolic changes that are becoming more apparent in spite of the transgene shutdown after the first 12 weeks of the schedule. Perhaps, this happens via interactions with the decline of basal metabolism with increasing age (Krems et al. 2005). Nevertheless, the changes in the body weight were not the determining factor for the differences in the motor performance, as revealed by the lack of correlation between the body weight and performance on the accelerating rod.

A continued toxicity related effect was more obvious in the associative learning and anxiety related parameters. Despite the cessation of its administration after 12 weeks, a dox-induced increase in the fear memory under the trace fear-conditioning paradigm (see Fig.3.24.) was observed both in the shock and neutral context. This phenotype was not present in the previously described earlier time-point. A similar situation was also observed for anxiety parameters as all three tests now show an increased anxiety-like behavior in the PrP.90xCGG mice related to the dox-induction (see Fig.3.23.). This result contradicts the previously published study (Castro et al. 2017), where a rescue of anxiety was reported upon transgene shut down. Again, this incompatibility might be related to the difference in the lighting conditions used for open field test and the difference in the parameters reported for the light-dark transition test. With an additional PPI experiment, sensorimotor behavior was also addressed at this time point (see Fig.3.25.). This experiment was done to investigate whether or not a 12-week dox-induction is sufficient when the mice are age-matched with the 24-week induction study. No PPI deficits related to the 12-week dox-induction were observed under this trehalose treatment schedule. Despite the differences in the dox-induction method, the lack of PPI deficits suggest that 24 weeks dox-induction is necessary to produce problems in sensorimotor gating.

In order to investigate potential genotype independent effects of dox and trehalose, individual groups of wild-type BL6 mice were treated with dox or trehalose for 12 weeks (see Fig.3.26. through 3.28.). These mice have been subjected to the behavior paradigms that were previously affected either by dox or trehalose. The lack of any effects related to dox or trehalose suggests that the effects seen at the behavior level in relation to dox and trehalose are genuine and specific to the genetic and pathologic circumstances that only manifest in the PrP.90xCGG mice. Conversely, the anti-inflammatory properties of doxycycline have been reported to be actually protective in the context of neurodegenerative disorders, including the nigral degeneration related to PD (Santa-Cecília et al. 2019).

4.7 A controversy surrounding trehalose

Trehalose has been shown to play a neuroprotective role in the animal models of neurodegenerative diseases, including Huntington’s disease (HD) (Tanaka et al. 2004), Parkinson’s disease (PD) (Rodríguez-Navarro et al. 2010) and amyotrophic lateral sclerosis (ALS) (Y. Li et al. 2015). There is a considerable consensus between these animal studies in relating the beneficial effects of trehalose to autophagy activation. Despite its recognition as an autophagy inducer (Mardones, Rubinsztein, and Hetz 2016), there is a controversy surrounding the autophagy inducing function of trehalose, especially for studies involving animal models. The controversy for the most part, originates from the very low levels of trehalose found in the brain upon oral administration as compared to the trehalose concentrations required to exert beneficial effects in cell models (Howson et al. 2019), (Lee, Yoon, and Lee 2018). However, also within the literature surrounding the work in cell models, there is a lack of consensus. More recent studies suggest that trehalose might actually interfere with the autophagy flux and act as an autophagy blocker rather than an enhancer (Lee, Yoon, and Lee 2018).

There is also evidence suggesting that trehalose can act at the gut level to induce autophagy in the brain. One study on Lewy body disease reported that only the oral intake of trehalose induces autophagy in the mouse brain and not the intraperitoneal injection of trehalose

(Tanji et al. 2015). This adds even more to the controversy by suggesting that the gastrointestinal system is required for the autophagy induction and for the beneficial effects of trehalose. Research on HD contributed to the controversy by suggesting an additional mechanism other than the induction of autophagy for the neuroprotective role of trehalose (Tanaka et al. 2004). In that study, trehalose was found to reduce mutant huntingtin aggregation by stabilizing the mutant huntingtin and preventing it from folding into form that promotes aggregation.

In the FXTAS field however, there is a disagreement surrounding not trehalose *per se* but autophagy in general. Although the presence of p62 in the inclusions is interpreted as an attempted targeting of the sequestered proteins for autophagic degradation (Ma et al. 2019), a drosophila study on FXTAS did not find any change in CGG^{exp}-associated toxicity when they manipulated the autophagy pathway. In the drosophila model, knocking down essential autophagy genes (either *atg6* or *atg12*) did not result in a worsening of the observed phenotype and feeding the flies with rapamycin did not improve the FXTAS phenotype but worsened the outcome (Oh et al. 2015). On the other hand, another drosophila study demonstrated that rapamycin also worsened CGG^{exp}-induced phenotype but through an autophagy-independent mechanism (Lin et al. 2013). It is also worth noting that in mammals, deletion of the nonredundant ATG genes, including *atg12* result in neonatal death (Kuma, Komatsu, and Mizushima 2017).

In FXTAS, autophagy could potentially explain the absence of inclusions in rapidly dividing cells like fibroblasts (Garcia-Arocena et al. 2010). The absence of inclusions may be attributed to autophagy because during cell division the nuclear envelope breaks down and aggregates may become subjected to autophagic degradation. In fact, recent data on human derived skin fibroblast cultures found increased autophagic flux in FXTAS cells (unpublished conference proceedings by L. Rodrigues-Revenga; Hospital Clinic, Barcelona, Spain - 4th International Conference on FMR1 Premutation, 2019, Rotterdam, The Netherlands). Other than the formation of inclusions, known problems associated with FXTAS can also be targeted via autophagy. Autophagy is capable of compensating for dysfunctional UPS (Demishtein et al. 2017) and degrading accumulated dysfunctional mitochondria, a known toxic mechanism in various neurodegenerative disorders including FXTAS (Ross-Inta et al.

2010). Perhaps the beneficial effect of the trehalose treatment in the PrP.90xCGG model can be partially attributed to an improvement related to the mitochondrial dysfunction.

4.8 Targeting the expanded CGG-repeats

Antisense approaches have been used as therapeutic strategies for neurodegenerative disorders with success (Hu et al. 2009), including the development of an FDA-approved drug, nusinersen for spinal muscular atrophy (Bennett, Krainer, and Cleveland 2019). For FXTAS, targeting the CGG-repeats on the 5'UTR of the *fmr1* mRNA is one of the few ways of modulating both of the main pathogenic mechanisms. ASOs, being not the only option (see section 1.9.) are one of the better tolerated compounds to target CGG^{exp} due to their intracellular stability and low toxicity. The ability to target RNA based on a base-pairing mechanism gives the ASOs another advantage. By binding to the expanded CGG sequences on the mRNA, ASOs can also potentially inhibit the formation of DNA:RNA R-loops, a phenomenon that is implicated to play a role in the expansion of the CGG-repeats at the *fmr1* gene locus. Although R-loop formation is not considered to be one of the main pathomechanisms of FXTAS and normally occurs at various loci throughout the genome, excessive R-loop formation can trigger DNA damage repair response and induce cellular toxicity (P. J. Hagerman and Hagerman 2015). ASO binding to the CGG-repeats in the nucleus can interfere with the formation of RNA:DNA hybrids. ASO binding can also inhibit the association of RNA binding proteins with the CGG^{exp} and block the protein sequestration. On the other hand, upon its export into the cytoplasm, the ASO bound CGG^{exp}-mRNA cannot be translated via RAN translation, whereas canonical translation of FMRP should still be viable (see Fig.4.1.).

The therapeutic potential of an ASO has been for the first time evaluated in an *in vivo* model of FXTAS. For this purpose, a CCG sequence containing ASO that can associate with the CGG repeat locus on the *fmr1* mRNA has been used. The ASO-CCG was delivered to dox-induced PrP.90xCGG mice via ICV infusion for a period of 4 weeks starting 4 weeks after the DOX-induction. This delivery schedule has been designed on the basis of limited damage that is expected upon a short 4 weeks dox-induction. Even after an 8-week long dox-induction PrP90xCGG mice remained asymptomatic (Castro et al. 2017). Dox administration was kept continuous for 12 weeks to ensure manifestation of FXTAS-related molecular and behavioral phenotypes as suggested by the previously described trehalose study. ASO infusion was absent during the last 4 weeks of induction under the assumption that the ASO-CCG would persist in the brain thanks to its high stability. Indeed, this 4+4+4 schedule resulted in a decrease in the number of nuclei with FMRpolyG-positive inclusions and in their size in the cerebellum lobule X (see Fig.3.29.).

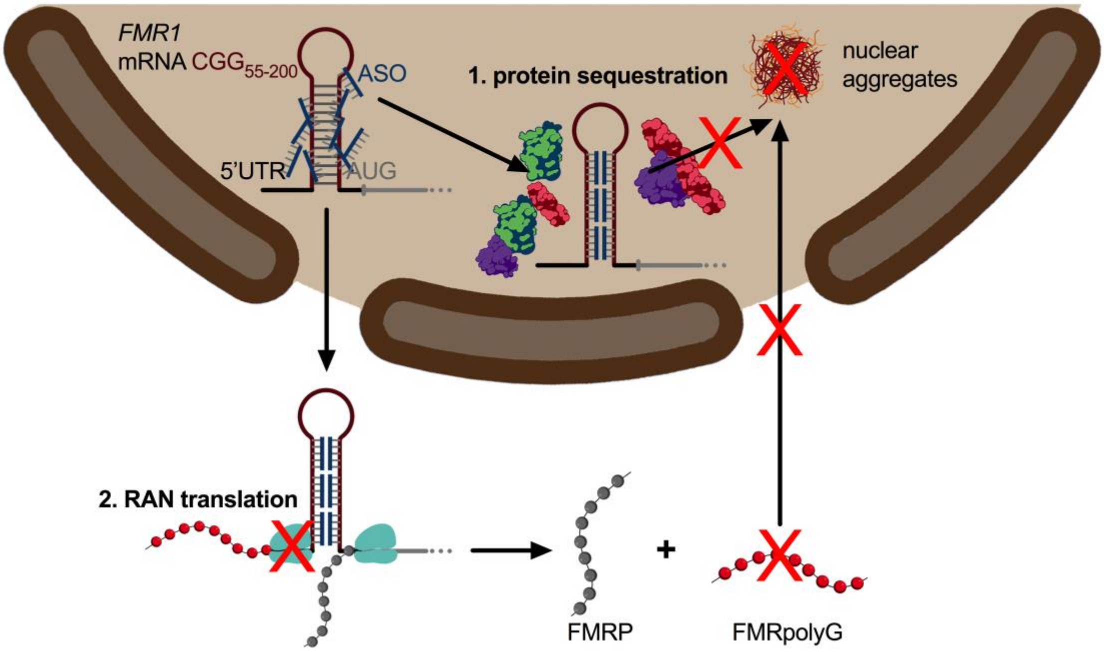

Figure 4.1: The proposed working mechanism of the ASO-CCG

Following transcription, ASO binds to the expanded repeats on the fmr1 mRNA in the nucleus and inhibits the toxic RNA-gain-of-function mechanism. In the cytoplasm, ASO binding inhibits the RAN translation of the repeats and generation of FMRpolyG.

Behaviorally, ASO-CCG infusion corrected the dox-induced motor deficits on the Rotarod without inducing a change in the body weights of the animals (see Fig.3.30.). The number of nuclei with the FMRpolyG focus and their size also correlated inversely with the motor performance on the accelerating Rotarod. Although this 12-week dox-induction schedule did not produce any other behavioral phenotypes (with the exception of marble burying) in the trehalose study, dox-induced mice were tested using the same paradigms as control experiments for the potential off-target effects of the ASO-CCG. The results of the control experiments showed that ASO-CCG did not alter any behavior that dox-induction did not produce (see Fig.3.32. through 3.34.). In the case of the marble burying paradigm, a trend in the direction opposite to the known dox-effect was observed with the ASO-CCG infused mice, which did not become significant (see Fig.3.33.).

The use of PrP.90xCGG model has some very particular advantages but also disadvantages in testing the potential of an antisense therapy. Because the CGG^{exp} expression is controlled by the PrP promotor, the expression level of the CGG^{exp} is exceptionally high especially in the cerebellum lobule X. Thus, the reduction of the number of nuclei with FMRpolyG focus in lobule X is a strong indication of the potency of ASO-CCG. However, this high transgene expression under the PrP promotor may have obscured the full potential of ASO-CCG. Given the fact that a substantial number of inclusions still remain in the lobule X, it is not clear whether the ASO-CCG provided a long-term protection or reinstituted an early asymptomatic era by slowing down the progression of FXTAS. It would be interesting to test the ASO-CCG in a model, where the CGG^{exp} is expressed under the native *fmr1* promotor, such as a KI model.

As the CGG^{exp} is not expressed under the *fmr1* promotor in the PrP.90CGG model, any potential side-effect of the ASO-CCG on the expression of the murine FMRP is automatically excluded. This allows the interpretation of the improvements in the motor performance specifically within the frame of CGG^{exp} toxicity. However, ASO-CCG has indeed been found to interfere with the translation of FMRP in patient-derived fibroblasts carrying CGG^{exp} (unpublished collaboration data obtained by M. Derbis; K. Sobczak's group, AMU, Poznań, Poland). This can potentially be a critical limitation because the FMRP expression is already slightly reduced in FXTAS. However, the reduction in FMRP is not associated with the manifestation of FXTAS, as older adults with FXS, even with undetectable levels of FMRP, do not show FXTAS symptoms (Qurashi et al. 2012). Nevertheless, it is an important next step to figure out how much the ASO-CCG interferes with the FMRP expression *in vivo*.

4.9 The dominating pathomechanism in FXTAS

The mechanisms that produce the therapeutic action of the two *in vivo* intervention strategies presented here are distinct from one another. Trehalose was used as an autophagy inducer and an accelerated degradation of the RAN translation product, FMRpolyG was proposed as the mechanism of action. For ASO-CCG, the proposed mechanism was the binding of CGG^{exp}-mRNA, thereby interfering with both the RAN translation and the toxic RNA gain-of-function. Therefore, there is not a meaningful and direct way of comparing these two strategies. However, both strategies have produced favorable outcomes in terms of motor deficits and molecular pathology. A debate related to the FXTAS research that is still left unanswered is; which mechanism is the dominant one: RNA gain-of-function or RAN translation?

The latest publication that came out of this debate supports RAN translation as the dominant mechanism (Hoem et al. 2019). This study addressed the question by expressing the FMRpolyG in the absence of any CGG^{exp}-mRNA. This was achieved by expressing a plasmid containing CGG-repeats designed not to form a hairpin structure. Expression of this plasmid resulted in FMRpolyG production in various cell lines and reduced cell viability, disrupted the nuclear lamina, and formed aggregates. An equally valid counter argument can be supported by the RAN translation deficient NIH-mouse. This model produces ubiquitin-positive intranuclear inclusions in various structures in the brain without expressing FMRpolyG. This suggests that inclusions are possible without FMRpolyG. However, the phenotype of these mice is rather mild compared to the Dutch-mouse that also produces FMRpolyG (Berman et al. 2014). Also, the repeat size of the CGG^{exp}-mRNA is relatively short in comparison to RNA toxicity driven diseases, such as myotonic dystrophy (Swinnen, Robberecht, and Van Den Bosch 2019). On the other hand, the toxicity associated with FMRpolyG could be overexaggerated because of the use of overexpressing models. The endogenous levels of FMRpolyG in the FXTAS patients was found to be extremely low and at these low concentrations, the quantity of the RAN product is arguably insufficient to drive a toxic action (Ma et al. 2019).

The common mechanism targeted by the autophagy induction and the antisense treatment strategies is the RAN translation or rather the presence of FMRpolyG. The fact that trehalose was beneficial both at the behavior and the molecular levels without any expected impact on the RNA gain-of-function mechanism suggests that RAN translation may be the dominant pathomechanism in the context of PrP.90xCGG model. On the other hand, intervention strategies that can target both of the pathomechanisms, such as ASO-CCG, have the potential of creating a more favorable outcome.

5 Future perspectives and concluding remarks

The repeat expansion mutations associated with the *fmr1* gene affect a significant portion of the human population with implications exceeding single individuals and persisting for generations in the affected families. Without a cure available to treat the disorders associated either with the full mutation or the premutation, affected individuals are limited to symptomatic treatments aiming to limit suffering and improve lifestyle. During my thesis work, I tried to build upon existing knowledge and unveil the unidentified consequences of the expression of premutation size CGG repeats at the molecular, as well as at the behavioral level in the inducible PrP.90xCGG mouse model. This model incorporates many of the human aspects of FXTAS and FXAND and provides a framework to draw parallels to the human case that can be used to better understand the pathology and progression of these disorders. Despite successful identification of several previously undescribed phenotypes in this model, there is more potential. The nigrostriatal degeneration was investigated in the PrP.90xCGG mice in relation to Parkinsonism that is associated with FXTAS. However, tyrosine hydroxylase stainings (see Fig.3.5.) suggest that the degeneration might not be limited to substantia nigra. It may be worth investigating other dopaminergic neuron populations of the basal ganglia including the ventral tegmental area (VTA) in relation to the specific functions of these neurons, the networks they are involved in and potential overlap of their functions with known FXTAS phenotypes. Moreover, potential benefits of a dopamine replacement therapy on these phenotypes are an interesting area that could be explored in the PrP.90xCGG model. Although a deeper investigation is absolutely warranted, PrP.90xCGG model also shows a potential as a tool to address the neuropsychiatric features of the premutation that are associated with FXAND.

In the absence of a cure, I dedicated a substantial part of my thesis work to the development of novel treatment strategies for the PrP.90xCGG model and evaluated the impact of two distinct approaches on the pathology and phenotype. I have specifically focused on strategies with low toxicity and limited side effects because translational potential was set a critical criterion. This approach allowed the evaluation of trehalose and antisense oligonucleotides as potential therapeutics for the treatment of FXTAS. Despite the identified beneficial effects of these interventions, they are constrained by the fact that some of the features of the premutation might progress in spite of these interventions if cells have been harmed already. Therefore, development of new diagnostic tools is needed to monitor presymptomatic development of the premutation and determine suitable starting time points for intended interventions. Ultimately, it is necessary to develop strategies that are not only able to counteract the pathogenic mechanisms but also reverse the damage that may have already been inflicted. The ethical controversy aside, even strategies such as Crispr-based gene editing that can potentially provide a permanent solution are constrained (with exception of germ-line editing) by the implications of the irreversibility of initial damage.

The therapeutic strategies applied here can be extended via incorporation of new approaches and via lessons learned from the pitfalls. One potential side effect associated with the ASO-CCG is its hindrance on the translation of FMRP. The proximity of the CGG^{exp} and the FMRP's canonical start site can explain this interaction. A potential solution can be to design ASOs that target the RAN translation initiation site that is further upstream of the FMRP start codon and limit this interaction. Such an ASO is currently being developed and preliminary reports demonstrate that it does not interfere with the FMRP levels in cell models (unpublished conference proceedings by S.E. Wright; P.K. Todd's group, University of Michigan, Ann Arbor, USA - 4th International Conference on FMR1 Premutation, 2019, Rotterdam, The Netherlands). The ASOs that do not target the CGG repeats directly should however, not be able to inhibit the RNA gain-of-function mechanism. Similarly, the trehalose intervention can be extended via modulation of chaperone mediated transport mechanisms to inhibit the nuclear import of FMRpolyG or to stimulate its nuclear export. A strategy based on modulation of cellular localization mutant proteins has already been shown to improve the outcomes in a mouse model of spinocerebellar ataxia type 3 (Bichelmeier et al. 2007). Nuclear export-based strategies may also have the potential to partially reverse the already inflicted damage by the expression of expanded CGG repeats.

Bibliography

Aitman, Timothy J., Charles Boone, Gary A. Churchill, Michael O. Hengartner, Trudy F. C. Mackay, and Derek L. Stemple. 2011. “The Future of Model Organisms in Human Disease Research.” *Nature Reviews Genetics* 12 (8): 575–82. https://doi.org/10.1038/nrg3047.

Angoa-Pérez, Mariana, Michael J. Kane, Denise I. Briggs, Dina M. Francescutti, and Donald M. Kuhn. 2013. “Marble Burying and Nestlet Shredding as Tests of Repetitive, Compulsive-like Behaviors in Mice.” *Journal of Visualized Experiments*, no. 82 (December): 50978. https://doi.org/10.3791/50978.

Apartis, E., A. Blancher, W. G. Meissner, L. Guyant-Marechal, D. Maltete, T. De Broucker, A.-P. Legrand, et al. 2012. “FXTAS: New Insights and the Need for Revised Diagnostic Criteria.” *Neurology* 79 (18): 1898–1907. https://doi.org/10.1212/WNL.0b013e318271f7ff.

Ariza, Jeanelle, Hailee Rogers, Anna Hartvigsen, Melissa Snell, Michael Dill, Derek Judd, Paul Hagerman, and Verónica Martínez-Cerdeño. 2017. “Iron Accumulation and Dysregulation in the Putamen in Fragile X-Associated Tremor/Ataxia Syndrome.” *Movement Disorders* 32 (4): 585–91. https://doi.org/10.1002/mds.26902.

Ariza, Jeanelle, Hailee Rogers, Angela Monterrubio, Adriana Reyes-Miranda, Paul J. Hagerman, and Verónica Martínez-Cerdeño. 2016. “A Majority of FXTAS Cases Present with Intranuclear Inclusions Within Purkinje Cells.” *The Cerebellum* 15 (5): 546–51. https://doi.org/10.1007/s12311-016-0776-y.

Arocena, Dolores Garcia, Christine K. Iwahashi, Nelly Won, Alexandra Beilina, Anna L. Ludwig, Flora Tassone, Philip H. Schwartz, and Paul J. Hagerman. 2005. “Induction of Inclusion Formation and Disruption of Lamin A/C Structure by Premutation CGG-Repeat RNA in Human Cultured Neural Cells.” *Human Molecular Genetics* 14 (23): 3661–71. https://doi.org/10.1093/hmg/ddi394.

Arrasate, Montserrat, Siddhartha Mitra, Erik S. Schweitzer, Mark R. Segal, and Steven Finkbeiner. 2004. “Inclusion Body Formation Reduces Levels of Mutant Huntingtin and the Risk of Neuronal Death.” *Nature* 431 (7010): 805–10. https://doi.org/10.1038/nature02998.

Bardoni, Barbara, Annette Schenck, and Jean-Louis Mandel. 2001. “The Fragile X Mental Retardation Protein.” *Brain Research Bulletin* 56 (3–4): 375–82. https://doi.org/10.1016/S0361-9230(01)00647-5.

Bennett, C. Frank, Adrian R. Krainer, and Don W. Cleveland. 2019. “Antisense Oligonucleotide Therapies for Neurodegenerative Diseases.” *Annual Review of Neuroscience* 42 (1): 385–406. https://doi.org/10.1146/annurev-neuro-070918-050501.

Berman, Robert F., Ronald AM Buijsen, Karen Usdin, Elizabeth Pintado, Frank Kooy, Dalyir Pretto, Isaac N Pessah, et al. 2014. “Mouse Models of the Fragile X Premutation and Fragile X-Associated Tremor/Ataxia Syndrome.” *Journal of Neurodevelopmental Disorders* 6 (1): 25. https://doi.org/10.1186/1866-1955-6-25.

Bernat, Viachaslau, and Matthew D. Disney. 2015. “RNA Structures as Mediators of Neurological Diseases and as Drug Targets.” *Neuron* 87 (1): 28–46. https://doi.org/10.1016/j.neuron.2015.06.012.

Bichelmeier, Ulrike, T. Schmidt, J. Hubener, Jana Boy, L. Ruttiger, K. Habig, Sven Poths, et al. 2007. “Nuclear Localization of Ataxin-3 Is Required for the Manifestation of Symptoms in SCA3: In Vivo Evidence.” *Journal of Neuroscience* 27 (28): 7418–28. https://doi.org/10.1523/JNEUROSCI.4540-06.2007.

Blitterswijk, Marka van, Mariely DeJesus-Hernandez, and Rosa Rademakers. 2012. “How Do C9ORF72 Repeat Expansions Cause Amyotrophic Lateral Sclerosis and Frontotemporal

Dementia." *Current Opinion in Neurology* 25 (6): 689–700. https://doi.org/10.1097/WCO.0b013e32835a3efb.

Bové, Jordi, Marta Martínez-Vicente, and Miquel Vila. 2011. "Fighting Neurodegeneration with Rapamycin: Mechanistic Insights." *Nature Reviews Neuroscience* 12 (8): 437–52. https://doi.org/10.1038/nrn3068.

Buijsen, R.A.M., Chantal Sellier, Lies-Anne WFM Severijnen, Mustapha Oulad-Abdelghani, Rob FM Verhagen, Robert F Berman, Nicolas Charlet-Berguerand, Rob Willemsen, and Renate K Hukema. 2014. "FMRpolyG-Positive Inclusions in CNS and Non-CNS Organs of a Fragile X Premutation Carrier with Fragile X-Associated Tremor/Ataxia Syndrome." *Acta Neuropathologica Communications* 2 (1): 162. https://doi.org/10.1186/s40478-014-0162-2.

Buijsen, R.A.M., J.A. Visser, P. Kramer, E.A.W.F.M. Severijnen, M. Gearing, N. Charlet-Berguerand, S.L. Sherman, R.F. Berman, R. Willemsen, and R.K. Hukema. 2016. "Presence of Inclusions Positive for Polyglycine Containing Protein, FMRpolyG, Indicates That Repeat-Associated Non-AUG Translation Plays a Role in Fragile X-Associated Primary Ovarian Insufficiency." *Human Reproduction* 31 (1): 158–68. https://doi.org/10.1093/humrep/dev280.

Burman, Michael A., Cassandra A. Simmons, Miles Hughes, and Lei Lei. 2014. "Developing and Validating Trace Fear Conditioning Protocols in C57BL/6 Mice." *Journal of Neuroscience Methods* 222 (1): 111–17. https://doi.org/10.1016/j.jneumeth.2013.11.005.

Castro, Hoanna, Emre Kul, Ronald A.M. Buijsen, Lies-Anne W.F.M. Severijnen, Rob Willemsen, Renate K. Hukema, Oliver Stork, and Mónica Santos. 2017. "Selective Rescue of Heightened Anxiety but Not Gait Ataxia in a Premutation 90CGG Mouse Model of Fragile X-Associated Tremor/Ataxia Syndrome." *Human Molecular Genetics* 26 (11): 2133–45. https://doi.org/10.1093/hmg/ddx108.

Ceravolo, R., A. Antonini, D. Volterrani, C. Rossi, S. Goldwurm, E. Di Maria, L. Kiferle, U. Bonuccelli, and L. Murri. 2005. "Dopamine Transporter Imaging Study in Parkinsonism Occurring in Fragile X Premutation Carriers." *Neurology* 65 (12): 1971–73. https://doi.org/10.1212/01.wnl.0000188821.51055.52.

Coffey, Sarah M., Kylee Cook, Nicole Tartaglia, Flora Tassone, Danh V. Nguyen, Ruiqin Pan, Hannah E. Bronsky, et al. 2008. "Expanded Clinical Phenotype of Women with TheFMR1 Premutation." *American Journal of Medical Genetics Part A* 146A (8): 1009–16. https://doi.org/10.1002/ajmg.a.32060.

Dam, Debby Van, Vanessa Errijgers, R. Frank Kooy, Rob Willemsen, Edwin Mientjes, Ben A. Oostra, and Peter Paul De Deyn. 2005. "Cognitive Decline, Neuromotor and Behavioural Disturbances in a Mouse Model for Fragile-X-Associated Tremor/Ataxia Syndrome (FXTAS)." *Behavioural Brain Research* 162 (2): 233–39. https://doi.org/10.1016/j.bbr.2005.03.007.

Datson, Nicole A., Anchel González-Barriga, Eleni Kourkouta, Rudie Weij, Jeroen van de Giessen, Susan Mulders, Outi Kontkanen, Taneli Heikkinen, Kimmo Lehtimäki, and Judith C. T. van Deutekom. 2017. "The Expanded CAG Repeat in the Huntingtin Gene as Target for Therapeutic RNA Modulation throughout the HD Mouse Brain." Edited by Yuqing Li. *PLOS ONE* 12 (2): e0171127. https://doi.org/10.1371/journal.pone.0171127.

Daubner, S Colette, Tiffany Le, and Shanzhi Wang. 2011. "Tyrosine Hydroxylase and Regulation of Dopamine Synthesis." *Archives of Biochemistry and Biophysics* 508 (1): 1–12. https://doi.org/10.1016/j.abb.2010.12.017.

Demishtein, Alik, Milana Fraiberg, Dikla Berko, Boaz Tirosh, Zvulun Elazar, and Ami Navon.

2017. “SQSTM1/P62-Mediated Autophagy Compensates for Loss of Proteasome Polyubiquitin Recruiting Capacity.” *Autophagy* 13 (10): 1697–1708. https://doi.org/10.1080/15548627.2017.1356549.

Disney, Matthew D., Biao Liu, Wang-Yong Yang, Chantal Sellier, Tuan Tran, Nicolas Charlet-Berguerand, and Jessica L. Childs-Disney. 2012. “A Small Molecule That Targets r(CGG) Exp and Improves Defects in Fragile X-Associated Tremor Ataxia Syndrome.” *ACS Chemical Biology* 7 (10): 1711–18. https://doi.org/10.1021/cb300135h.

Dubińska-Magiera, Magda, Magdalena Chmielewska, Katarzyna Kozioł, Magdalena Machowska, Christopher J. Hutchison, Martin W. Goldberg, and Ryszard Rzepecki. 2016. “Xenopus LAP2β Protein Knockdown Affects Location of Lamin B and Nucleoporins and Has Effect on Assembly of Cell Nucleus and Cell Viability.” *Protoplasma* 253 (3): 943–56. https://doi.org/10.1007/s00709-015-0861-y.

Engin, Elif, Kiersten S Smith, Yudong Gao, David Nagy, Rachel A Foster, Evgeny Tsvetkov, Ruth Keist, et al. 2016. “Modulation of Anxiety and Fear via Distinct Intrahippocampal Circuits.” *ELife* 5 (March): 1–23. https://doi.org/10.7554/eLife.14120.

Entezam, Ali, Rea Biacsi, Bonnie Orrison, Tapas Saha, Gloria E. Hoffman, Ed Grabczyk, Robert L. Nussbaum, and Karen Usdin. 2007. “Regional FMRP Deficits and Large Repeat Expansions into the Full Mutation Range in a New Fragile X Premutation Mouse Model.” *Gene* 395 (1–2): 125–34. https://doi.org/10.1016/j.gene.2007.02.026.

Fernagut, Pierre O., Elsa Diguet, Bertrand Labattu, and François Tison. 2002. “A Simple Method to Measure Stride Length as an Index of Nigrostriatal Dysfunction in Mice.” *Journal of Neuroscience Methods* 113 (2): 123–30. https://doi.org/10.1016/S0165-0270(01)00485-X.

Fink, Dorothy A., Lawrence M. Nelson, Reed Pyeritz, Josh Johnson, Stephanie L. Sherman, Yoram Cohen, and Shai E. Elizur. 2018. “Fragile X Associated Primary Ovarian Insufficiency (FXPOI): Case Report and Literature Review.” *Frontiers in Genetics* 9 (November): 1–12. https://doi.org/10.3389/fgene.2018.00529.

Garcia-Arocena, Dolores, Jane E. Yang, Judith R. Brouwer, Flora Tassone, Christine Iwahashi, Elizabeth M. Berry-Kravis, Christopher G. Goetz, et al. 2010. “Fibroblast Phenotype in Male Carriers of FMR1 Premutation Alleles.” *Human Molecular Genetics* 19 (2): 299–312. https://doi.org/10.1093/hmg/ddp497.

Gareri, Pietro, Alberto Castagna, Antonino Maria Cotroneo, Salvatore Putignano, Giovambattista De Sarro, and Amalia Cecilia Bruni. 2015. “The Role of Citicoline in Cognitive Impairment: Pharmacological Characteristics, Possible Advantages, and Doubts for an Old Drug with New Perspectives.” *Clinical Interventions in Aging* 10 (September): 1421. https://doi.org/10.2147/CIA.S87886.

Geary, Richard S., Daniel Norris, Rosie Yu, and C. Frank Bennett. 2015. “Pharmacokinetics, Biodistribution and Cell Uptake of Antisense Oligonucleotides.” *Advanced Drug Delivery Reviews* 87: 46–51. https://doi.org/10.1016/j.addr.2015.01.008.

Glineburg, M. Rebecca, Peter K. Todd, Nicolas Charlet-Berguerand, and Chantal Sellier. 2018. “Repeat-Associated Non-AUG (RAN) Translation and Other Molecular Mechanisms in Fragile X Tremor Ataxia Syndrome.” *Brain Research* 1693 (August): 43–54. https://doi.org/10.1016/j.brainres.2018.02.006.

Gohel, Dhruv, Lakshmi Sripada, Paresh Prajapati, Kritarth Singh, Milton Roy, Darshan Kotadia, Flora Tassone, Nicolas Charlet-Berguerand, and Rajesh Singh. 2019. “FMRpolyG Alters Mitochondrial Transcripts Level and Respiratory Chain Complex Assembly in Fragile X Associated Tremor/Ataxia Syndrome [FXTAS].” *Biochimica et Biophysica Acta (BBA) - Molecular Basis of Disease* 1865 (6): 1379–88.

https://doi.org/10.1016/j.bbadis.2019.02.010.

Greco, C. M., R. F. Berman, R. M. Martin, F. Tassone, P. H. Schwartz, A. Chang, B. D. Trapp, et al. 2006. “Neuropathology of Fragile X-Associated Tremor/Ataxia Syndrome (FXTAS).” *Brain* 129 (1): 243–55. https://doi.org/10.1093/brain/awh683.

Greco, C.M., Randi J. Hagerman, F. Tassone, A.E. Chudley, M.R. Del Bigio, S. Jacquemont, M. Leehey, and Paul J. Hagerman. 2002. “Neuronal Intranuclear Inclusions in a New Cerebellar Tremor/Ataxia Syndrome among Fragile X Carriers.” *Brain* 125 (8): 1760–71. https://doi.org/10.1093/brain/awf184.

Green, Katelyn M, Udit Sheth, Brittany N Flores, Shannon E Wright, Alexandra Sutter, Michael G Kearse, Sami Barmada, Magdalena I Ivanova, and Peter K Todd. 2019. “High-Throughput Screening Yields Several Small-Molecule Inhibitors of Repeat-Associated Non-AUG Translation.” *Journal of Biological Chemistry*, no. 1 (October): jbc.RA119.009951. https://doi.org/10.1074/jbc.RA119.009951.

Hagerman, Paul J., and Randi J. Hagerman. 2015. “Fragile X-Associated Tremor/Ataxia Syndrome.” *Annals of the New York Academy of Sciences* 1338 (1): 58–70. https://doi.org/10.1111/nyas.12693.

Hagerman, Randi J., and Paul J. Hagerman. 2002. “The Fragile X Premutation: Into the Phenotypic Fold.” *Current Opinion in Genetics & Development* 12 (3): 278–83. https://doi.org/10.1016/S0959-437X(02)00299-X.

Hagerman, Randi J., Dragana Protic, Akash Rajaratnam, Maria J. Salcedo-Arellano, Elber Yuksel Aydin, and Andrea Schneider. 2018. “Fragile X-Associated Neuropsychiatric Disorders (FXAND).” *Frontiers in Psychiatry* 9 (November): 1–9. https://doi.org/10.3389/fpsyt.2018.00564.

Hall, Deborah A., Rachael C. Birch, Mathieu Anheim, Aia E. Jønch, Elizabeth Pintado, Joanne O’Keefe, Julian N. Trollor, et al. 2014. “Emerging Topics in FXTAS.” *Journal of Neurodevelopmental Disorders* 6 (1): 31. https://doi.org/10.1186/1866-1955-6-31.

Hall, Deborah A., Katherine Howard, Randi J. Hagerman, and Maureen A. Leehey. 2009. “Parkinsonism in FMR1 Premutation Carriers May Be Indistinguishable from Parkinson Disease.” *Parkinsonism & Related Disorders* 15 (2): 156–59. https://doi.org/10.1016/j.parkreldis.2008.04.037.

Hall, Deborah A, Maureen A Leehey, Elizabeth Berry-Kravis, and Randi J Hagerman. 2016. “Treatment and Management of FXTAS.” In *FXTAS, FXPOI, and Other Premutation Disorders*, edited by Flora Tassone and Deborah A Hall, 181–97. Cham: Springer International Publishing. https://doi.org/10.1007/978-3-319-33898-9_9.

Handa, Vaishali. 2003. “The Fragile X Syndrome Repeats Form RNA Hairpins That Do Not Activate the Interferon-Inducible Protein Kinase, PKR, but Are Cut by Dicer.” *Nucleic Acids Research* 31 (21): 6243–48. https://doi.org/10.1093/nar/gkg818.

Hayashi, Etsuko, Kazuyoshi Kuratani, Mine Kinoshita, and Hideaki Hara. 2010. “Pharmacologically Distinctive Behaviors Other than Burying Marbles during the Marble Burying Test in Mice.” *Pharmacology* 86 (5–6): 293–96. https://doi.org/10.1159/000321190.

Hoem, Gry, Kenneth Bowitz Larsen, Aud Øvervatn, Andreas Brech, Trond Lamark, Eva Sjøttem, and Terje Johansen. 2019. “The FMRpolyGlycine Protein Mediates Aggregate Formation and Toxicity Independent of the CGG MRNA Hairpin in a Cellular Model for FXTAS.” *Frontiers in Genetics* 10 (MAR): 1–18. https://doi.org/10.3389/fgene.2019.00249.

Howson, Patrick A., Tom H. Johnston, Paula Ravenscroft, Michael P. Hill, Jin Su, Jonathan M. Brotchie, and James B. Koprich. 2019. “Beneficial Effects of Trehalose on Striatal

Dopaminergic Deficits in Rodent and Primate Models of Synucleinopathy in Parkinson's Disease." *Journal of Pharmacology and Experimental Therapeutics* 369 (3): 364–74. https://doi.org/10.1124/jpet.118.255695.

Hu, Jiaxin, Masayuki Matsui, Keith T Gagnon, Jacob C Schwartz, Sylvie Gabillet, Khalil Arar, Jun Wu, Ilya Bezprozvanny, and David R Corey. 2009. "Allele-Specific Silencing of Mutant Huntingtin and Ataxin-3 Genes by Targeting Expanded CAG Repeats in MRNAs." *Nature Biotechnology* 27 (5): 478–84. https://doi.org/10.1038/nbt.1539.

Hukema, Renate K., Ronald A.M. Buijsen, Martijn Schonewille, Chris Raske, Lies-Anne W.F.M. Severijnen, Ingeborg Nieuwenhuizen-Bakker, Rob F.M. Verhagen, et al. 2015. "Reversibility of Neuropathology and Motor Deficits in an Inducible Mouse Model for FXTAS." *Human Molecular Genetics* 24 (17): 4948–57. https://doi.org/10.1093/hmg/ddv216.

Hukema, Renate K., Ronald Am Buijsen, Chris Raske, Lies Anne Severijnen, Ingeborg Nieuwenhuizen-Bakker, Michelle Minneboo, Alex Maas, et al. 2014. "Induced Expression of Expanded CGG RNA Causes Mitochondrial Dysfunction in Vivo." *Cell Cycle* 13 (16): 2600–2608. https://doi.org/10.4161/15384101.2014.943112.

Irwin, Scott A. 2000. "Dendritic Spine Structural Anomalies in Fragile-X Mental Retardation Syndrome." *Cerebral Cortex* 10 (10): 1038–44. https://doi.org/10.1093/cercor/10.10.1038.

Iwahashi, C. K., D. H. Yasui, H.-J. An, C. M. Greco, F. Tassone, K. Nannen, B. Babineau, C. B. Lebrilla, R. J. Hagerman, and P. J. Hagerman. 2006. "Protein Composition of the Intranuclear Inclusions of FXTAS." *Brain* 129 (1): 256–71. https://doi.org/10.1093/brain/awh650.

Kaganovich, Daniel, Ron Kopito, and Judith Frydman. 2008. "Misfolded Proteins Partition between Two Distinct Quality Control Compartments." *Nature* 454 (7208): 1088–95. https://doi.org/10.1038/nature07195.

Kagi, G, K. P. Bhatia, and E. Tolosa. 2010. "The Role of DAT-SPECT in Movement Disorders." *Journal of Neurology, Neurosurgery & Psychiatry* 81 (1): 5–12. https://doi.org/10.1136/jnnp.2008.157370.

Kearse, Michael G., and Jeremy E. Wilusz. 2017. "Non-AUG Translation: A New Start for Protein Synthesis in Eukaryotes." *Genes & Development* 31 (17): 1717–31. https://doi.org/10.1101/gad.305250.117.

Kesner, Raymond P. 2007. "A Behavioral Analysis of Dentate Gyrus Function." In *Progress in Brain Research*, 163:567–76. https://doi.org/10.1016/S0079-6123(07)63030-1.

Krems, C., P. M. Lührmann, A. Straßburg, B. Hartmann, and Monika Neuhäuser-Berthold. 2005. "Lower Resting Metabolic Rate in the Elderly May Not Be Entirely Due to Changes in Body Composition." *European Journal of Clinical Nutrition* 59 (2): 255–62. https://doi.org/10.1038/sj.ejcn.1602066.

Kuma, Akiko, Masaaki Komatsu, and Noboru Mizushima. 2017. "Autophagy-Monitoring and Autophagy-Deficient Mice." *Autophagy* 13 (10): 1619–28. https://doi.org/10.1080/15548627.2017.1343770.

Lee, He-Jin, Ye-Seul Yoon, and Seung-Jae Lee. 2018. "Mechanism of Neuroprotection by Trehalose: Controversy Surrounding Autophagy Induction." *Cell Death & Disease* 9 (7): 712. https://doi.org/10.1038/s41419-018-0749-9.

Leehey, Maureen A. 2009. "Fragile X-Associated Tremor/Ataxia Syndrome." *Journal of Investigative Medicine* 57 (8): 830–36. https://doi.org/10.2310/JIM.0b013e3181af59c4.

Lempel, Augusto Abel, Lucia Coll, Alejandro F. Schinder, Osvaldo Daniel Uchitel, and Joaquin Piriz. 2017. "Chronic Pregabalin Treatment Decreases Excitability of Dentate Gyrus and

Accelerates Maturation of Adult-Born Granule Cells." *Journal of Neurochemistry* 140 (2): 257–67. https://doi.org/10.1111/jnc.13740.

Levine, Beth, and Guido Kroemer. 2008. "Autophagy in the Pathogenesis of Disease." *Cell* 132 (1): 27–42. https://doi.org/10.1016/j.cell.2007.12.018.

Li, Y., Y. Guo, X. Wang, X. Yu, W. Duan, K. Hong, J. Wang, H. Han, and C. Li. 2015. "Trehalose Decreases Mutant SOD1 Expression and Alleviates Motor Deficiency in Early but Not End-Stage Amyotrophic Lateral Sclerosis in a SOD1-G93A Mouse Model." *Neuroscience* 298 (July): 12–25. https://doi.org/10.1016/j.neuroscience.2015.03.061.

Lin, Yunting, Chengyuan Tang, Hua He, and Ranhui Duan. 2013. "Activation of MTOR Ameliorates Fragile X Premutation RCGG Repeat-Mediated Neurodegeneration." Edited by Mathias Toft. *PLoS ONE* 8 (4): e62572. https://doi.org/10.1371/journal.pone.0062572.

Linsalata, Alexander E, Fang He, Ahmed M Malik, Mary Rebecca Glineburg, Katelyn M Green, Sam Natla, Brittany N Flores, et al. 2019. "<scp>DDX</Scp> 3X and Specific Initiation Factors Modulate *<scp>FMR</Scp> 1* Repeat-associated Non-AUG-initiated Translation." *EMBO Reports* 20 (9): 1–18. https://doi.org/10.15252/embr.201847498.

Liu, Wei Jing, Lin Ye, Wei Fang Huang, Lin Jie Guo, Zi Gan Xu, Hong Luan Wu, Chen Yang, and Hua Feng Liu. 2016. "P62 Links the Autophagy Pathway and the Ubiqutin–Proteasome System upon Ubiquitinated Protein Degradation." *Cellular & Molecular Biology Letters* 21 (1): 29. https://doi.org/10.1186/s11658-016-0031-z.

Löw, Peter. 2011. "The Role of Ubiquitin–Proteasome System in Ageing." *General and Comparative Endocrinology* 172 (1): 39–43. https://doi.org/10.1016/j.ygcen.2011.02.005.

Lugo, Joaquin N., Gregory D. Smith, and Andrew J. Holley. 2014. "Trace Fear Conditioning in Mice." *Journal of Visualized Experiments*, no. 85 (March): 1–7. https://doi.org/10.3791/51180.

Luo, Majing, Xueya Zhao, Ying Song, Hanhua Cheng, and Rongjia Zhou. 2016. "Nuclear Autophagy: An Evolutionarily Conserved Mechanism of Nuclear Degradation in the Cytoplasm." *Autophagy* 12 (11): 1973–83. https://doi.org/10.1080/15548627.2016.1217381.

Ma, Lisa, Anthony W. Herren, Glenda Espinal, Jamie Randol, Bridget McLaughlin, Veronica Martinez-Cerdeño, Isaac N. Pessah, Randi J. Hagerman, and Paul J. Hagerman. 2019. "Composition of the Intranuclear Inclusions of Fragile X-Associated Tremor/Ataxia Syndrome." *Acta Neuropathologica Communications* 7 (1): 143. https://doi.org/10.1186/s40478-019-0796-1.

Madeo, G., F. Alemseged, B. Di Pietro, O. Schillaci, and A. Pisani. 2013. "Early Abnormalities in 123I-Ioflupane (DaTSCAN) Imaging in the Fragile X-Associated Tremor Ataxia Syndrome (FXTAS): A Case Report." *Neurological Sciences* 34 (8): 1475–77. https://doi.org/10.1007/s10072-012-1223-6.

Mandel, J.L., and V. Biancalana. 2004. "Fragile X Mental Retardation Syndrome: From Pathogenesis to Diagnostic Issues." *Growth Hormone & IGF Research* 14 (SUPPL. A): 158–65. https://doi.org/10.1016/j.ghir.2004.03.034.

Mann, Amandeep, and Marie-Francoise Chesselet. 2015. "Techniques for Motor Assessment in Rodents." In *Movement Disorders*, Second Edi, 139–57. Elsevier. https://doi.org/10.1016/B978-0-12-405195-9.00008-1.

Mardones, Pablo, David C. Rubinsztein, and Claudio Hetz. 2016. "Mystery Solved: Trehalose Kickstarts Autophagy by Blocking Glucose Transport." *Science Signaling* 9 (416): fs2–fs2. https://doi.org/10.1126/scisignal.aaf1937.

McEchron, Matthew D., Hans Bouwmeester, Wilbur Tseng, Craig Weiss, and John F. Disterhoft. 1999. “Hippocampectomy Disrupts Auditory Trace Fear Conditioning and Contextual Fear Conditioning in the Rat.” *Hippocampus* 8 (6): 638–46. https://doi.org/10.1002/(SICI)1098-1063(1998)8:6<638::AID-HIPO6>3.0.CO;2-Q.

Mizushima, Noboru, and Tamotsu Yoshimori. 2007. “How to Interpret LC3 Immunoblotting.” *Autophagy* 3 (6): 542–45. https://doi.org/10.4161/auto.4600.

Muslimovic, D., Bart Post, Johannes D. Speelman, and Ben Schmand. 2005. “Cognitive Profile of Patients with Newly Diagnosed Parkinson Disease.” *Neurology* 65 (8): 1239–45. https://doi.org/10.1212/01.wnl.0000180516.69442.95.

Niu, Yu-Qiong, Jin-Chen Yang, Deborah A. Hall, Maureen A. Leehey, Flora Tassone, John M. Olichney, Randi J. Hagerman, and Lin Zhang. 2014. “Parkinsonism in Fragile X-Associated Tremor/Ataxia Syndrome (FXTAS): Revisited.” *Parkinsonism & Related Disorders* 20 (4): 456–59. https://doi.org/10.1016/j.parkreldis.2014.01.006.

Oh, Seok Yoon, Fang He, Amy Krans, Michelle Frazer, J. Paul Taylor, Henry L. Paulson, and Peter K. Todd. 2015. “RAN Translation at CGG Repeats Induces Ubiquitin Proteasome System Impairment in Models of Fragile X-Associated Tremor Ataxia Syndrome.” *Human Molecular Genetics* 24 (15): 4317–26. https://doi.org/10.1093/hmg/ddv165.

Pablo-Fernandez, Eduardo De, Karen M. Doherty, Janice L. Holton, Tamas Revesz, Atbin Djamshidian, Patricia Limousin, Kailash P. Bhatia, Thomas T. Warner, Andrew J. Lees, and Helen Ling. 2015. “Concomitant Fragile X-Associated Tremor Ataxia Syndrome and Parkinson’s Disease: A Clinicopathological Report of Two Cases: Table 1.” *Journal of Neurology, Neurosurgery & Psychiatry* 86 (8): 934–36. https://doi.org/10.1136/jnnp-2014-309460.

Pretto, Dalyir, Carolyn M. Yrigollen, Hiu-Tung Tang, John Williamson, Glenda Espinal, Chris K. Iwahashi, Blythe Durbin-Johnson, Randi J. Hagerman, Paul J. Hagerman, and Flora Tassone. 2014. “Clinical and Molecular Implications of Mosaicism in FMR1 Full Mutations.” *Frontiers in Genetics* 5 (SEP): 1–11. https://doi.org/10.3389/fgene.2014.00318.

Qin, Mei, Ali Entezam, Karen Usdin, Tianjian Huang, Zhong-Hua Liu, Gloria E. Hoffman, and Carolyn B. Smith. 2011. “A Mouse Model of the Fragile X Premutation: Effects on Behavior, Dendrite Morphology, and Regional Rates of Cerebral Protein Synthesis.” *Neurobiology of Disease* 42 (1): 85–98. https://doi.org/10.1016/j.nbd.2011.01.008.

Qurashi, Abrar, Huijie Liu, Laurie Ray, David L. Nelson, Ranhui Duan, and Peng Jin. 2012. “Chemical Screen Reveals Small Molecules Suppressing Fragile X Premutation RCGG Repeat-Mediated Neurodegeneration in Drosophila.” *Human Molecular Genetics* 21 (9): 2068–75. https://doi.org/10.1093/hmg/dds024.

Ralph, Rebecca J., Martin P. Paulus, Fabio Fumagalli, Marc G. Caron, and Mark A. Geyer. 2001. “Prepulse Inhibition Deficits and Perseverative Motor Patterns in Dopamine Transporter Knock-Out Mice: Differential Effects of D1 and D2 Receptor Antagonists.” *The Journal of Neuroscience* 21 (1): 305–13. https://doi.org/10.1523/JNEUROSCI.21-01-00305.2001.

Raske, Christopher, and Paul J. Hagerman. 2009. “Molecular Pathogenesis of Fragile X-Associated Tremor/Ataxia Syndrome.” *Journal of Investigative Medicine* 57 (8): 825–29. https://doi.org/10.2310/JIM.0b013e3181be329a.

Rau, Andrew R., Ann M. Chappell, Tracy R. Butler, Olusegun J. Ariwodola, and Jeff L. Weiner. 2015. “Increased Basolateral Amygdala Pyramidal Cell Excitability May Contribute to the Anxiogenic Phenotype Induced by Chronic Early-Life Stress.” *Journal of Neuroscience* 35 (26): 9730–40. https://doi.org/10.1523/JNEUROSCI.0384-15.2015.

Raybuck, Jonathan D., and K. Matthew Lattal. 2011. “Double Dissociation of Amygdala and Hippocampal Contributions to Trace and Delay Fear Conditioning.” Edited by Joe Z. Tsien. *PLoS ONE* 6 (1): e15982. https://doi.org/10.1371/journal.pone.0015982.

Renoux, A.J., K.J. Sala-Hamrick, N.M. Carducci, M. Frazer, K.E. Halsey, M.A. Sutton, D.F. Dolan, G.G. Murphy, and P.K. Todd. 2014. “Impaired Sensorimotor Gating in Fmr1 Knock out and Fragile X Premutation Model Mice.” *Behavioural Brain Research* 267 (1): 42–45. https://doi.org/10.1016/j.bbr.2014.03.013.

Robin, Gaëlle, José R. López, Glenda M. Espinal, Susan Hulsizer, Paul J. Hagerman, and Isaac N. Pessah. 2017. “Calcium Dysregulation and Cdk5-ATM Pathway Involved in a Mouse Model of Fragile X-Associated Tremor/Ataxia Syndrome.” *Human Molecular Genetics* 26 (14): 2649–66. https://doi.org/10.1093/hmg/ddx148.

Rodríguez-Navarro, Jose A., Laura Rodríguez, María J. Casarejos, Rosa M. Solano, Ana Gómez, Juan Perucho, Ana María Cuervo, Justo García de Yébenes, and María A. Mena. 2010. “Trehalose Ameliorates Dopaminergic and Tau Pathology in Parkin Deleted/Tau Overexpressing Mice through Autophagy Activation.” *Neurobiology of Disease* 39 (3): 423–38. https://doi.org/10.1016/j.nbd.2010.05.014.

Rogers, Hailee, Jeanelle Ariza, Angela Monterrubio, Paul Hagerman, and Verónica Martínez-Cerdeño. 2016. “Cerebellar Mild Iron Accumulation in a Subset of FMR1 Premutation Carriers with FXTAS.” *The Cerebellum* 15 (5): 641–44. https://doi.org/10.1007/s12311-016-0798-5.

Rosario, Roseanne, Panagiotis Filis, Victoria Tessyman, Hazel Kinnell, Andrew J. Childs, Nicola K. Gray, and Richard A. Anderson. 2016. “FMRP Associates with Cytoplasmic Granules at the Onset of Meiosis in the Human Oocyte.” Edited by Barbara Bardoni. *PLOS ONE* 11 (10): e0163987. https://doi.org/10.1371/journal.pone.0163987.

Rose, April, and Christian Schlieker. 2012. “Alternative Nuclear Transport for Cellular Protein Quality Control.” *Trends in Cell Biology* 22 (10): 509–14. https://doi.org/10.1016/j.tcb.2012.07.003.

Ross-Inta, Catherine, Alicja Omanska-Klusek, Sarah Wong, Cedrick Barrow, Dolores Garcia-Arocena, Christine Iwahashi, Elizabeth Berry-Kravis, Randi J. Hagerman, Paul J. Hagerman, and Cecilia Giulivi. 2010. “Evidence of Mitochondrial Dysfunction in Fragile X-Associated Tremor/Ataxia Syndrome.” *Biochemical Journal* 429 (3): 545–52. https://doi.org/10.1042/BJ20091960.

Ryzhikov, Mikhail, Anna Ehlers, Deborah Steinberg, Wenfang Xie, Eitan Oberlander, Samuel Brown, Petra E. Gilmore, et al. 2019. “Diurnal Rhythms Spatially and Temporally Organize Autophagy.” *Cell Reports* 26 (7): 1880-1892.e6. https://doi.org/10.1016/j.celrep.2019.01.072.

Santa-Cecília, Flávia Viana, Caio Abner Leite, Elaine Del-Bel, and Rita Raisman-Vozari. 2019. “The Neuroprotective Effect of Doxycycline on Neurodegenerative Diseases.” *Neurotoxicity Research* 35 (4): 981–86. https://doi.org/10.1007/s12640-019-00015-z.

Scaglione, C., A. Ginestroni, A. Vella, M. T. Dotti, R. Della Nave, G. Rizzo, M. T. Cristofaro, et al. 2008. “MRI and SPECT of Midbrain and Striatal Degeneration in Fragile X-Associated Tremor/Ataxia Syndrome.” *Journal of Neurology* 255 (1): 144–46. https://doi.org/10.1007/s00415-007-0711-8.

Schneider, Andrea, Elizabeth Ballinger, Alyssa Chavez, Flora Tassone, Randi J. Hagerman, and David Hessl. 2012. “Prepulse Inhibition in Patients with Fragile X-Associated Tremor Ataxia Syndrome.” *Neurobiology of Aging* 33 (6): 1045–53. https://doi.org/10.1016/j.neurobiolaging.2010.09.002.

Seibenhener, Michael L., and Michael C. Wooten. 2015. “Use of the Open Field Maze to

Measure Locomotor and Anxiety-like Behavior in Mice.” *Journal of Visualized Experiments*, no. 96 (February): 1–6. https://doi.org/10.3791/52434.

Sellier, Chantal, Ronald A.M. Buijsen, Fang He, Sam Natla, Laura Jung, Philippe Tropel, Angeline Gaucherot, et al. 2017. “Translation of Expanded CGG Repeats into FMRpolyG Is Pathogenic and May Contribute to Fragile X Tremor Ataxia Syndrome.” *Neuron* 93 (2): 331–47. https://doi.org/10.1016/j.neuron.2016.12.016.

Sellier, Chantal, Fernande Freyermuth, Ricardos Tabet, Tuan Tran, Fang He, Frank Ruffenach, Violaine Alunni, et al. 2013. “Sequestration of DROSHA and DGCR8 by Expanded CGG RNA Repeats Alters MicroRNA Processing in Fragile X-Associated Tremor/Ataxia Syndrome.” *Cell Reports* 3 (3): 869–80. https://doi.org/10.1016/j.celrep.2013.02.004.

Sellier, Chantal, Frédérique Rau, Yilei Liu, Flora Tassone, Renate K. Hukema, Renata Gattoni, Anne Schneider, et al. 2010. “Sam68 Sequestration and Partial Loss of Function Are Associated with Splicing Alterations in FXTAS Patients.” *The EMBO Journal* 29 (7): 1248–61. https://doi.org/10.1038/emboj.2010.21.

Seritan, Andreea L., Danh V. Nguyen, Yi Mu, Flora Tassone, James A. Bourgeois, Andrea Schneider, Jennifer B. Cogswell, et al. 2014. “Memantine for Fragile X–Associated Tremor/Ataxia Syndrome.” *The Journal of Clinical Psychiatry* 75 (03): 264–71. https://doi.org/10.4088/JCP.13m08546.

Sharp, B. M. 2017. “Basolateral Amygdala and Stress-Induced Hyperexcitability Affect Motivated Behaviors and Addiction.” *Translational Psychiatry* 7 (8): e1194–e1194. https://doi.org/10.1038/tp.2017.161.

Sherman, Stephanie L., Eliza C. Curnow, Charles A. Easley, Peng Jin, Renate K. Hukema, Maria Isabel Tejada, Rob Willemsen, and Karen Usdin. 2014. “Use of Model Systems to Understand the Etiology of Fragile X-Associated Primary Ovarian Insufficiency (FXPOI).” *Journal of Neurodevelopmental Disorders* 6 (1): 26. https://doi.org/10.1186/1866-1955-6-26.

Shoji, Hirotaka, Keizo Takao, Satoko Hattori, and Tsuyoshi Miyakawa. 2014. “Contextual and Cued Fear Conditioning Test Using a Video Analyzing System in Mice.” *Journal of Visualized Experiments*, no. 85 (March): 1–13. https://doi.org/10.3791/50871.

Sigurdsson, Torfi, Valérie Doyère, Christopher K. Cain, and Joseph E. LeDoux. 2007. “Long-Term Potentiation in the Amygdala: A Cellular Mechanism of Fear Learning and Memory.” *Neuropharmacology* 52 (1): 215–27. https://doi.org/10.1016/j.neuropharm.2006.06.022.

Swerdlow, Neal R, David L Braff, and Mark A Geyer. 2016. “Sensorimotor Gating of the Startle Reflex: What We Said 25 Years Ago, What Has Happened since Then, and What Comes Next.” *Journal of Psychopharmacology* 30 (11): 1072–81. https://doi.org/10.1177/0269881116661075.

Swinnen, Bart, Wim Robberecht, and Ludo Van Den Bosch. 2019. “RNA Toxicity in Non-coding Repeat Expansion Disorders.” *The EMBO Journal*, November, 1–23. https://doi.org/10.15252/embj.2018101112.

Takao, Keizo, and Tsuyoshi Miyakawa. 2006. “Light/Dark Transition Test for Mice.” *Journal of Visualized Experiments*, no. 1 (November): 1–3. https://doi.org/10.3791/104.

Tanaka, Motomasa, Yoko Machida, Sanyong Niu, Tetsurou Ikeda, Nihar R. Jana, Hiroshi Doi, Masaru Kurosawa, Munenori Nekooki, and Nobuyuki Nukina. 2004. “Trehalose Alleviates Polyglutamine-Mediated Pathology in a Mouse Model of Huntington Disease.” *Nature Medicine* 10 (2): 148–54. https://doi.org/10.1038/nm985.

Tanji, Kunikazu, Yasuo Miki, Atsushi Maruyama, Junsei Mimura, Tomoh Matsumiya, Fumiaki Mori, Tadaatsu Imaizumi, Ken Itoh, and Koichi Wakabayashi. 2015. “Trehalose Intake

Induces Chaperone Molecules along with Autophagy in a Mouse Model of Lewy Body Disease.” *Biochemical and Biophysical Research Communications* 465 (4): 746–52. https://doi.org/10.1016/j.bbrc.2015.08.076.

Tassone, Flora, John Adams, Elizabeth M. Berry-Kravis, Susannah S. Cohen, Alfredo Brusco, Maureen A. Leehey, Lexin Li, Randi J. Hagerman, and Paul J. Hagerman. 2007. “CGG Repeat Length Correlates with Age of Onset of Motor Signs of the Fragile X-Associated Tremor/Ataxia Syndrome (FXTAS).” *American Journal of Medical Genetics Part B: Neuropsychiatric Genetics* 144B (4): 566–69. https://doi.org/10.1002/ajmg.b.30482.

Tassone, Flora, Claudia M Greco, Michael R Hunsaker, Andreea L Seritan, R. F. Berman, Louise W Gane, Sebastien Jacquemont, et al. 2012. “Neuropathological, Clinical and Molecular Pathology in Female Fragile X Premutation Carriers with and without FXTAS.” *Genes, Brain and Behavior* 11 (5): 577–85. https://doi.org/10.1111/j.1601-183X.2012.00779.x.

Tassone, Flora, Christine Iwahashi, and Paul J. Hagerman. 2004. “FMR1 RNA within the Intranuclear Inclusions of Fragile X-Associated Tremor/Ataxia Syndrome (FXTAS).” *RNA Biology* 1 (2): 103–5. https://doi.org/10.4161/rna.1.2.1035.

Taylor, Tonya N., James G. Greene, and Gary W. Miller. 2010. “Behavioral Phenotyping of Mouse Models of Parkinson’s Disease.” *Behavioural Brain Research* 211 (1): 1–10. https://doi.org/10.1016/j.bbr.2010.03.004.

Thorburn, Andrew. 2018. “Autophagy and Disease.” *Journal of Biological Chemistry* 293 (15): 5425–30. https://doi.org/10.1074/jbc.R117.810739.

Todd, Peter K., Seok Yoon Oh, Amy Krans, Fang He, Chantal Sellier, Michelle Frazer, Abigail J. Renoux, et al. 2013. “CGG Repeat-Associated Translation Mediates Neurodegeneration in Fragile X Tremor Ataxia Syndrome.” *Neuron* 78 (3): 440–55. https://doi.org/10.1016/j.neuron.2013.03.026.

Tran, Tuan, Jessica L. Childs-Disney, Biao Liu, Lirui Guan, Suzanne Rzuczek, and Matthew D. Disney. 2014. “Targeting the r(CGG) Repeats That Cause FXTAS with Modularly Assembled Small Molecules and Oligonucleotides.” *ACS Chemical Biology* 9 (4): 904–12. https://doi.org/10.1021/cb400875u.

Uhlen, M., Linn Fagerberg, B. M. Hallstrom, Cecilia Lindskog, Per Oksvold, Adil Mardinoglu, A. Sivertsson, et al. 2015. “Tissue-Based Map of the Human Proteome.” *Science* 347 (6220): 1260419–1260419. https://doi.org/10.1126/science.1260419.

Valsamis, Bridget, and Susanne Schmid. 2011. “Habituation and Prepulse Inhibition of Acoustic Startle in Rodents.” *Journal of Visualized Experiments*, no. 55 (September): 1–10. https://doi.org/10.3791/3446.

Volianskis, Arturas, Neil Bannister, Valerie J. Collett, Mark W. Irvine, Daniel T. Monaghan, Stephen M. Fitzjohn, Morten S. Jensen, David E. Jane, and Graham L. Collingridge. 2013. “Different NMDA Receptor Subtypes Mediate Induction of Long-Term Potentiation and Two Forms of Short-Term Potentiation at CA1 Synapses in Rat Hippocampus in Vitro.” *The Journal of Physiology* 591 (4): 955–72. https://doi.org/10.1113/jphysiol.2012.247296.

Volianskis, Arturas, and Morten S. Jensen. 2003. “Transient and Sustained Types of Long-Term Potentiation in the CA1 Area of the Rat Hippocampus.” *The Journal of Physiology* 550 (2): 459–92. https://doi.org/10.1113/jphysiol.2003.044214.

Vuillermot, Stéphanie, Joram Feldon, and Urs Meyer. 2011. “Relationship between Sensorimotor Gating Deficits and Dopaminergic Neuroanatomy in Nurr1-Deficient Mice.” *Experimental Neurology* 232 (1): 22–32. https://doi.org/10.1016/j.expneurol.2011.07.008.

Waguri, Satoshi, and Masaaki Komatsu. 2009. “Biochemical and Morphological Detection of Inclusion Bodies in Autophagy-Deficient Mice.” In *Methods in Enzymology*, 1st ed., 453:181–96. Elsevier Inc. https://doi.org/10.1016/S0076-6879(08)04009-3.

Wan, W. Brad, and Punit P. Seth. 2016. “The Medicinal Chemistry of Therapeutic Oligonucleotides.” *Journal of Medicinal Chemistry* 59 (21): 9645–67. https://doi.org/10.1021/acs.jmedchem.6b00551.

Wang, J. Y., A. M. Trivedi, N. R. Carrillo, J. Yang, A. Schneider, C. Giulivi, P. Adams, et al. 2017. “Open-Label Allopregnanolone Treatment of Men with Fragile X-Associated Tremor/Ataxia Syndrome.” *Neurotherapeutics* 14 (4): 1073–83. https://doi.org/10.1007/s13311-017-0555-6.

Wang, Xiao-Hong, Jin-Chen Yang, Robert Soohoo, Devyn Cotter, Mei Yuan, Jiangyi Xia, Shuja Yaqub, et al. 2018. “Cognitive Deficits and Associated ERP N400 Abnormalities in FXTAS With Parkinsonism.” *Frontiers in Genetics* 9 (SEP): 1–9. https://doi.org/10.3389/fgene.2018.00327.

Weinstein, Jodi J., Muhammad O. Chohan, Mark Slifstein, Lawrence S. Kegeles, Holly Moore, and Anissa Abi-Dargham. 2017. “Pathway-Specific Dopamine Abnormalities in Schizophrenia.” *Biological Psychiatry* 81 (1): 31–42. https://doi.org/10.1016/j.biopsych.2016.03.2104.

Wenzel, H. Jürgen, Karl D. Murray, Saif N. Haify, Michael R. Hunsaker, Jared J. Schwartzer, Kyoungmi Kim, Albert R. La Spada, et al. 2019. “Astroglial-Targeted Expression of the Fragile X CGG Repeat Premutation in Mice Yields RAN Translation, Motor Deficits and Possible Evidence for Cell-to-Cell Propagation of FXTAS Pathology.” *Acta Neuropathologica Communications* 7 (1): 27. https://doi.org/10.1186/s40478-019-0677-7.

Westergard, Thomas, Brigid K. Jensen, Xinmei Wen, Jingli Cai, Elizabeth Kropf, Lorraine Iacovitti, Piera Pasinelli, and Davide Trotti. 2016. “Cell-to-Cell Transmission of Dipeptide Repeat Proteins Linked to C9orf72 -ALS/FTD.” *Cell Reports* 17 (3): 645–52. https://doi.org/10.1016/j.celrep.2016.09.032.

Willemsen, R, J Levenga, and BA Oostra. 2011. “CGG Repeat in the FMR1 Gene: Size Matters.” *Clinical Genetics* 80 (3): 214–25. https://doi.org/10.1111/j.1399-0004.2011.01723.x.

Wooten, Marie W., Xiao Hu, J. Ramesh Babu, M. Lamar Seibenhener, Thangiah Geetha, Michael G. Paine, and Michael C. Wooten. 2006. “Signaling, Polyubiquitination, Trafficking, and Inclusions: Sequestosome 1/P62’s Role in Neurodegenerative Disease.” *Journal of Biomedicine and Biotechnology* 2006: 1–12. https://doi.org/10.1155/JBB/2006/62079.

Yang, Wang-Yong, Henry D. Wilson, Sai Pradeep Velagapudi, and Matthew D. Disney. 2015. “Inhibition of Non-ATG Translational Events in Cells via Covalent Small Molecules Targeting RNA.” *Journal of the American Chemical Society* 137 (16): 5336–45. https://doi.org/10.1021/ja507448y.

Yang, Ying, and Jian-Zhi Wang. 2017. “From Structure to Behavior in Basolateral Amygdala-Hippocampus Circuits.” *Frontiers in Neural Circuits* 11 (October): 1–8. https://doi.org/10.3389/fncir.2017.00086.

Yrigollen, Carolyn, and Beverly Davidson. 2019. “CRISPR to the Rescue: Advances in Gene Editing for the FMR1 Gene.” *Brain Sciences* 9 (1): 17. https://doi.org/10.3390/brainsci9010017.

Yrigollen, Carolyn M., Loreto Martorell, Blythe Durbin-Johnson, Montserrat Naudo, Jordi Genoves, Alessandra Murgia, Roberta Polli, et al. 2014. “AGG Interruptions and Maternal Age Affect FMR1 CGG Repeat Allele Stability during Transmission.” *Journal of*

Neurodevelopmental Disorders 6 (1): 20. https://doi.org/10.1186/1866-1955-6-24.

Zalfa, Francesca, Boris Eleuteri, Kirsten S. Dickson, Valentina Mercaldo, Silvia De Rubeis, Alessandra di Penta, Elisabetta Tabolacci, et al. 2007. "A New Function for the Fragile X Mental Retardation Protein in Regulation of PSD-95 MRNA Stability." *Nature Neuroscience* 10 (5): 578–87. https://doi.org/10.1038/nn1893.

Zeniya, Satoshi, Hiroya Kuwahara, Kaiichi Daizo, Akihiro Watari, Masuo Kondoh, Kie Yoshida-Tanaka, Hidetoshi Kaburagi, et al. 2018. "Angubindin-1 Opens the Blood–Brain Barrier in Vivo for Delivery of Antisense Oligonucleotide to the Central Nervous System." *Journal of Controlled Release* 283 (May): 126–34. https://doi.org/10.1016/j.jconrel.2018.05.010.

Zhao, Xiao-Nan, and Karen Usdin. 2016. "Ups and Downs: Mechanisms of Repeat Instability in the Fragile X-Related Disorders." *Genes* 7 (9): 70. https://doi.org/10.3390/genes7090070.

Zoetmulder, Marielle, Heidi B. Biernat, Miki Nikolic, Lise Korbo, Lars Friberg, and Poul J. Jennum. 2014. "Prepulse Inhibition Is Associated with Attention, Processing Speed, and 123I-FP-CIT SPECT in Parkinson's Disease." *Journal of Parkinson's Disease* 4 (1): 77–87. https://doi.org/10.3233/JPD-130307.

Appendix

Table S1.: ANOVA results related to Fig.3.1.

ANOVA results for Figure 3.1.C.	**F (DFn, DFd)**	**P value**
spl x dox	F (3, 66) = 0.8186	P=0.4882
spl	F (1.195, 26.30) = 40.33	P<0.0001
dox	F (1, 22) = 0.2033	P=0.6565
Subject	F (22, 66) = 5.533	P<0.0001
ANOVA results for Figure 3.1.D.	**F (DFn, DFd)**	**P value**
spl x dox	F (3, 66) = 0.3709	P=0.7742
spl	F (1.716, 37.75) = 24.48	P<0.0001
dox	F (1, 22) = 4.992	P=0.0359
Subject	F (22, 66) = 4.445	P<0.0001

Table S2.: ANOVA results related to Fig.3.2.

ANOVA results for Figure 3.2.A.	**F (DFn, DFd)**	**P value**
spl x dox	F (3, 42) = 0.7802	P=0.5117
spl	F (1.556, 21.78) = 29.76	P<0.0001
dox	F (1, 14) = 0.5299	P=0.4786
Subject	F (14, 42) = 4.298	P=0.0001
ANOVA results for Figure 3.2.B.	**F (DFn, DFd)**	**P value**
spl x dox	F (3, 42) = 1.395	P=0.2576
spl	F (1.350, 18.90) = 19.16	P=0.0001
dox	F (1, 14) = 4.054	P=0.0637
Subject	F (14, 42) = 4.724	P<0.0001
ANOVA results for Figure 3.2.C.	**F (DFn, DFd)**	**P value**
spl x dox	F (3, 60) = 0.4770	P=0.6995
spl	F (1.436, 28.71) = 29.71	P<0.0001
dox	F (1, 20) = 0.001249	P=0.9722
Subject	F (20, 60) = 7.483	P<0.0001
ANOVA results for Figure 3.2.D.	**F (DFn, DFd)**	**P value**
spl x dox	F (3, 60) = 0.1906	P=0.9024
spl	F (1.702, 34.04) = 24.07	P<0.0001
dox	F (1, 20) = 0.2725	P=0.6074
Subject	F (20, 60) = 4.448	P<0.0001

Table S3.: ANOVA results related to Fig.3.3.

ANOVA results for Figure 3.3.D.	**F (DFn, DFd)**	**P value**
time-bin x dox	F (3, 84) = 0.9862	P=0.4034
time-bin	F (2.087, 58.44) = 9.087	P=0.0003
dox	F (1, 28) = 0.7263	P=0.4013
Subject	F (28, 84) = 10.12	P<0.0001
ANOVA results for Figure 3.3.E.	**F (DFn, DFd)**	**P value**
time-bin x dox	F (3, 48) = 3.020	P=0.0387
time-bin	F (2.475, 39.59) = 15.40	P<0.0001
dox	F (1, 16) = 0.1120	P=0.7423
Subject	F (16, 48) = 8.291	P<0.0001

Fisher's LSD

11xCGG.24weDOX- vs 11xCGG.24weDOX+	**t**	**P value**
5	1.869	0.0801
10	0.09666	0.9244
15	0.3617	0.7225
20	0.3861	0.7045

ANOVA results for Figure 3.3.F.	**F (DFn, DFd)**	**P value**
time-bin x dox	F (3, 84) = 0.6274	P=0.5993
time-bin	F (2.313, 64.77) = 5.226	P=0.0056
dox	F (1, 28) = 2.201	P=0.1491
Subject	F (28, 84) = 3.595	P<0.0001

ANOVA results for Figure 3.3.G.	**F (DFn, DFd)**	**P value**
time-bin x dox	F (3, 48) = 0.3238	P=0.8081
time-bin	F (2.365, 37.84) = 0.7126	P=0.5191
dox	F (1, 16) = 4.158	P=0.0583
Subject	F (16, 48) = 1.624	P=0.0984

Table S4.: ANOVA results related to Fig.3.9.

ANOVA results for Figure 3.9.C.	**F (DFn, DFd)**	**P value**
trial (day) x dox	F (2, 38) = 0.8390	P=0.4400
trial (day)	F (1.623, 30.83) = 10.94	P=0.0006
dox	F (1, 19) = 3.329	P=0.0838
Subject	F (19, 38) = 2.818	P=0.0032

ANOVA results for Figure 3.9.D.	**F (DFn, DFd)**	**P value**
rpm x dox	F (4, 76) = 1.658	P=0.1685
rpm	F (2.671, 50.74) = 1.778	P=0.1686
dox	F (1, 19) = 0.1859	P=0.6712
Subject	F (19, 76) = 1.155	P=0.3179

Table S5.: ANOVA results related to Fig.3.12.

ANOVA results for Figure 3.12.A.	**F (DFn, DFd)**	**P value**
stimulation intensity x dox	F (8, 408) = 6.736	P<0.0001
stimulation intensity	F (2.105, 107.3) = 107.0	P<0.0001
dox	F (1, 51) = 5.030	P=0.0293
Subject	F (51, 408) = 13.34	P<0.0001

Fisher's LSD

early.dox- vs early.dox+	**t**	**P value**
10	1.576	0.122
20	1.353	0.183
30	0.2223	0.825
40	1.334	0.1902
50	1.511	0.1406
75	2.367	0.0245
100	2.342	0.0257
150	2.719	0.0104
200	2.544	0.0157

ANOVA results for Figure 3.12.B.	F (DFn, DFd)	P value
stimulation intensity x dox	F (8, 384) = 3.944	P=0.0002

stimulation intensity	F (2.201, 105.7) = 83.48	P<0.0001
dox	F (1, 48) = 0.2909	P=0.5921
Subject	F (48, 384) = 15.18	P<0.0001
Fisher's LSD		
early.dox-.WO vs early.dox+.WO	**t**	**P value**
10	0.6779	0.502
20	1.124	0.2686
30	1.43	0.1616
40	0.4052	0.6872
50	0.2521	0.8021
75	0.4246	0.673
100	0.9759	0.3341
150	1.567	0.1237
200	2.001	0.0511
ANOVA results for Figure 3.12.C.	**F (DFn, DFd)**	**P value**
time (min) x dox	F (19, 494) = 1.616	P=0.0481
time (min)	F (2.683, 69.76) = 7.053	P=0.0005
dox	F (1, 26) = 0.08049	P=0.7789
Subject	F (26, 494) = 35.45	P<0.0001
Fisher's LSD		
early.dox- vs early.dox+	**t**	**P value**
2	1.478	0.152
4	0.5387	0.5953
6	0.4236	0.6754
8	0.8576	0.3991
10	0.1471	0.8843
12	0.5201	0.6076
14	0.3629	0.7197
16	0.4035	0.6901
18	0.361	0.7212
20	1.145	0.2625
22	0.233	0.8176
24	0.4196	0.6782
26	0.1748	0.8626
28	0.5708	0.5731
30	0.2326	0.8179
32	0.3227	0.7495
34	0.8337	0.4121
36	0.5959	0.5564
38	0.6403	0.5276
40	0.906	0.3734
ANOVA results for Figure 3.12.D.	**F (DFn, DFd)**	**P value**
time (min) x dox	F (19, 532) = 2.442	P=0.0006
time (min)	F (2.191, 61.36) = 1.931	P=0.1498
dox	F (1, 28) = 0.3540	P=0.5566
Subject	F (28, 532) = 33.28	P<0.0001
Fisher's LSD		

early.dox-.WO vs early.dox+.WO	**t**	**P value**
2	1.505	0.1458
4	0.08516	0.9328
6	0.3614	0.7205
8	0.341	0.7358
10	0.03789	0.9701
12	0.2863	0.7768
14	0.4564	0.6522
16	0.6392	0.5292
18	0.8325	0.4132
20	0.1988	0.8441
22	0.6757	0.5054
24	0.6287	0.5347
26	0.8714	0.391
28	1.03	0.3124
30	1.283	0.2116
32	0.9997	0.3268
34	1.819	0.0807
36	1.507	0.1442
38	1.119	0.2737
40	1.219	0.236

Table S6.: ANOVA results related to Fig.3.13.

ANOVA results for Figure 3.13.A.	**F (DFn, DFd)**	**P value**
stimulation intensity x dox	F (4, 380) = 3.685	P=0.0059
stimulation intensity	F (1.559, 148.1) = 243.7	P<0.0001
dox	F (1, 95) = 10.77	P=0.0014
Subject	F (95, 380) = 23.28	P<0.0001
Fisher's LSD		
early.dox- vs early.dox+	**t**	**P value**
10	3.187	0.0021
20	3.31	0.0014
30	3.173	0.0021
40	3.259	0.0016
50	3.366	0.0011
ANOVA results for Figure 3.13.B.	**F (DFn, DFd)**	**P value**
stimulation intensity x dox	F (4, 272) = 0.4581	P=0.7665
stimulation intensity	F (1.747, 118.8) = 228.8	P<0.0001
dox	F (1, 68) = 0.1258	P=0.7240
Subject	F (68, 272) = 33.60	P<0.0001
ANOVA results for Figure 3.13.C.	F (DFn, DFd)	P value
time (min) x dox	F (19, 437) = 1.779	P=0.0229
time (min)	F (2.121, 48.77) = 16.15	P<0.0001
dox	F (1, 23) = 2.976	P=0.0979
Subject	F (23, 437) = 194.9	P<0.0001
Fisher's LSD		
early.dox- vs early.dox+	**t**	**P value**

2	2.808	0.014
4	2.23	0.0422
6	1.961	0.0676
8	1.753	0.0976
10	1.719	0.1041
12	1.539	0.1416
14	1.421	0.1731
16	1.515	0.1501
18	1.576	0.1323
20	1.383	0.1825
22	1.465	0.1614
24	1.359	0.1907
26	1.626	0.121
28	1.646	0.1193
30	1.339	0.1968
32	1.422	0.1718
34	1.403	0.1772
36	1.274	0.2182
38	1.609	0.1256
40	1.288	0.2129
ANOVA results for Figure 3.13.D.	**F (DFn, DFd)**	**P value**
time (min) x dox	F (19, 323) = 0.9262	P=0.5505
time (min)	F (2.700, 45.90) = 8.533	P=0.0002
dox	F (1, 17) = 0.9310	P=0.3481
Subject	F (17, 323) = 155.7	P<0.0001

Table S7.: ANOVA results related to Fig.3.15.

ANOVA results for Figure 3.15.B.	**F (DFn, DFd)**	**P value**
Interaction	F (1, 28) = 0.01815	P=0.8938
treh	F (1, 28) = 5.655	P=0.0245
dox	F (1, 28) = 0.02427	P=0.8773

Table S8.: ANOVA results related to Fig.3.16.

ANOVA results for Figure 3.16.A.	**F (DFn, DFd)**	**P value**
trial number	F (2.297, 87.29) = 20.39	P<0.0001
dox	F (1, 38) = 2.506	P=0.1217
treh	F (1, 38) = 2.098	P=0.1557
trial number x dox	F (3, 114) = 3.137	P=0.0282
trial number x treh	F (3, 114) = 1.254	P=0.2935
dox x treh	F (1, 38) = 0.1913	P=0.6643
trial number x dox x treh	F (3, 114) = 1.391	P=0.2492
Fisher's LSD		
	t	**P value**
T1:dox-.treh- vs. T2:dox-.treh+	2.817	0.0201
T1:dox-.treh- vs. T3:dox-.treh-	2.498	0.034
T1:dox-.treh- vs. T3:dox+.treh+	2.74	0.0226
T1:dox-.treh- vs. T4:dox-.treh-	2.817	0.0201
T1:dox-.treh- vs. T4:dox-.treh+	2.423	0.0347

T1:dox-.treh- vs. T4:dox+.treh-	2.688	0.0243
T1:dox-.treh- vs. T4:dox+.treh+	2.485	0.0328
T1:dox-.treh+ vs. T1:dox+.treh-	2.867	0.0105
T1:dox+.treh- vs. T2:dox-.treh+	4.825	0.0007
T1:dox+.treh- vs. T2:dox+.treh-	3.422	0.0065
T1:dox+.treh- vs. T2:dox+.treh+	2.757	0.0124
T1:dox+.treh- vs. T3:dox-.treh-	4.517	0.0009
T1:dox+.treh- vs. T3:dox-.treh+	3.931	0.0016
T1:dox+.treh- vs. T3:dox+.treh-	3.72	0.004
T1:dox+.treh- vs. T3:dox+.treh+	4.744	0.0008
T1:dox+.treh- vs. T4:dox-.treh-	4.825	0.0007
T1:dox+.treh- vs. T4:dox-.treh+	4.349	0.001
T1:dox+.treh- vs. T4:dox+.treh-	4.833	0.0007
T1:dox+.treh- vs. T4:dox+.treh+	4.452	0.001
T1:dox+.treh+ vs. T2:dox-.treh+	3.417	0.0066
T1:dox+.treh+ vs. T2:dox+.treh+	2.49	0.032
T1:dox+.treh+ vs. T3:dox-.treh-	3.168	0.0094
T1:dox+.treh+ vs. T3:dox-.treh+	2.732	0.0173
T1:dox+.treh+ vs. T3:dox+.treh-	2.123	0.0481
T1:dox+.treh+ vs. T3:dox+.treh+	3.405	0.0067
T1:dox+.treh+ vs. T4:dox-.treh-	3.417	0.0066
T1:dox+.treh+ vs. T4:dox-.treh+	3.053	0.0106
T1:dox+.treh+ vs. T4:dox+.treh-	3.301	0.0078
T1:dox+.treh+ vs. T4:dox+.treh+	3.348	0.0074
T2:dox-.treh- vs. T2:dox-.treh+	2.29	0.0478
T2:dox-.treh- vs. T4:dox-.treh-	2.29	0.0478

ANOVA results for Figure 3.16.B.	**F (DFn, DFd)**	**P value**
rpm	F (2.660, 101.1) = 8.948	P<0.0001
dox	F (1, 38) = 26.39	P<0.0001
treh	F (1, 38) = 6.482	P=0.0151
rpm x dox	F (4, 152) = 2.860	P=0.0254
rpm x treh	F (4, 152) = 1.298	P=0.2735
dox x treh	F (1, 38) = 6.521	P=0.0148
rpm x dox x treh	F (4, 152) = 1.085	P=0.3660

Fisher's LSD

	t	**P value**
15:dox-.treh- vs. 31:dox+.treh-	3.357	0.0073
15:dox-.treh- vs. 36:dox+.treh-	3.537	0.0054
15:dox-.treh- vs. 40:dox-.treh+	2.943	0.0164
15:dox-.treh- vs. 40:dox+.treh-	5.8	0.0002
15:dox-.treh- vs. 40:dox+.treh+	2.532	0.0298
15:dox-.treh+ vs. 31:dox+.treh-	3.357	0.0073
15:dox-.treh+ vs. 36:dox+.treh-	3.537	0.0054
15:dox-.treh+ vs. 40:dox-.treh+	2.943	0.0164
15:dox-.treh+ vs. 40:dox+.treh-	5.8	0.0002
15:dox-.treh+ vs. 40:dox+.treh+	2.532	0.0298
15:dox+.treh- vs. 31:dox+.treh-	3.318	0.0078

15:dox+.treh- vs. 36:dox+.treh-	3.154	0.0103
15:dox+.treh- vs. 40:dox+.treh-	5.204	0.0004
15:dox+.treh+ vs. 31:dox+.treh-	3.202	0.0091
15:dox+.treh+ vs. 36:dox+.treh-	3.4	0.0065
15:dox+.treh+ vs. 40:dox-.treh+	2.312	0.039
15:dox+.treh+ vs. 40:dox+.treh-	5.568	0.0002
15:dox+.treh+ vs. 40:dox+.treh+	2.275	0.0462
24:dox-.treh- vs. 31:dox+.treh-	3.345	0.0074
24:dox-.treh- vs. 36:dox+.treh-	3.527	0.0055
24:dox-.treh- vs. 40:dox-.treh+	2.902	0.0175
24:dox-.treh- vs. 40:dox+.treh-	5.785	0.0002
24:dox-.treh- vs. 40:dox+.treh+	2.518	0.0305
24:dox-.treh+ vs. 31:dox+.treh-	2.989	0.0125
24:dox-.treh+ vs. 36:dox+.treh-	3.212	0.0086
24:dox-.treh+ vs. 40:dox-.treh+	2.707	0.0241
24:dox-.treh+ vs. 40:dox+.treh-	5.251	0.0003
24:dox+.treh- vs. 36:dox+.treh-	2.887	0.0162
24:dox+.treh- vs. 40:dox+.treh-	2.424	0.0358
24:dox+.treh+ vs. 31:dox+.treh-	2.189	0.0446
24:dox+.treh+ vs. 36:dox+.treh-	2.49	0.0257
24:dox+.treh+ vs. 40:dox+.treh-	3.922	0.0011
31:dox-.treh- vs. 31:dox+.treh-	3.082	0.011
31:dox-.treh- vs. 36:dox+.treh-	3.294	0.0077
31:dox-.treh- vs. 40:dox+.treh-	5.401	0.0002
31:dox-.treh- vs. 40:dox+.treh+	2.222	0.0489
31:dox-.treh+ vs. 31:dox+.treh-	3.357	0.0073
31:dox-.treh+ vs. 36:dox+.treh-	3.537	0.0054
31:dox-.treh+ vs. 40:dox-.treh+	2.943	0.0164
31:dox-.treh+ vs. 40:dox+.treh-	5.8	0.0002
31:dox-.treh+ vs. 40:dox+.treh+	2.532	0.0298
31:dox+.treh- vs. 36:dox-.treh-	3.113	0.0102
31:dox+.treh- vs. 36:dox-.treh+	2.587	0.0242
31:dox+.treh- vs. 40:dox-.treh+	2.367	0.0359
31:dox+.treh+ vs. 40:dox+.treh-	2.916	0.0086
36:dox-.treh- vs. 36:dox+.treh-	3.322	0.0072
36:dox-.treh- vs. 40:dox+.treh-	5.416	0.0002
36:dox-.treh- vs. 40:dox+.treh+	2.26	0.0452
36:dox-.treh+ vs. 36:dox+.treh-	2.852	0.0153
36:dox-.treh+ vs. 40:dox+.treh-	4.671	0.0005
36:dox+.treh- vs. 36:dox+.treh+	2.192	0.0448
36:dox+.treh- vs. 40:dox-.treh+	2.655	0.0218
36:dox+.treh+ vs. 40:dox+.treh-	3.496	0.0026
40:dox-.treh- vs. 40:dox+.treh-	2.973	0.0078
40:dox-.treh+ vs. 40:dox+.treh-	4.395	0.0008
ANOVA results for Figure 3.16.C.	**F (DFn, DFd)**	**P value**
Interaction	F (1, 38) = 7.622	P=0.0088
dox	F (1, 38) = 24.77	P<0.0001

treh	F (1, 38) = 10.66	P=0.0023
Fisher's LSD		
	t	**P value**
dox-:treh- vs. dox-:treh+	0.3477	0.73
dox-:treh- vs. dox+:treh-	5.472	<0.0001
dox-:treh- vs. dox+:treh+	1.211	0.2333
dox-:treh+ vs. dox+:treh-	5.828	<0.0001
dox-:treh+ vs. dox+:treh+	1.567	0.1254
dox+:treh- vs. dox+:treh+	4.366	<0.0001
ANOVA results for Figure 3.16.D.	F (DFn, DFd)	P value
Interaction	F (1, 38) = 0.002164	P=0.9631
dox	F (1, 38) = 2.352	P=0.1334
treh	F (1, 38) = 0.9545	P=0.3348

Table S9.: ANOVA results related to Fig.3.18.

ANOVA results for Figure 3.18.B.	**F (DFn, DFd)**	**P value**
Interaction	F (1, 41) = 0.2028	P=0.6548
treh	F (1, 41) = 0.2659	P=0.6089
dox	F (1, 41) = 0.9365	P=0.3389
ANOVA results for Figure 3.18.C.	**F (DFn, DFd)**	**P value**
Interaction	F (1, 41) = 0.6476	P=0.4256
treh	F (1, 41) = 0.1568	P=0.6942
dox	F (1, 41) = 1.018	P=0.3188
ANOVA results for Figure 3.18.D.	**F (DFn, DFd)**	**P value**
Interaction	F (1, 41) = 0.3181	P=0.5758
treh	F (1, 41) = 0.004277	P=0.9482
dox	F (1, 41) = 0.01672	P=0.8977
ANOVA results for Figure 3.18.E.	**F (DFn, DFd)**	**P value**
Interaction	F (1, 41) = 0.01218	P=0.9127
treh	F (1, 41) = 0.7212	P=0.4007
dox	F (1, 41) = 3.465	P=0.0699
ANOVA results for Figure 3.18.F.	**F (DFn, DFd)**	**P value**
Interaction	F (1, 41) = 0.6245	P=0.4339
treh	F (1, 41) = 2.665	P=0.1102
dox	F (1, 41) = 0.6407	P=0.4281
ANOVA results for Figure 3.18.G.	**F (DFn, DFd)**	**P value**
Interaction	F (1, 41) = 2.658	P=0.1107
treh	F (1, 41) = 0.8086	P=0.3738
dox	F (1, 41) = 1.004	P=0.3221

Table S10.: ANOVA results related to Fig.3.19.

ANOVA results for Figure 3.19.A.	**F (DFn, DFd)**	**P value**
Interaction	F (1, 41) = 0.6258	P=0.4334
treh	F (1, 41) = 0.08333	P=0.7743
dox	F (1, 41) = 2.898	P=0.0963
ANOVA results for Figure 3.19.B.	**F (DFn, DFd)**	**P value**
Interaction	F (1, 40) = 0.1471	P=0.7033
treh	F (1, 40) = 0.004864	P=0.9447

dox	F (1, 40) = 5.115	P=0.0292
ANOVA results for Figure 3.19.C.	**F (DFn, DFd)**	**P value**
time-bin	F (1.940, 79.56) = 11.19	P<0.0001
dox	F (1, 41) = 1.150	P=0.2899
treh	F (1, 41) = 3.692	P=0.0616
time-bin x dox	F (3, 123) = 3.758	P=0.0127
time-bin x treh	F (3, 123) = 0.6694	P=0.5724
dox x treh	F (1, 41) = 8.551	P=0.0056
time-bin x dox x treh	F (3, 123) = 1.654	P=0.1805
Fisher's LSD		
	t	**P value**
5:dox-.treh- vs. 5:dox-.treh+	2.245	0.0469
5:dox-.treh- vs. 5:dox+.treh-	2.652	0.0236
5:dox-.treh- vs. 10:dox-.treh+	2.801	0.0183
5:dox-.treh- vs. 10:dox+.treh-	2.505	0.0274
5:dox-.treh- vs. 15:dox-.treh+	3.378	0.0066
5:dox-.treh- vs. 15:dox+.treh-	2.767	0.0171
5:dox-.treh- vs. 15:dox+.treh+	3.055	0.0118
5:dox-.treh- vs. 20:dox-.treh-	3.272	0.0096
5:dox-.treh- vs. 20:dox-.treh+	3.569	0.0046
5:dox-.treh- vs. 20:dox+.treh-	2.906	0.0137
5:dox-.treh- vs. 20:dox+.treh+	2.702	0.0207
5:dox-.treh+ vs. 15:dox-.treh+	3.845	0.0032
5:dox-.treh+ vs. 20:dox-.treh+	5.77	0.0002
5:dox+.treh- vs. 20:dox-.treh+	2.416	0.0255
5:dox+.treh+ vs. 15:dox-.treh+	2.566	0.0183
5:dox+.treh+ vs. 20:dox-.treh+	2.93	0.0081
10:dox-.treh- vs. 10:dox-.treh+	2.29	0.039
10:dox-.treh- vs. 15:dox-.treh+	3.262	0.0058
10:dox-.treh- vs. 15:dox+.treh-	2.169	0.0444
10:dox-.treh- vs. 15:dox+.treh+	2.729	0.017
10:dox-.treh- vs. 20:dox-.treh-	2.592	0.0291
10:dox-.treh- vs. 20:dox-.treh+	3.566	0.003
10:dox-.treh- vs. 20:dox+.treh-	2.409	0.0281
10:dox-.treh+ vs. 20:dox-.treh+	2.472	0.033
10:dox+.treh+ vs. 15:dox-.treh+	2.254	0.036
10:dox+.treh+ vs. 15:dox+.treh+	2.643	0.0215
10:dox+.treh+ vs. 20:dox-.treh+	2.601	0.0172
15:dox-.treh- vs. 20:dox-.treh+	2.431	0.0265
ANOVA results for Figure 3.19.D.	**F (DFn, DFd)**	**P value**
time-bin	F (2.674, 109.6) = 49.00	P<0.0001
dox	F (1, 41) = 1.813	P=0.1855
treh	F (1, 41) = 0.4517	P=0.5053
time-bin x dox	F (3, 123) = 1.878	P=0.1368
time-bin x treh	F (3, 123) = 0.6387	P=0.5915
dox x treh	F (1, 41) = 0.8463	P=0.3630
time-bin x dox x treh	F (3, 123) = 0.1866	P=0.9053

Table S11.: ANOVA results related to Fig.3.20.

ANOVA results for Figure 3.20.B.	**F (DFn, DFd)**	**P value**
<u>pre-training</u>		
Interaction	F (1, 41) = 2.413	P=0.1280
treh	F (1, 41) = 0.001156	P=0.9730
dox	F (1, 41) = 1.536	P=0.2223
<u>post-training</u>		
Interaction	F (1, 41) = 2.593	P=0.1150
treh	F (1, 41) = 1.338	P=0.2540
dox	F (1, 41) = 1.273	P=0.2658
ANOVA results for Figure 3.20.C.	**F (DFn, DFd)**	**P value**
<u>shock context</u>		
Interaction	F (1, 41) = 3.528	P=0.0674
treh	F (1, 41) = 0.1143	P=0.7370
dox	F (1, 41) = 0.1961	P=0.6602
<u>neutral context</u>		
Interaction	F (1, 41) = 3.709	P=0.0611
treh	F (1, 41) = 0.0003970	P=0.9842
dox	F (1, 41) = 0.5226	P=0.4738
ANOVA results for Figure 3.20.D.	**F (DFn, DFd)**	**P value**
<u>CS+</u>		
Interaction	F (1, 41) = 0.1195	P=0.7314
treh	F (1, 41) = 1.909	P=0.1746
dox	F (1, 41) = 0.004162	P=0.9489
<u>trace</u>		
Interaction	F (1, 41) = 0.03538	P=0.8517
treh	F (1, 41) = 0.7053	P=0.4059
dox	F (1, 41) = 0.2257	P=0.6373

Table S12.: ANOVA results related to Fig.3.21.

ANOVA results for Figure 3.21.B.	**F (DFn, DFd)**	**P value**
trial number	F (2.726, 92.68) = 19.69	P<0.0001
dox	F (1, 34) = 2.649	P=0.1128
treh	F (1, 34) = 1.472	P=0.2334
trial number x dox	F (3, 102) = 0.3602	P=0.7819
trial number x treh	F (3, 102) = 1.378	P=0.2539
dox x treh	F (1, 34) = 0.04588	P=0.8317
trial number x dox x treh	F (3, 102) = 0.3379	P=0.7979
ANOVA results for Figure 3.21.C.	**F (DFn, DFd)**	**P value**
rpm	F (3.081, 104.8) = 30.14	P<0.0001
dox	F (1, 34) = 15.56	P=0.0004
treh	F (1, 34) = 0.8237	P=0.3705
rpm x dox	F (4, 136) = 1.894	P=0.1150
rpm x treh	F (4, 136) = 0.4232	P=0.7917
dox x treh	F (1, 34) = 0.02414	P=0.8775
rpm x dox x treh	F (4, 136) = 0.09309	P=0.9845
ANOVA results for Figure 3.21.D.	**F (DFn, DFd)**	**P value**

Interaction	F (1, 34) = 0.4875	P=0.4898
treh	F (1, 34) = 1.011	P=0.3219
dox	F (1, 34) = 10.99	P=0.0022
ANOVA results for Figure 3.21.E.	**F (DFn, DFd)**	**P value**
Interaction	F (1, 34) = 3.629	P=0.0653
treh	F (1, 34) = 1.278	P=0.2662
dox	F (1, 34) = 35.81	P<0.0001

Table S13.: ANOVA results related to Fig.3.22.

ANOVA results for Figure 3.22.A.	**F (DFn, DFd)**	**P value**
Interaction	F (1, 34) = 0.4735	P=0.4960
treh	F (1, 34) = 0.03430	P=0.8542
dox	F (1, 34) = 0.008394	P=0.9275
ANOVA results for Figure 3.22.B.	**F (DFn, DFd)**	**P value**
Interaction	F (1, 34) = 1.077	P=0.3068
treh	F (1, 34) = 1.085	P=0.3050
dox	F (1, 34) = 0.6429	P=0.4282
ANOVA results for Figure 3.22.C.	**F (DFn, DFd)**	**P value**
Interaction	F (1, 34) = 3.009e-006	P=0.9986
treh	F (1, 34) = 0.6121	P=0.4394
dox	F (1, 34) = 0.1192	P=0.7321
ANOVA results for Figure 3.22.D.	**F (DFn, DFd)**	**P value**
Interaction	F (1, 34) = 1.922	P=0.1747
treh	F (1, 34) = 3.743	P=0.0614
dox	F (1, 34) = 0.0009927	P=0.9750
ANOVA resultss for Figure 3.22.E.	**F (DFn, DFd)**	**P value**
Interaction	F (1, 34) = 0.1080	P=0.7445
treh	F (1, 34) = 0.3412	P=0.5630
dox	F (1, 34) = 0.1080	P=0.7445
ANOVA results for Figure 3.22.F.	**F (DFn, DFd)**	**P value**
Interaction	F (1, 34) = 1.164	P=0.2882
treh	F (1, 34) = 0.1674	P=0.6850
dox	F (1, 34) = 0.1788	P=0.6751

Table S14.: ANOVA results related to Fig.3.23.

ANOVA results for Figure 3.23.A.	**F (DFn, DFd)**	**P value**
Interaction	F (1, 34) = 1.773	P=0.1919
treh	F (1, 34) = 0.4375	P=0.5128
dox	F (1, 34) = 12.71	P=0.0011
ANOVA results for Figure 3.23.B.	**F (DFn, DFd)**	**P value**
Interaction	F (1, 34) = 0.1263	P=0.7244
treh	F (1, 34) = 0.002773	P=0.9583
dox	F (1, 34) = 25.96	P<0.0001
ANOVA results for Figure 3.23.C.	**F (DFn, DFd)**	**P value**
time-bin	F (2.568, 87.31) = 6.689	P=0.0008
dox	F (1, 34) = 4.309	P=0.0455
treh	F (1, 34) = 3.219	P=0.0817
time-bin x dox	F (3, 102) = 1.191	P=0.3168

time-bin x treh	F (3, 102) = 0.08224	P=0.9696
dox x treh	F (1, 34) = 0.8175	P=0.3723
time-bin x dox x treh	F (3, 102) = 0.1758	P=0.9126
ANOVA results for Figure 3.23.D.	**F (DFn, DFd)**	**P value**
time-bin	F (2.522, 85.74) = 20.47	P<0.0001
dox	F (1, 34) = 0.0007230	P=0.9787
treh	F (1, 34) = 0.1792	P=0.6747
time-bin x dox	F (3, 102) = 0.8800	P=0.4541
time-bin x treh	F (3, 102) = 0.7900	P=0.5022
dox x treh	F (1, 34) = 0.2742	P=0.6039
time-bin x dox x treh	F (3, 102) = 0.2365	P=0.8707

Table S15.: ANOVA results related to Fig.3.24.

ANOVA results for Figure 3.24.A.	**F (DFn, DFd)**	**P value**
pre-training		
Interaction	F (1, 34) = 0.8414	P=0.3655
treh	F (1, 34) = 0.08704	P=0.7698
dox	F (1, 34) = 1.960	P=0.1706
post-training		
Interaction	F (1, 34) = 0.1814	P=0.6729
treh	F (1, 34) = 0.05361	P=0.8183
dox	F (1, 34) = 0.1932	P=0.6630
ANOVA results for Figure 3.24.B.	**F (DFn, DFd)**	**P value**
shock context		
Interaction	F (1, 34) = 0.01243	P=0.9119
treh	F (1, 34) = 0.5415	P=0.4669
dox	F (1, 34) = 9.333	P=0.0044
neutral context		
Interaction	F (1, 34) = 1.880	P=0.1793
treh	F (1, 34) = 0.04200	P=0.8388
dox	F (1, 34) = 7.098	P=0.0117
ANOVA results for Figure 3.24.C.	**F (DFn, DFd)**	**P value**
CS+		
Interaction	F (1, 34) = 1.742	P=0.1958
treh	F (1, 34) = 0.08921	P=0.7670
dox	F (1, 34) = 0.1498	P=0.7011
trace		
Interaction	F (1, 34) = 1.205	P=0.2801
treh	F (1, 34) = 1.939	P=0.1728
dox	F (1, 34) = 2.874	P=0.0992

Table S16.: ANOVA results related to Fig.3.25.

ANOVA results for Figure 3.25.A.	**F (DFn, DFd)**	**P value**
SPL	F (1.294, 43.98) = 41.05	P<0.0001
dox	F (1, 34) = 0.04534	P=0.8326
treh	F (1, 34) = 0.4762	P=0.4948
SPL x dox	F (3, 102) = 1.859	P=0.1413
SPL x treh	F (3, 102) = 0.4956	P=0.6862

dox x treh	F (1, 34) = 0.07753	P=0.7824
SPL x dox x treh	F (3, 102) = 0.3643	P=0.7789
ANOVA results for Figure 3.25.B.	**F (DFn, DFd)**	**P value**
SPL	F (1.666, 56.66) = 47.86	P<0.0001
dox	F (1, 34) = 0.1825	P=0.6719
treh	F (1, 34) = 0.2694	P=0.6071
SPL x dox	F (3, 102) = 0.7174	P=0.5438
SPL x treh	F (3, 102) = 5.045	P=0.0027
dox x treh	F (1, 34) = 0.07794	P=0.7818
SPL x dox x treh	F (3, 102) = 1.086	P=0.3586
Fisher's LSD		
	t	**P value**
70:dox-.WOtreh- vs. 70:dox-.WOtreh+	2.145	0.0473
70:dox-.WOtreh- vs. 85:dox-.WOtreh+	3.061	0.0108
70:dox-.WOtreh- vs. 85:dox+.WOtreh-	2.419	0.0319
70:dox-.WOtreh- vs. 85:dox+.WOtreh+	2.217	0.0469
70:dox-.WOtreh+ vs. 75:dox-.WOtreh-	2.293	0.0367
70:dox-.WOtreh+ vs. 75:dox-.WOtreh+	8.715	<0.0001
70:dox-.WOtreh+ vs. 75:dox+.WOtreh-	2.761	0.0134
70:dox-.WOtreh+ vs. 80:dox-.WOtreh-	3.649	0.002
70:dox-.WOtreh+ vs. 80:dox-.WOtreh+	6.908	0.0001
70:dox-.WOtreh+ vs. 80:dox+.WOtreh-	4.372	0.0004
70:dox-.WOtreh+ vs. 80:dox+.WOtreh+	5.596	<0.0001
70:dox-.WOtreh+ vs. 85:dox-.WOtreh-	4.173	0.0007
70:dox-.WOtreh+ vs. 85:dox-.WOtreh+	10.76	<0.0001
70:dox-.WOtreh+ vs. 85:dox+.WOtreh-	6.056	<0.0001
70:dox-.WOtreh+ vs. 85:dox+.WOtreh+	5.866	<0.0001
70:dox+.WOtreh- vs. 80:dox-.WOtreh+	2.806	0.0138
70:dox+.WOtreh- vs. 80:dox+.WOtreh-	2.834	0.0196
70:dox+.WOtreh- vs. 80:dox+.WOtreh+	3.22	0.0069
70:dox+.WOtreh- vs. 85:dox-.WOtreh-	2.569	0.0193
70:dox+.WOtreh- vs. 85:dox-.WOtreh+	4.333	0.0011
70:dox+.WOtreh- vs. 85:dox+.WOtreh-	3.491	0.0068
70:dox+.WOtreh- vs. 85:dox+.WOtreh+	3.411	0.005
70:dox+.WOtreh+ vs. 75:dox-.WOtreh+	2.245	0.0454
70:dox+.WOtreh+ vs. 75:dox+.WOtreh+	3.054	0.0157
70:dox+.WOtreh+ vs. 80:dox-.WOtreh-	2.385	0.0335
70:dox+.WOtreh+ vs. 80:dox-.WOtreh+	2.81	0.0187
70:dox+.WOtreh+ vs. 80:dox+.WOtreh-	2.67	0.0216
70:dox+.WOtreh+ vs. 80:dox+.WOtreh+	3.795	0.0053
70:dox+.WOtreh+ vs. 85:dox-.WOtreh-	2.745	0.0169
70:dox+.WOtreh+ vs. 85:dox-.WOtreh+	3.694	0.0052
70:dox+.WOtreh+ vs. 85:dox+.WOtreh-	3.283	0.0092
70:dox+.WOtreh+ vs. 85:dox+.WOtreh+	4.1	0.0034
75:dox-.WOtreh- vs. 85:dox-.WOtreh-	2.7	0.0244
75:dox-.WOtreh+ vs. 85:dox-.WOtreh+	4.131	0.0033
75:dox+.WOtreh- vs. 80:dox+.WOtreh-	3.787	0.0043

75:dox+.WOtreh- vs. 85:dox-.WOtreh+	2.855	0.0149
75:dox+.WOtreh- vs. 85:dox+.WOtreh-	3.335	0.0087
75:dox+.WOtreh+ vs. 80:dox+.WOtreh+	3.303	0.0108
75:dox+.WOtreh+ vs. 85:dox-.WOtreh+	3.229	0.0093
75:dox+.WOtreh+ vs. 85:dox+.WOtreh-	2.596	0.0251
75:dox+.WOtreh+ vs. 85:dox+.WOtreh+	3.252	0.0117
80:dox-.WOtreh- vs. 85:dox-.WOtreh-	2.853	0.019
80:dox-.WOtreh+ vs. 85:dox-.WOtreh+	2.822	0.0224

Table S17.: ANOVA results related to Fig.3.26.

ANOVA results for Figure 3.26.B.	**F (DFn, DFd)**	**P value**
rpm x treatment	F (6, 66) = 0.5081	P=0.8001
rpm	F (2.616, 57.55) = 1.272	P=0.2919
treatment	F (2, 22) = 1.138	P=0.3385
Subject	F (22, 66) = 0.8502	P=0.6549
ANOVA results for Figure 3.26.C.	**F (DFn, DFd)**	**P value**
rpm x treatment	F (8, 88) = 0.3417	P=0.9473
rpm	F (2.764, 60.81) = 4.744	P=0.0060
treatment	F (2, 22) = 1.129	P=0.3413
Subject	F (22, 88) = 1.311	P=0.1875

Table S18.: ANOVA results related to Fig.3.27.

ANOVA results for Figure 3.27.C.	**F (DFn, DFd)**	**P value**
time-bin x trreatment	F (6, 66) = 1.648	P=0.1481
time-bin	F (2.269, 49.91) = 2.239	P=0.1108
treatment	F (2, 22) = 1.445	P=0.2572
Subject	F (22, 66) = 3.005	P=0.0003
ANOVA results Figure 3.27.D.	**F (DFn, DFd)**	**P value**
time-bin x trreatment	F (6, 66) = 1.461	P=0.2052
time-bin	F (2.042, 44.93) = 32.61	P<0.0001
treatment	F (2, 22) = 1.204	P=0.3189
Subject	F (22, 66) = 7.177	P<0.0001

Table S19.: ANOVA results related to Fig.3.30.

ANOVA results for Figure 3.30.A.	**F (DFn, DFd)**	**P value**
trial x aso	F (3, 33) = 0.9414	P=0.4318
trial	F (1.855, 20.41) = 2.837	P=0.0851
aso	F (1, 11) = 1.117	P=0.3131
Subject	F (11, 33) = 1.625	P=0.1371
ANOVA results for Figure 3.30.B.	**F (DFn, DFd)**	**P value**
rpm x aso	F (4, 44) = 1.569	P=0.1995
rpm	F (2.804, 30.84) = 8.592	P=0.0003
aso	F (1, 11) = 5.994	P=0.0323
Subject	F (11, 44) = 3.873	P=0.0006

Table S20.: ANOVA results related to Fig.3.33.

ANOVA results for Figure 3.33.C.	**F (DFn, DFd)**	**P value**
time-bin x aso	F (3, 36) = 1.839	P=0.1576

time-bin	F (1.555, 18.66) = 7.302	P=0.0072
aso	F (1, 12) = 0.2341	P=0.6372
Subject	F (12, 36) = 6.105	P<0.0001
ANOVA results for Figure 3.33.D.	**F (DFn, DFd)**	**P value**
time-bin x aso	F (3, 36) = 0.1378	P=0.9368
time-bin	F (2.466, 29.60) = 19.65	P<0.0001
aso	F (1, 12) = 1.853	P=0.1985
Subject	F (12, 36) = 15.83	P<0.0001

Declaration of Honor

I hereby declare that I prepared this thesis without impermissible help of third parties and that none other than the indicated tools have been used; all sources of information are clearly marked, including my own publications.

In particular I have not consciously:

- Fabricated data or rejected undesired results
- Misused statistical methods with the aim of drawing other conclusions than those warranted by the available data
- Plagiarized external data or publications
- Presented the results of other researchers in a distorted way

I am aware that violations of copyright may lead to injunction and damage claims of the author and also to prosecution by the law enforcement authorities.

I hereby agree that the thesis may be reviewed for plagiarism by mean of electronic data processing.

This work has not yet been submitted as a doctoral thesis in the same or a similar form in Germany or in any other country. It has not yet been published as a whole.

Magdeburg, 20.04.2020

Ufuk Emre Kul